

Dish surface characterization for HIRAX and CHORD using metrology and simulations

Aditya Krishna Karigiri Madhusudhan



Department of Physics, Trottier Space Institute
McGill University
Montréal, Québec, Canada

September 2024

A thesis submitted to McGill University in partial fulfillment of the requirements of the degree of

Master of Science in Physics

©Aditya Krishna K M 2024

Abstract

Understanding the expansion history of the universe is crucial to modern cosmology, as it offers insights into the nature of dark energy and dark matter, as well as the formation and evolution of large-scale structures. The Hydrogen Intensity and Real-time Analysis eXperiment (HIRAX) and the Canadian Hydrogen Observatory and Radio-transient Detector (CHORD) are next-generation radio interferometers designed to measure baryonic acoustic oscillations (BAOs) through 21 cm intensity mapping (IM) and also act as a powerful platform for studying fast radio bursts (FRBs), pulsars and cross-correlation studies. Achieving precision cosmology with 21 cm IM techniques necessitates that HIRAX and CHORD interferometers meet stringent design, alignment, and calibration requirements. Thus, to develop redundant front-end electronic systems, feeds, and precise metrology methods, the Deep-Dish Development Array (D3A) was deployed at the Dominion Radio Astrophysical Observatory (DRAO). This small interferometric prototype array, comprising 2 three-meter and 3 six-meter composite dishes, serves as a testbed for various technologies, including antenna feed and mount design, reflector fabrication

methods, the signal conditioning chain, and the readout system for HIRAX and CHORD. This thesis focuses on the dish surface characterization for CHORD and HIRAX, emphasizing the necessity of redundancy to achieve the desired scientific objectives. It discusses the mathematical framework required to analyze data from precise metrology techniques, such as laser tracker, photogrammetry, and finite element analysis. The implementation and results from these analyses are presented, highlighting the critical steps taken to ensure the accuracy and precision of the dish surface. Furthermore, the effects of these surface deformations on the telescope's beam pattern are investigated through electromagnetic (EM) simulations in CST Studio Suite, which helps determine the dish tolerances and optimal parameters needed to achieve redundancy targets. Finally, the concept of beam covariance is introduced as a metric to quantify the spatial variations within the beam patterns due to these surface deformations.

Résumé

Comprendre l'histoire de l'expansion de l'univers est crucial pour la cosmologie moderne, car elle offre un aperçu de la nature de l'énergie noire et de la matière noire, ainsi que de la formation et de l'évolution de structures à grande échelle. L'expérience d'analyse de l'intensité de l'hydrogène et d'analyse en temps réel (HIRAX) et l'observatoire canadien de l'hydrogène et le détecteur de transit radio (CHORD) sont des interféromètres radio de nouvelle génération conçus pour mesurer les oscillations acoustiques baryoniques (BAO) grâce à une cartographie d'intensité de 21 cm et agissent également comme une plate-forme puissante pour étudier les sursauts radio rapides (FRB), les pulsars et les études de corrélation croisée. Pour obtenir une cosmologie de précision avec des techniques de cartographie d'intensité de 21 cm, les interféromètres HIRAX et CHORD doivent répondre à des exigences strictes en matière de conception, d'alignement et d'étalonnage. Ainsi, pour développer des systèmes électroniques frontaux redondants, des alimentations et des méthodes de métrologie précises, le Deep-Dish Development Array (D3A) a été déployé à l'Observatoire fédéral de radioastrophysique (DRAO). Ce petit réseau prototype

interférométrique, comprenant 2 paraboles composites de trois mètres et 3 paraboles composites de six mètres, sert de banc d'essai pour diverses technologies, notamment la parabole composite, la conception des montures, les alimentations d'antenne, la chaîne de conditionnement du signal et le système de lecture pour HIRAX et CHORD. Cette thèse se concentre sur la caractérisation de la surface des paraboles pour CHORD et HIRAX, en soulignant la nécessité de redondance pour atteindre les objectifs scientifiques souhaités. Il aborde le cadre mathématique requis pour analyser les données issues de techniques de métrologie précises, telles que le laser tracker, la photogrammétrie et l'analyse par éléments finis. La mise en œuvre et les résultats de ces analyses sont présentés, mettant en évidence les étapes critiques prises pour garantir l'exactitude et la précision de la surface de la parabole. De plus, les effets de ces déformations de surface sur le modèle de faisceau du télescope sont étudiés au moyen de simulations électromagnétiques dans CST Studio Suite, qui permettent de déterminer les tolérances de la parabole et les paramètres optimaux nécessaires pour atteindre les objectifs de redondance. Enfin, le concept de covariance des faisceaux est introduit comme mesure pour quantifier les variations spatiales dans les modèles de faisceaux dues à ces déformations de surface.

Acknowledgements

It gives me immense pleasure to write this thesis, marking the culmination of my master's program. This journey has been an enriching experience, and it would not have been possible without the support and guidance of many individuals. First and foremost, I would like to express my deepest gratitude to my supervisor, *H Cynthia Chiang* for her invaluable guidance, encouragement, and patience. I am immensely grateful for her confidence in my ability to pursue cosmology despite my engineering background, which has been a significant source of motivation. I would also like to thank my supervisory committee member, *Jonathan Sievers*, whose expertise and guidance in computational physics have been instrumental in the successful execution of my research. The foundation of this work rests significantly on various measurements and simulation data generously provided by *Mohammad Nouroz Islam* from the National Research Council (NRC) Canada. His unwavering support and feedback have enhanced the reliability of the findings presented herein. Special thanks to *Kit M. Gerodias* for introducing me to CST simulation software and guiding me in the realm of EM simulations. The insightful discussions we had on interpreting the intricacies of simulation

results and his valuable contributions throughout this journey are greatly appreciated. I had the pleasure of working with the *McGill Radio Lab* research group where I witnessed the dedication and expertise of every member in advancing our knowledge of the cosmos. Being a part of this family has been an honor, and I am thrilled to continue with these outstanding individuals for my next academic endeavor. I would like to express my sincere gratitude to Benjamin Saliwanchik, Devin Crichton, and Dallas Wulf for their timely feedback during the telecons and constant support throughout this journey. Additionally, I am thankful to the CHORD/HIRAX collaboration members for welcoming me into their vision and giving me the opportunity to contribute to their pioneering work.

Words cannot express my gratitude towards my mother, *Hiranmaye*, my elder sisters, *Nivedha* and *Keerthi*, and my brother-in-law, *Narasimhon*. Their love, understanding, and faith in my abilities have been the pillars that sustained me throughout this journey. I love you guys, and can't wait to see you all here as I walk the stage for my graduation! I am blessed with friends whose unwavering support and encouragement have provided me with the resilience needed to navigate challenges. My dear people, *Srinivasan*, *Vinay*, *Porkodi*, *Soundarya*, *Sandhya*, *Ajay* and *Vimal*, thanks for making my life more fun and happy! Finally, I conclude by expressing my gratitude to Mother Nature for providing me with this beautiful life to cherish and the opportunity to contribute to sustainability.

Contents

List of Figures	XIII
List of Tables	XIV
1 Cosmic Odyssey: Probing the Universe with Radio Astronomy	1
1.1 Standard Model of Modern Cosmology	4
1.2 Expansion History of the Universe	6
1.3 Baryonic Acoustic Oscillations	9
1.3.1 The Cosmic Dance between Gravity and Pressure	10
1.3.2 BAO as a Standard Ruler	11
1.4 Tracing Back using 21 cm Intensity Mapping	14
1.5 Elements of Radio Astronomy	19
1.5.1 Dish and Feed Antenna	20
1.5.2 Analog and Digital Electronics	23
1.6 Thesis Outline	24

2	Principles of Radio Interferometry	26
2.1	A Two-Element Radio Interferometer	26
2.1.1	Noise and System Temperature	32
2.1.2	The Importance of Redundancy	35
2.2	Overview of HIRAX and CHORD	36
2.3	Deep-Dish Development Array (D3A)	43
2.3.1	Composite Dishes	44
2.3.2	Radio Frequency over Fibre System	46
2.3.3	ICE-system vs RFSoc based F Engine	48
3	Metrology on D3A6 Composite Dishes	50
3.1	Laser Tracker Analysis	51
3.1.1	Nomenclature and Methodology	54
3.1.2	Evaluation Metrics	61
3.1.3	Results and Discussions	65
3.2	Photogrammetry Analysis	71
3.2.1	Methodology	73
3.2.2	Results and Discussion	75
3.3	Effects of Radome on CHORD dishes	78
3.3.1	Methodology and Results	81

4	Surface Deformation Effects on Beam Patterns through EM Simulations	87
4.1	Propagating Surface Deformations to CST	94
4.2	Simulations of Deformed Dishes with HIRAX Feed	99
4.2.1	Surface Deformations from Laser Tracker Analysis	100
4.2.2	Surface Deformations from Photogrammetry Analysis	105
4.3	A Glimpse of CST Simulations with CHORD Feed	112
5	Beam Covariance	116
5.1	A Metric to Quantify the Beam Differences	116
5.2	Mathematical Framework of Beam Covariance	118
5.3	Results and Discussions	124
6	Summary and Future Work	132

List of Figures

1.1	The energy density evolution of the main components of the universe as a function of scale factor $a(t)$	8
1.2	BAO as a standard ruler	12
1.3	BAO detection using SDSS data	13
1.4	Hyperfine splitting of hydrogen atom	15
1.5	Anatomy of a traditional radio telescope	21
2.1	Block diagram of a two-element radio interferometer	29
2.2	Canadian Hydrogen Observatory and Radio-transient Detector (CHORD)	39
2.3	Hydrogen Intensity Real-time Analysis eXperiment (HIRAX)	40
2.4	DRAO site and the D3A dishes	47
3.1	Laser tracker datasets of mold and D3A6 dishes.	53
3.2	Rotational and translational corrections for laser tracker datasets.	55

3.3	Regular gridding of dish 2 laser tracker dataset on a $f/0.21$ 6-m parabolic grid and a uniform rectangular grid.	59
3.4	Residual plots of the difference between the laser tracker data D'_i and averaged BFP \bar{P}	62
3.5	Illustration of vertical vs perpendicular residuals in a 1D linear fitting model.	63
3.6	Residual plots of the difference between the laser tracker data D''_i and averaged azimuthally clocked datasets \bar{D}	68
3.7	Residual plots of difference between laser tracker datasets, $D''_i - D''_j$	70
3.8	Photogrammetry datasets of D3A6 dishes 1 and 2 at 0° and 30° zenith angles.	72
3.9	Residual plots of photogrammetry datasets, $D'_i - P_i$	76
3.10	Difference between Photogrammetry dishes 1 and 2 at 0 and 30 degrees zenith angle.	79
3.11	Difference between laser tracker and photogrammetry dishes 1 and 2 at 0° zenith angle.	80
3.12	FEA surface RMS errors and feed displacement magnitude for 0, 40 and 80 kph wind speeds at 0° , $+30^\circ$ and -30° zenith angles.	82
3.13	FEA residual plots for 0 kph wind speed at 0° , $+30^\circ$ and -30° zenith angles, with and without the radome.	84
3.14	FEA residual plots for 40 kph wind speed at 0° , $+30^\circ$ and -30° zenith angles, with and without the radome.	85

3.15	FEA residual plots for 80 kph wind speed at 0° , $+30^\circ$ and -30° zenith angles, with and without the radome	86
4.1	CST CAD model of the dish and HIRAX/CHORD feed components.	88
4.2	2D electric field distribution and 1D beam pattern plots at $\phi = 0^\circ$ and 90° for the dish and HIRAX feed model.	91
4.3	2D electric field distribution and 1D beam pattern plots at $\phi = 0^\circ$ and 90° for the dish with CHORD feed model.	93
4.4	A $f/0.21$ 6-m parabolic grid with 5000 and 20000 facets along with the faceted surfaces rendered using SolidWorks and python	95
4.5	2D beam difference between the HIRAX fiducial and discretized beams rendered with 5000 facets using SolidWorks and Python.	98
4.6	Beam difference between fiducial and deformed surface models using laser tracker dish 1 residuals.	101
4.7	Beam differences among laser tracker dishes 1, 2, and 3 using 5000-faceted deformed surface models.	103
4.8	Primary beams of fiducial and deformed surface models using laser tracker dishes 1, 2, and 3 residuals.	104
4.9	Beam difference between fiducial and deformed surface models using Photogrammetry dish 1 residuals at 0° zenith angle.	106

4.10	Beam difference between fiducial and deformed surface models using Photogrammetry dish 1 residuals at 30° zenith angle.	108
4.11	Beam differences between 0° and +30° zenith angles for photogrammetry dishes 1 and 2 with 5000 and 20000-faceted models	110
4.12	Primary beams of fiducial and deformed surface models using Photogrammetry dishes 1 and 2 residuals at 0° and +30° zenith angles. . . .	111
4.13	Beam difference between fiducial and discretized surface models with the CHORD feed	114
4.14	Primary beams (1D beam cuts at $\phi = 0^\circ$ and $\phi = 90^\circ$) of fiducial and discretized surface models with the CHORD feed	115
5.1	A glimpse of the coordinate system (θ, ϕ) surrounding the dish in CST	117
5.2	Beam differences, $R_{\text{cond}}^{-1/2}$, for the perturbed CST models with feed offsets and dish surface discretizations.	125
5.3	Beam differences, $R_{\text{cond}}^{-1/2}$, for the perturbed CST models with feed tilts/rotations in x , y , and z axes.	128
5.4	Beam differences, $R_{\text{cond}}^{-1/2}$, for the perturbed CST models with feed tilts/rotations staying within TMA limits, in x , y , and z axes.	130

List of Tables

2.1	Instrumental parameters of HIRAX and CHORD	41
3.1	List of laser tracker variables and their definitions.	56
3.2	Vertical and perpendicular RMSE of laser tracker dataset, σ_i along with the errors obtained from comparison against \bar{P} and \bar{D}	66
3.3	Vertical and perpendicular RMS errors of photogrammetry dataset, σ_i	77
4.1	Primary beams parameters of HIRAX and CHORD fiducial models.	92
4.2	RMS errors of beam differences between fiducial and deformed surface models, incorporating surface errors from laser tracker and photogrammetry analyses.	109
5.1	Beam difference, $R_{\text{cond}}^{-1/2}$, for the deformed surface models.	127

Chapter 1

Cosmic Odyssey: Probing the Universe with Radio Astronomy

IN the core of our collective human endeavor resides an innate curiosity to explore the world around us and to understand our origins. It was this universal quest that led to a new branch of physics, *Cosmology*, concerned with the study of the chronology of the universe. The most complete description of the geometrical properties of the universe is provided by Einstein's general theory of relativity (GR) which describes gravity as the curvature of spacetime caused by the presence of mass and energy. In this framework, the Friedmann-Lemaître-Robertson-Walker (FLRW) metric serves as the foundation, providing a mathematical model for the universe's expansion and evolution over time. Assuming a homogeneous and isotropic space, the FLRW metric is conventionally written in the form

$$ds^2 = -c^2 dt^2 + a(t)^2 [dr^2 + \delta_k(r)^2 d\Omega^2], \quad (1.1)$$

where $a(t)$ is a dimensionless function called the *scale factor* which describes how distances grow or decrease with time, c is the speed of light, $d\Omega^2 = d\theta^2 + \sin^2 \theta d\phi^2$ and $\delta_k(r)$ defines the curvature of the universe and can take one of the following three forms depending on the curvature constant, k .

$$\delta_k(r) = \begin{cases} R_0 \sin(r/R_0), & k = 1 \quad (\text{Positively curved universe}) \\ r, & k = 0 \quad (\text{Flat universe}) \\ R_0 \sinh(r/R_0), & k = -1 \quad (\text{Negatively curved universe}) \end{cases} \quad (1.2)$$

Here, r represents the co-moving radial coordinate, and R_0 which has dimensions of length, is the radius of curvature at the present moment for a curved space. The current best model of the universe which matches all physical observations extremely closely is the *Big Bang theory* that describes how the universe expanded from an initial state of high density and temperature. The earliest and most direct observational evidence of the Big Bang theory is the expansion of the universe according to Hubble's law, the discovery and measurement of the cosmic microwave background (CMB), and the relative abundances of light elements produced by Big Bang nucleosynthesis (BBN). Edwin Hubble in 1929 observed the relation between distance and radial velocity among extra-galactic nebulae and showed that the

galaxies are receding away from us with a velocity that is proportional to their distance from us, i.e., more distant galaxies recede faster than nearby galaxies (Hubble, 1929). This linear relation between galaxy velocity (v) and its distance (d) is given as

$$v = H_0 \times d, \tag{1.3}$$

where H_0 is the current expansion rate of the universe called as *Hubble's constant* and estimated to be 70 km/s/Mpc.

However, in 1998, the evidence from studying distant Type Ia supernovae showed that the expansion of the universe was accelerating rather than slowing down due to gravity (Schmidt et al., 1998; Garnavich et al., 1998). To explain this acceleration, GR requires that much of the energy in the universe consists of a component with large negative pressure, dubbed *dark energy* (DE). In the late 1980s, various observations indicated that the amount of visible matter in the universe was insufficient to account for the observed gravitational forces within and between galaxies. This led to the idea that up to 90% of the matter in the universe is *dark matter* (Rubin and Ford Jr, 1970; Rubin et al., 1985) that does not emit light or interact with normal baryonic matter. Thus, to reconcile these observations, a comprehensive framework was required that can simultaneously explain the accelerated expansion, large-scale structure formation, and the abundance of dark matter and dark energy in the universe. The following sections on the cosmological background are referred from the works of Ryden (2017), Dodelson and Schmidt (2020), and Huterer (2023).

1.1 Standard Model of Modern Cosmology

The standard cosmological model, also known as the Λ CDM model assumes that the universe has a component of its energy density driven by the cosmological constant, Λ (believed to be due to dark energy), and that dark matter is cold dark matter (i.e. dark matter particles that have non-relativistic velocities). Applying the FLRW metric to Einstein's field equations leads to the Friedmann equations¹

$$H(t)^2 = \left(\frac{\dot{a}}{a}\right)^2 = \frac{8\pi G}{3}\rho(t) - \frac{k}{R_0^2 a(t)^2} + \frac{\Lambda}{3}, \quad (1.4)$$

$$\frac{\ddot{a}}{a} = \frac{-4\pi G}{3}(\rho + 3P) + \frac{\Lambda}{3}, \quad (1.5)$$

which provides a comprehensive description of how the expansion rate of the universe depends on its energy content, curvature, and the presence of dark energy. Here, $H(t)$ is the Hubble parameter defined as the function of time, ρ and P are the mean energy density and the mean pressure of the universe's contents. In reality, the evolution of our universe is complicated by the fact that it contains different components with different equations of state (EoS) that relate the energy density of the contents to its pressure as

$$P = \omega\rho, \quad (1.6)$$

¹Note that throughout the section 1.1, natural units are used such that $c = 1$

where ω is a dimensionless number called the EoS parameter. For matter, radiation, and the cosmological constant, ω equals 0, 1/3, and -1 respectively. To see how the universe expands when there are multiple components, we need to know how the mean energy density of the universe varies with time. From the Friedmann equations described above, one arrives at

$$\dot{\rho} = -3H(t)(\rho + \omega), \quad (1.7)$$

which can be solved analytically assuming all components of the universe are perfect fluid that obeys the equation of state. Thus, for each component, Equation 1.7 becomes

$$\rho(a) = \rho_0 a^{-3(1+\omega)}, \quad (1.8)$$

where ρ_0 denotes the present-day energy density of the components. For a given rate of expansion, there is a critical density, ρ_c which is that combination of matter and energy that brings the universe coasting to a stop at time infinity (Dolgov, 1991). If the actual density is higher than this critical density, then the expansion will reverse and the universe will begin to contract. If the actual density is lower, then the universe will expand forever. For a multi-component universe containing contributions from matter, radiation, cosmological constant, and curvature, the Friedmann equation is expected to take the form:

$$H(t)^2 = H_0^2 \left(\Omega_{m,0} a^{-3} + \Omega_{r,0} a^{-4} + \Omega_{\Lambda,0} a^{-3(1+\omega)} + \Omega_{k,0} a^{-2} \right), \quad (1.9)$$

where $\Omega_{m,0}$, $\Omega_{r,0}$, $\Omega_{\Lambda,0}$ and $\Omega_{k,0}$ are the present-day density parameter (ratio of the actual density ρ to the critical density ρ_c) for matter, radiation, cosmological constant and curvature respectively. Considering a universe that is spatially flat, and contains both matter and a cosmological constant is of particular interest to us, since it appears to be in a close approximation to our universe at the present day. With this framework in place, we are now poised to journey back through time and understand the expansion history of our universe.

1.2 Expansion History of the Universe

From 10^{-36} seconds to between 10^{-33} and 10^{-32} seconds after the Big Bang, the universe expanded faster than the speed of light, a period called *cosmic inflation* which is believed to be due to a hypothetical scalar field called an inflaton that has a large energy density and negative pressure, causing the universe to expand exponentially (Guth, 1981). After Inflation, and until about 47,000 years after the Big Bang, the dynamics of the early universe were dominated by radiation, referring to the universe's constituents that moved relativistically, principally photons and neutrinos. We call this the *radiation-dominated era* and the Friedmann equation takes the form (Debono and Smoot, 2016)

$$\frac{\dot{a}}{a} = \left(\frac{8\pi G \rho_r(t)}{3} \right)^{1/2} = \left(\frac{8\pi G \rho_r(t_0)}{3} \right)^{1/2} a(t)^{-2}. \quad (1.10)$$

Solving the above equation for $a(t)$ gives

$$a(t) = (2H_0t)^{1/2} \quad , \quad H(t) = \frac{1}{2t_0}. \quad (1.11)$$

Thus during this era, the cosmic expansion decelerated, with the scale factor growing proportionally with the square root of the time. The universe was still too hot for the atomic nuclei of primordial elements to catch electrons and form complete atoms and thus remained optically thick to radiation as a vast number of electrons created a sort of fog that scattered light. Since radiation redshifts as the universe expands, eventually, the non-relativistic matter came to dominate the energy density of the universe, marking the transition into the *matter-dominated era*. The Friedmann equation for this era can be written as

$$\frac{\dot{a}}{a} = \left(\frac{8\pi G\rho_m(t)}{3} \right)^{1/2} = \left(\frac{8\pi G\rho_m(t_0)}{3} \right)^{1/2} a(t)^{-3/2} = H_0 a(t)^{-3/2}. \quad (1.12)$$

Solving the above equation for $a(t)$, we find that the cosmic expansion decelerated, with the scale factor growing as the 2/3 power of time ([Debono and Smoot, 2016](#)):

$$a(t) = \left(\frac{3H_0t}{2} \right)^{2/3} \quad , \quad H(t) = \frac{2}{3t_0}. \quad (1.13)$$

The cosmological constant, Λ , can be viewed as equivalent to the ‘mass’ of empty space. Since this increases with the volume of the universe, the expansion pressure is effectively

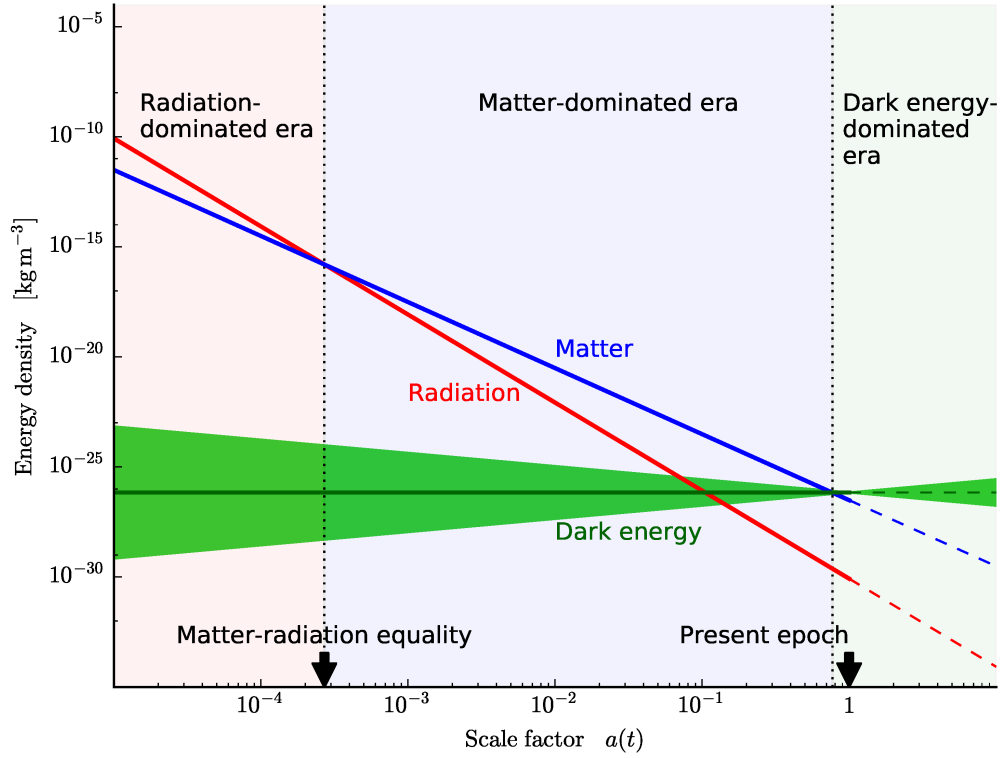


Figure 1.1: The density evolution of the universe’s primary components (from [Debono and Smoot \(2016\)](#)) shows a transition from a radiation-dominated early universe to a matter-dominated epoch as the temperature decreased. As the universe expanded and the matter-energy density decreased, dark energy began to dominate in the recent past. The green band represents dark energy, with an EoS parameter $\omega = -1 \pm 0.2$.

constant, independent of the scale of the universe. As the density of matter and radiation dropped to very low concentrations over time as shown in [Figure 1.1](#), the cosmological constant term eventually dominated the energy density of the universe, entering the *dark energy domination era*. Solving Friedmann equations for $a(t)$ gives

$$a(t) = e^{H_0(t-t_0)}. \quad (1.14)$$

Unlike the previous two scenarios, the solution of $a(t)$ here is not compatible with the initial condition $a(0) = 0$. Instead, it gives $a(0) = e^{-H_0 t_0}$ which is nonzero unless $H_0 t_0 \rightarrow +\infty$. The way out is to define the beginning time of universe $t = -\infty$ so that $a(t) = 0$. Thus a flat universe dominated by cosmological constant is infinitely old and exponentially expands. Using the relation between redshift, z and scale factor, $a(t)$ as given by

$$1 + z = \frac{\lambda(t_0)}{\lambda(t_e)} = \frac{1}{a(t_e)}, \quad (1.15)$$

where t_0 and t_e denote the observed and emitted time respectively, the onset of dark energy dominated era from Equation 1.9 corresponds to the interval of redshift between $1 < z < 2$ (de Araujo, 2005). To comprehend the characteristics of dark energy, more observational data is necessary, especially in the redshift range corresponding to dark energy domination as given above. Fortunately, nature has provided us with a unique cosmic ruler that can be used to understand the universe's expansion history.

1.3 Baryonic Acoustic Oscillations

Baryonic acoustic oscillations (BAOs) are a pattern of wrinkles in the density distribution of the clusters of galaxies spread across the universe (Bassett and Hlozek, 2010). They are a subtle but important effect because they provide an independent way to measure the expansion rate of the universe and how that rate has changed throughout cosmic history.

1.3.1 The Cosmic Dance between Gravity and Pressure

Back when the universe was in its infancy, matter was spread out in an almost uniform sea of charged particles. Tiny fluctuations in the density of about one part in 100,000 took the form of slight matter overdensities that attracted additional material due to gravity. This was not an easy process because the matter heated up as gravity pulled it together. This created an outward radiation pressure from photons that pushed the matter apart again. As it expanded, however, it cooled and gravity started to pull it back together again. This interplay of gravity and pressure set up an oscillation that generated acoustic waves within the photon-baryon fluid, thus influencing the distribution of matter and photons, and creating anisotropies in their densities.

Around 380,000 years after the Big Bang, the universe had cooled enough that atomic nuclei could capture electrons, a period called *recombination* ($z \approx 1100$). The formation of these first atoms released the photons that had previously been tightly coupled to electrons and are detectable today as the cosmic microwave background (CMB). With little now to resist gravity, the ripples essentially froze in place, with a characteristic length scale set by the sound horizon at approximately 0.14 megaparsecs (Mpc) (Aubourg et al., 2015). These ripples carried with them slightly more matter than the average density across the universe. Over several hundred years, these matter inhomogeneities caused further accumulation in denser regions, eventually leading to the formation of stars and galaxies. Consequently, slightly more galaxies formed along the ripples than elsewhere. As the

universe expanded, these frozen ripples stretched, now spanning approximately 147.41 ± 0.30 Mpc, thereby increasing the distances between galaxies by the same amount. Thus, by studying the distribution of galaxies across different cosmic epochs, we can investigate the evolving expansion of the universe over time.

1.3.2 BAO as a Standard Ruler

The concept of a standard ruler is straightforward: we determine the distance to an object of known size by measuring the angular size it subtends in our field of view. The BAO scale can be measured along and across the line of sight as shown in Figure 1.2. The BAO peak at a redshift z appears at an angular separation

$$\theta = \frac{r_d}{(1+z)d_A(z)} \quad (1.16)$$

where $d_A(z)$ is the angular diameter distance and r_d is the sound horizon at the drag epoch—the time when baryons were released from the drag of photons (Santos et al., 2011). The angular diameter distance and the Hubble parameter can then be mapped by measuring the transverse separation size L_\perp and the redshift interval Δz along the line of sight, respectively as

$$d_A(z) = \frac{L_\perp(z)}{(1+z)} \propto \int_0^z \frac{dz'}{H(z')} \quad , \quad H(z) = \frac{c\Delta z}{L_\parallel(z)}, \quad (1.17)$$

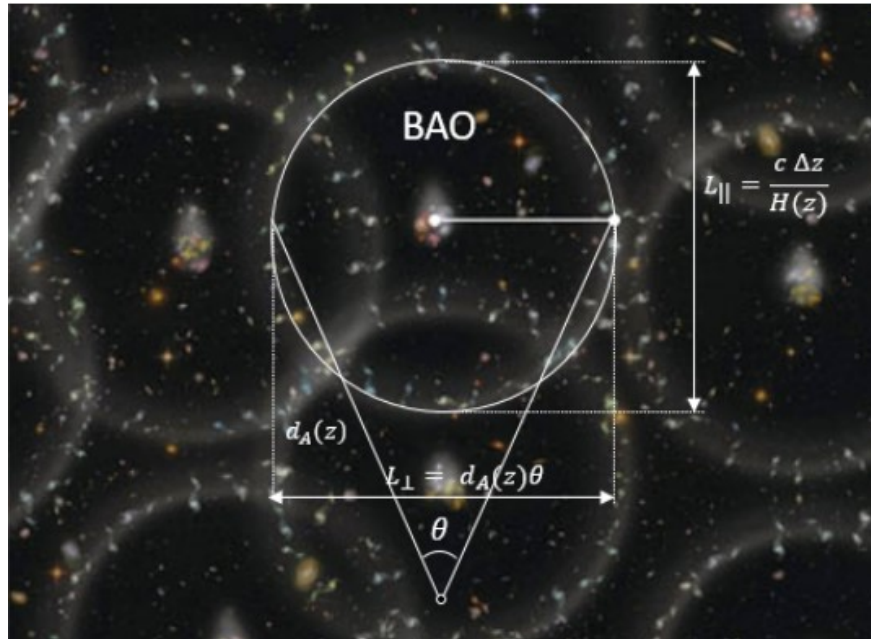


Figure 1.2: This artist’s illustration of the BAO structure^a shows the radial and angular sizes of the acoustic oscillations, with L_{\parallel} measuring the separation along the line of sight and L_{\perp} measuring the separation perpendicular to the line of sight.

^aCredit: Zosia Rostomian, Lawrence Berkeley National Laboratory. The distribution and clustering of galaxies along the BAO structures are greatly exaggerated and only serve to illustrate the separation size along and across the line of sight.

that helps constrain cosmological parameters and the nature of dark energy. To utilize BAO as a standard ruler for tracking the universe’s expansion history, it’s crucial to statistically measure the BAO structure by examining the power spectrum of the density field, depicting correlations in baryon density based on their separation, as shown in Figure 1.3. This necessitates mapping the baryon density and computing the associated power spectrum. Optical wavelengths through spectroscopic surveys have been instrumental in making these observations at lower redshift (Roukema, 2018). However, it is challenging to

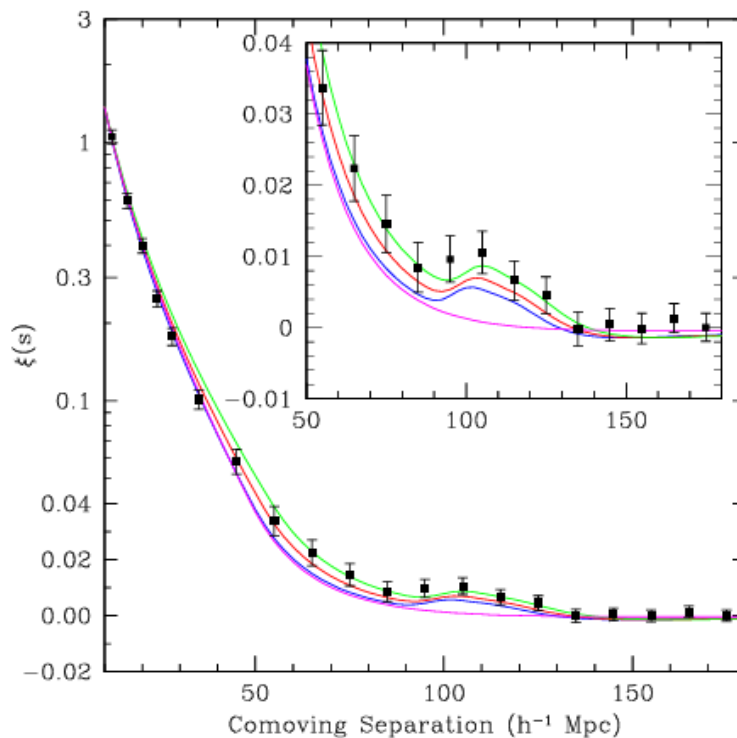


Figure 1.3: This plot from Eisenstein et al. (2005) shows the redshift-space correlation function measured from a spectroscopic sample of 46,748 luminous red galaxies from the Sloan Digital Sky Survey (SDSS). A well-detected peak has been observed in the correlation function at $100h^{-1}$ Mpc, which closely matches the expected shape and position of the imprint of acoustic oscillations during the recombination epoch. This detection confirms the linear growth of cosmic structure through gravitational instability from $z \approx 1000$ to the present day, confirming the predictions of the standard cosmological model.

make observations at higher redshifts for individual galaxies, and to detect them, large-volume surveys are needed. The following sections will describe how observing 21 cm emission from neutral hydrogen is a promising approach for mapping BAO structure over cosmological volumes that are difficult to access with optical surveys.

1.4 Tracing Back using 21 cm Intensity Mapping

The baryonic mass of the universe is largely hydrogen ($\sim 75\%$) with the remaining composed of helium. The electron and the proton in atomic hydrogen (HI) constitute tiny magnetic dipoles, whose interaction energy varies according to the relative orientation of their dipole moment, leading to the hyperfine structure in the energy levels as shown in Figure 1.4. If the spins are parallel, the energy is somewhat higher than it is when the spins are antiparallel. The difference is not too large, amounting to $\Delta E = 5.9 \times 10^{-6}$ eV, corresponding to a wavelength of 21.1 cm and a frequency of 1420 MHz (Pritchard and Loeb, 2012). However, it is only one line out of many that have been observed in local galaxies, which begs the question “Is 21 cm the most effective means to understand the large-scale structures?” To begin with, it tends to be optically thin, distinctly separated in frequency from other atomic lines, and hydrogen is ubiquitous in the universe. Moreover, this frequency is one of the most precisely known quantities, having been measured with great accuracy from studies of hydrogen masers (Pritchard and Loeb, 2012). Through the use of 21 cm intensity mapping (IM)—a technique that maps the universe by measuring the collective 21 cm emission from underlying matter—we harness a powerful tool for constraining dark energy via measurements of BAOs in the galaxy power spectrum. Redshifts around $z \sim 2$ are of great interest because this marks the transition period when dark energy began to dominate the energy budget of the universe. Therefore, probing a redshift range that brackets this transition is crucial for understanding the influence of dark energy on cosmic expansion. While galaxy surveys will begin to probe

is labeled with a subscript 0 and 1 for the 1S singlet and 1S triplet levels, respectively) and is given as (Nusser, 2005)

$$\frac{n_1}{n_0} = \frac{g_1}{g_0} e^{-(T_*/T_s)} \quad (1.18)$$

The anti-parallel lower energy state (E_0) has total spin $S = 0$, so its degeneracy is $g_0 = 2S + 1 = 1$. The upper state (E_1) has total spin $S = 1$, so $g_1 = 3$. The energy difference between the two states corresponds to a temperature $T_* = \Delta E_{10}/K_B = 0.0681$ K where K_B is the Boltzmann constant. The spin temperature is, therefore, merely a shorthand for the ratio between the occupation number of the two hyperfine levels (Griffiths, 1982). The spin temperature affects the contrast between the neutral hydrogen signal and the background radiation, which is essential for accurately detecting the 21 cm signal. Deviations from the CMB temperature, known as the brightness temperature fluctuations, provide information about the density and temperature distribution of neutral hydrogen gas in different regions of the universe (Kuhlen et al., 2006). The key challenge in using the 21-cm BAO signal to study dark energy is its faintness, with a mean brightness temperature of the order of about 0.1 mK (Tzu-Ching et al., 2008), requiring highly sensitive instruments and precise modeling to separate it from stronger galactic and extragalactic foregrounds and radio frequency interference (RFI).

Observations of the 21 cm line from the dark energy-dominated era are redshifted to radio frequencies which motivates the use of radio receivers with wide frequency bands to measure the signal as a function of redshift. The wide primary beam (which describes the

telescope’s sensitivity as a function of direction) of a radio telescope allows for the simultaneous integration of hydrogen emissions from a large number of galaxies, enabling the mapping of the three-dimensional distribution of neutral gas. However, a fundamental question emerges: “Which approach proves superior for IM measurements—utilizing a single, straightforward dish, or employing an interferometer array?” Various 21 cm IM projects employ both single-dish telescopes and interferometers, each offering distinct advantages. The first proof of concept demonstrating the 21-cm IM technique through cross-correlation between the Green Bank Telescope’s (GBT) radio spectra and the DEEP2 optical redshift survey (Davis et al., 2003) was conducted by Chang et al. (2010) where a detection of the 21-cm signal with a $\sim 4\sigma$ confidence level at redshifts between 0.53 and 1.12 was reported. Similarly, the study by Amiri et al. (2023) reported the detection of 21 cm emission from large-scale structures at redshifts between 0.78 and 1.43 using the Canadian Hydrogen Intensity Mapping Experiment (CHIME), which comprises four cylindrical telescopes operating between 400 and 800 MHz. The detection was made through cross-correlation with galaxies and quasars observed by the extended Baryon Oscillation Spectroscopic Survey (eBOSS) (Dawson et al., 2016). The first direct detection of the neutral hydrogen auto-power spectrum, without cross-correlating with galaxy surveys, was achieved by Paul et al. (2023) using the MEERKAT telescope. This detection reached a high level of statistical significance, with measurements of 8.0σ and 11.5σ at redshifts of 0.32 and 0.44, respectively. Other notable efforts include the Baryon Acoustic Oscillations

from Integrated Neutral Gas Observations (BINGO) ([Abdalla et al., 2022](#)), currently under construction in northeastern Brazil. BINGO uses a ~ 40 -meter dual-dish telescope and covers a redshift range from 0.127 to 0.449, offering a cost-effective approach to IM measurements at low redshifts. The Five hundred meter Aperture Spherical Telescope (FAST) ([Nan et al., 2011](#)) in southwestern China employs a 500-meter single-dish spherical telescope and observes the redshift range $0.5 < z < 2.5$, pioneering the effective implementation of a large single dish in 21 cm IM. The Hydrogen Intensity Real-time Analysis eXperiment (HIRAX) ([Crichton et al., 2022](#)) and the Canadian Hydrogen Observatory and Radio-transient Detector (CHORD) ([Vanderlinde et al., 2019](#))—the main focus of this thesis—are twin-radio interferometers planned for deployment in the southern and northern hemispheres, respectively. With their large collecting areas, wide-field outrigger stations, and high geometric redundancy, HIRAX and CHORD aim to enhance current measurements of Baryon Acoustic Oscillations (BAO) from galaxy surveys. These examples illustrate the diversity of approaches in 21-cm intensity mapping, showcasing how different telescope configurations cater to specific redshift ranges and scientific objectives in cosmological studies. Before diving into the principles of interferometry and focusing on HIRAX and CHORD—the primary subjects of this study—let us first understand the basic components and functionalities of a radio telescope.

1.5 Elements of Radio Astronomy

The radio frequency band spans a wide logarithmic range, covering five decades from 10 MHz to 1 THz at the lower end of the electromagnetic spectrum, which is delimited by the Earth's ionosphere, reflecting extraterrestrial radio waves with frequencies below ~ 10 MHz (Condon and Ransom, 2016). The Earth's atmosphere effectively blocks most electromagnetic radiation wavelengths, including infrared (IR), ultraviolet, X-ray, and gamma-ray, allowing only optical/near-IR and radio observations to be conducted from the ground. In radio astronomy, the strength of a radio source is commonly measured in terms of flux density, which is the amount of energy received per unit area per unit time per unit frequency. The standard unit for flux density is jansky (Jy), named after the pioneering radio astronomer Karl Jansky, and is defined as $10^{-26} \text{ Wm}^{-2}\text{Hz}^{-1}$. Just like optical telescopes, radio telescopes collect weak radio light waves, bring them to a focus, amplify them, and make them available for analysis. Each radio telescope comprises an antenna mounted on a structure, accompanied by at least one receiver device to detect the incoming signals. Due to the long wavelengths of radio waves and the faintness of cosmic radio sources, radio telescopes require significant size and employ highly sensitive receivers to capture and analyze these signals. However, they are also susceptible to interference from modern electronics in addition to synchrotron radiation from cosmic-ray electrons in the interstellar magnetic field that contributes the majority of the continuum emission, heavily dominating both Galactic and extragalactic foregrounds at the relevant frequencies. As a

result, it is crucial to accurately model and subtract these foregrounds, while implementing effective measures to shield radio telescopes from RFI.

1.5.1 Dish and Feed Antenna

Different types of antennas are utilized in radio astronomy, depending on the frequency of operation and the intended applications. Wire antennas like dipoles, yagis, and spirals are suitable for wavelengths below ~ 1 meter (300 MHz). However, as wavelengths increase, wire antennas become impractical due to their limited collecting area, prompting the preference for parabolic reflectors, which offer versatility and enhanced sensitivity. The parabola is a useful mathematical shape that forces incoming radio waves to bounce up to a single point above it, called a focus as shown in Figure 1.5. The ability of a radio telescope to distinguish fine details in the sky called the angular resolution, depends on the ratio of the wavelength (λ) of observations to the diameter (D) of the dish antenna as given by the Rayleigh criterion:

$$\theta = 1.22 \times \frac{\lambda}{D} \quad (1.19)$$

where θ is the angular separation in radians. In other words, to get finer detailed views of the sky, the result of that simple equation needs to be a very small number. The parabolic reflector (or dish) is often specified in terms of the diameter of the dish D and the focal-length-to-diameter ratio f/D which represents the size and shape (curvature rate), respectively. The

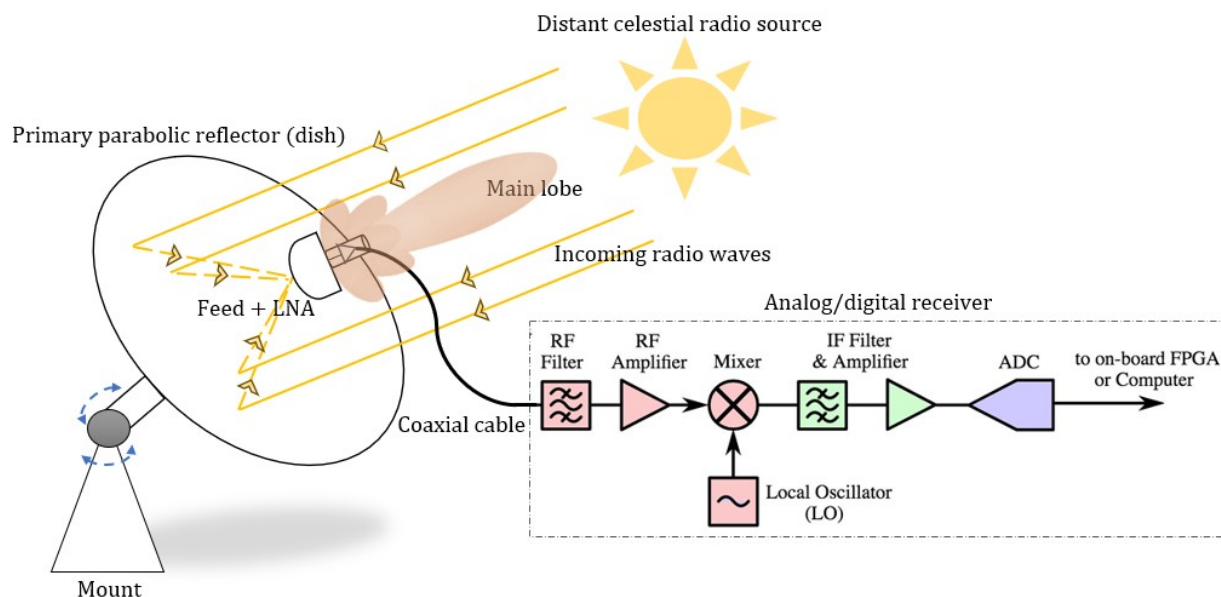


Figure 1.5: This schematic illustrates the key components of a radio telescope, including the parabolic dish, feed antenna, and receiver. The dish collects incoming radio waves, focusing them onto the feed antenna at the focal point. The feed antenna then converts the radio waves into electrical signals and amplifies them, which are then processed by the receiver for further analysis.

feed is the component of the antenna that translates incoming electromagnetic radiation into an analog voltage signal and is placed at the focus of the reflector. Many antenna designs require structures to hold the feed in place, and these structures block part of the aperture. Hence, the effective collecting area (A_{eff}) when pointed directly at a source may not be the same as the physical area (A_{phy}) of the aperture. The ratio between them, $\eta = A_{\text{eff}}/A_{\text{phy}}$, can be used to define the aperture efficiency. An antenna (or radiation) pattern is a graphical representation of the radiation properties of an antenna as a function of direction and illustrates how the strength of the radiation emitted or received by the

antenna varies with the angle relative to the antenna. The radiation patterns of dish antennas are highly directive, concentrating most of their energy into a narrow beam known as the main lobe as shown in Figure 1.5. Smaller lobes, called sidelobes, appear alongside the main lobe, representing directions with less energy radiation. Sidelobes are often minimized to reduce interference and direct most of the signal strength toward the intended target. The electromagnetic performance of a feed is often verified using simulation software like computer simulation technology (CST) Studio Suite ([Dassault Systemes, 2021](#)) which helps optimize the feed design for improved gain, bandwidth, efficiency, and reduced sidelobes ([Shamshad and Amin, 2012](#)).

If the pattern is measured at a distance far enough from the antenna such that the angular field distribution remains independent of the distance from the antenna, and this distance is significantly greater than both the operating wavelength λ and the dimensions of the antenna, it is classified as the far-field pattern. In the far-field (or Fraunhofer) region R_{ff} , electromagnetic waves are essentially planar and are approximated as $R_{\text{ff}} \geq 2D^2/\lambda$. Measurements at lesser distances, $R_{\text{nf}} < 2D^2/\lambda$, yield near-field patterns, which are a function of both angle and distance. In the near-field region, the electromagnetic field strength varies significantly, and the fields are characterized by reactive components where the electric and magnetic fields are not in phase. Adjusting the feed beam to become smaller may lead to underutilization of the dish, as a significant portion remains unilluminated. When the feed beam is too wide, a considerable portion misses the dish and

falls onto the ground, known as ground spillage. Efforts to minimize ground spillage often result in underilluminating the dish, representing a primary trade-off in telescope construction.

1.5.2 Analog and Digital Electronics

Analog components are fundamental for several tasks, primarily signal amplification and filtering. In radio astronomy, weak signals received by antennas need to be amplified to levels suitable for further processing and analysis. In the front-end electronics stage, typically positioned directly after the feed, low-noise amplifiers (LNAs) are utilized to amplify the weak incoming signals. If the early stage of an amplifier is noisy, the noise is amplified along with the signal, making it difficult to remove and reducing the system's sensitivity. Thus, particular emphasis is placed on minimizing the noise level of the initial amplifier (Chiong et al., 2021). The back-end electronics stage typically includes mixers for frequency conversion and filters as shown in Figure 1.5. Mixers operate with local oscillators—tunable signal generators that mix their signals with incoming RF signals—facilitating the downconversion of received signals to lower intermediate frequencies (IF) for easier processing. Filters are employed to pass only frequencies within a specified range while attenuating those outside this range, thus improving the signal-to-noise ratio (SNR). After conversion to IF, the signal is usually once again amplified using IF amplifiers before analog-to-digital conversion (ADC) (Taylor et al.,

1999). The digital stage comprises ADCs that digitize the received analog signal by sampling the continuous signal to create a discrete one, adhering to the Nyquist-Shannon sampling theorem, which requires the sampling rate to be at least twice the highest frequency in the signal to prevent aliasing and performs channelization to sort the broadband digitized signal into narrower frequency channels, enabling effective wideband signal processing (Zhang et al., 2023). Digital signal processing (DSP) techniques, such as filtering, Fourier transforms, and correlation are later performed to extract valuable information from the digitized signals, enabling detailed analysis and interpretation of astronomical data.

1.6 Thesis Outline

This thesis focuses on characterizing the dish surface deformations of two upcoming radio interferometers: the Hydrogen Intensity Real-time Analysis eXperiment (HIRAX) and the Canadian Hydrogen Observatory and Radio-transient Detector (CHORD). These instruments have a primary objective of studying dark energy through 21-cm intensity mapping of BAOs and will also serve as valuable platforms for discovering new pulsars and transient radio sources. In Chapter 2, I will introduce the principles of radio interferometry and discuss the scientific objectives and operational aspects of both HIRAX and CHORD. Additionally, I will delve into the Deep-Dish Development Array (D3A), which acts as a prototype and testing ground for the technologies used in HIRAX and CHORD, including

feeds, electronics, and reflector fabrication methods. Since real-world radio telescopes have reflectors with slight deviations from a perfect paraboloid, it is essential to study the impact of these surface errors on the telescope's performance. Chapter 3 marks the beginning of the original contributions of this thesis, detailing a few metrology techniques such as laser tracking, photogrammetry, and finite element analysis (FEA) along with the mathematical tools required to quantify the surface deformations of reflectors. In Chapter 4, I will explain how to incorporate surface deformations obtained from metrology into electromagnetic (EM) simulations and explore the impact of these deformations on the beam patterns of the reflectors. Chapter 5 develops the concept and mathematical framework of beam covariance, serving as a robust metric for quantifying the spatial variations between the beams. In addition, I will demonstrate the usage of this metric to calculate the beam perturbations due to systematics associated with dish surface deformations and feed offsets/tilts from their nominal positions. Finally, Chapter 6 summarizes the key findings of this thesis and outlines prospects for future research endeavors.

Chapter 2

Principles of Radio Interferometry

2.1 A Two-Element Radio Interferometer

According to the Rayleigh criterion, the maximum achievable angular resolution of a parabolic dish is determined by the formula $1.22\lambda/D$. Thus to attain increased resolution, a radio telescope needs a larger diameter. The largest steerable single-dish telescope is the Green Bank telescope ([Prestage et al., 2009](#)) with an aperture size of 100 m. For a wavelength (λ) of 20 cm, the maximum resolution achieved is around $8'$. Thus to obtain a $1''$ resolution, one would require an aperture size of ≈ 50 km which is economically and technically challenging. Interferometers address this issue by splitting a large dish into several smaller telescopes spread across a wide area and then combining their signals. This approach effectively creates a virtual telescope with resolving power equivalent to a single

dish whose diameter matches the maximum distance between the individual telescopes in the array. The following texts about interferometry basics are referenced from the works of [Condon and Ransom \(2016\)](#) and [Thompson et al. \(2017\)](#).

Consider the 1D geometric situation shown in Figure 2.1 where two identical dishes with effective apertures A_1 and A_2 are separated by the baseline vector \vec{b} that points from antenna 1 to antenna 2. Both dishes point in the same direction specified by the unit vector \hat{s} , and θ is the angle between \vec{b} and \hat{s} . Let there be a cosmic source located in the farfield of both telescopes, meaning it is sufficiently distant that the incident wavefront can be approximated as a plane wave over the distance $|\vec{b}|$. Each antenna receiver measures the electric field¹ of the source as

$$E(t) = B \cos(2\pi\nu t + \phi), \quad (2.1)$$

where B is the amplitude of the electric field, $2\pi\nu = \omega$ is the angular frequency, and ϕ is the phase at time $t = 0$. The plane waves from a distant cosmic source must travel an extra distance $\vec{b} \cdot \hat{s} = b \cos \theta$ to reach antenna 1, so the output voltage of antenna 1 is the same as that of antenna 2, but it lags in time by the geometric delay

$$\tau_g = \frac{\vec{b} \cdot \hat{s}}{c}. \quad (2.2)$$

This electric field $E(t)$, which is perpendicular to the direction of propagation, induces

¹For simplicity, let us assume the radiation emitted by the source is monochromatic and has frequency ν .

voltage at the two antennas which oscillates at the same frequency as the incoming wave.

Let the output voltages of antennas 1 and 2 at time t be written as

$$V_1 = V \cos[\omega(t - \tau_g)] \quad , \quad V_2 = V \cos(\omega t), \quad (2.3)$$

where the signal V_1 from antenna 1 is delayed by the extra time, τ_g , compensating for the additional time it takes for the waves to reach the reflector. The two voltages are then multiplied to form a cross-correlation and integrated as

$$r(\tau_g) = \frac{1}{2T} \int_{-T}^{+T} V \cos[\omega(t - \tau_g)] V \cos(\omega t) dt = \left(\frac{V^2}{2} \right) \cos(\omega \tau_g), \quad (2.4)$$

where the integration time $2T$ is much larger than $1/\nu$ to drop off the high-frequency components and capture the more stable, low-frequency components to gain the essential characteristics of the signal, such as its amplitude and phase variations. Because the voltages V_1 and V_2 are proportional to the electric field generated from the source and the voltage gain of two antennas, the correlator output amplitude (which is in the units of power) $V^2/2$ is proportional to the flux density of the source S multiplied by $(A_1 A_2)^{1/2}$. As the Earth rotates, resulting in the rising and setting of the source, the angle θ varies, leading to sinusoidal fluctuations in the correlator output $r(\tau_g)$. These fluctuations, known as fringes, exhibit maximum frequency when the source is at the zenith ($\theta = 90^\circ$) and minimum when the source is rising or setting ($\theta = 0^\circ$ or 180°). The resolution $\Delta\theta$ that a

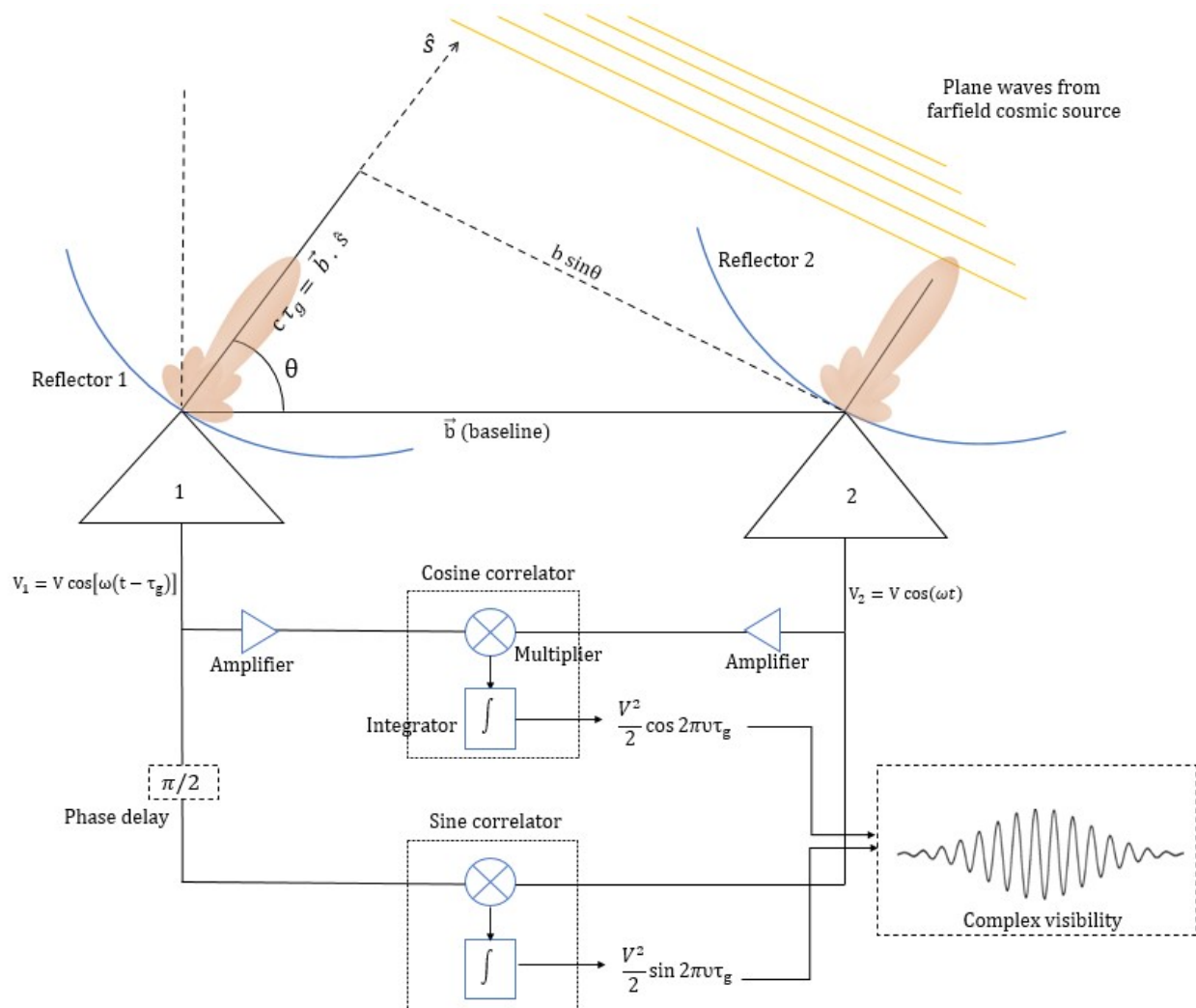


Figure 2.1: Block diagram representing the components of a two-element radio interferometer observing a distant point source with \vec{b} being the baseline vector pointing from antenna 1 to antenna 2. The output voltage V_1 of antenna 1 is the same as the output voltage V_2 of antenna 2, but it is delayed by the geometric delay τ_g representing the additional light-travel delay it takes for the waves to reach the reflector 1. The output voltages are amplified, multiplied, and integrated by the sine and cosine correlator to yield visibilities.

radio interferometer can achieve is given as

$$\Delta\theta = \frac{\lambda}{|b|}, \quad (2.5)$$

where the farther apart you place the antennas the finer the detail you can see in an astronomical object. Since the total collecting area is equivalent to the sum of the reflecting surface areas of all of the antennas in an interferometer, the larger the collecting area, the weaker the astronomical signal that the interferometer can detect.

As the functions V_1 and V_2 that represent the signals may be complex, the cosine response of the correlator (R_C) as shown in Equation 2.4 is sensitive only to the real (symmetric part of the source distribution) part of the interference pattern. To measure the imaginary (anti-symmetric) part of the fringe patterns, a sine correlator is implemented by inserting a 90° phase delay into the output of one antenna ($\cos(\omega t - \pi/2) = \sin(\omega t)$), yielding the cross-correlated output

$$R_S = \left(\frac{V^2}{2}\right) \sin(\omega\tau_g), \quad (2.6)$$

which is analogous to cosine response R_C but with a $\sin(\omega\tau_g)$ oscillatory component. The combination of cosine and sine correlators is called a complex correlator and the response of an interferometer with a complex correlator is called complex visibility \mathcal{V} , defined as

$$\mathcal{V} = R_C - iR_S, \quad (2.7)$$

where R_c and R_s are the real and imaginary outputs from the cosine and sine correlators respectively. The visibility amplitude A and the phase ϕ are then given as

$$A = \left(R_C^2 + R_S^2 \right)^{1/2} \quad , \quad \phi = \tan^{-1}(R_S/R_C). \quad (2.8)$$

Till now we had assumed that the radiation from the source was monochromatic. For a quasi-monochromatic extended source containing a narrow bandwidth $\Delta\nu$ centered around ν with brightness distribution $I(\hat{s})$, the cosine and sine correlator response is given as

$$R_C = \int I(\hat{s}) \cos(2\pi\vec{b}\cdot\hat{s}/\lambda) d\Omega \quad , \quad R_S = \int I(\hat{s}) \sin(2\pi\vec{b}\cdot\hat{s}/\lambda) d\Omega. \quad (2.9)$$

The complex correlator response or complex visibility for such an extended source can then be written as

$$\mathcal{V} = \int I(\hat{s}) e^{-2\pi i \vec{b}\cdot\hat{s}/\lambda} d\Omega. \quad (2.10)$$

where the complex visibility \mathcal{V} is defined as the two-dimensional Fourier transform of the sky brightness distribution. Thus to summarise, an interferometer measures components of the visibility function by forming interference fringes between the apertures whose separation is given by baseline length in wavelengths, and the orientation is given by the orientation of the baseline. The contrast and phase of these fringes give the amplitude and phase of the visibility function, providing essential information about the spatial structure and intensity distribution of radio sources in the sky.

2.1.1 Noise and System Temperature

The radiation from a blackbody at a temperature T , described by the Planck spectrum, can be approximated in the radio regime using the Rayleigh-Jeans approximation as

$$B(\nu) = \frac{2h\nu^3}{c^2} \frac{1}{e^{h\nu/K_B T} - 1} \approx \frac{2K_B T}{\lambda^2}, \quad (2.11)$$

where K_B is the Boltzmann's constant (1.38×10^{-23} J/K) and h is the Planck's constant (6.626×10^{-34} J/Hz). Thus a source brightness distribution $B(\nu)$ can be expressed in temperature units with no relation to the physical temperature of the source as

$$T = \frac{\lambda^2}{2K_B} B(\nu). \quad (2.12)$$

As detailed in Chapter 1, radio telescopes function by converting electromagnetic waves into output power, which can be traced from their reception by the feed through the receiving system. This output power P per unit frequency is usually expressed as antenna temperature², $T_A = P_A/K_B$, which is the temperature of a resistor whose thermal noise would yield an equivalent power per unit frequency as given by the Nyquist relation. A source with a flux density S increases the antenna temperature by $T_A = (A_{\text{eff}}S)/2K_B$, where A_{eff} is the effective collecting area as discussed in Section 1.5.1. Natural radio emissions from the CMB, discrete astronomical sources, the Earth's atmosphere, and the

²Remember that the antenna temperature does not correspond to the physical temperature of the antenna

ground produce random broadband noise that is almost indistinguishable from the noise generated by a warm resistor or receiver electronics. It is hence convenient to describe noise power (P_N) from any noise-like source as noise temperature, $T_N = P_N/K_B$, which is the equivalent noise power per unit bandwidth generated by a resistor of temperature T . This noise temperature affects the signal at multiple stages—initially at the antenna, where spillover from the warm ground, RFI, and signals from unwanted sources are captured and later in the receiver, through the electronic components and cables involved in transporting, amplifying, and filtering the signal (Taylor et al., 1999). The temperature equivalent to the total power from all sources referenced to the input of an ideal receiver connected to the output of a radio telescope is called the system temperature T_{sys} . When observing a blank sky, T_{sys} reflects the total random noise in the system and is essential to minimize this temperature to achieve optimal performance. Because the noise from various sub-systems of the radio telescope is uncorrelated, they can be added up linearly and generally be written as

$$T_{\text{sys}} = T_{\text{sky}} + T_{\text{source}} + T_{\text{spill}} + T_{\text{rec}} + \dots \quad (2.13)$$

Here, T_{sys} includes non-thermal radiation from galaxies at low frequencies and contributions from the CMB which is approximately 2.73 K. The temperature contribution from the astronomical source being observed is referred to as T_{source} , which is usually much smaller than T_{sys} . T_{spill} accounts for spillover radiation that the feed antenna picks up from

the ground around the edge of the reflector. T_{rec} represents the noise power generated by the receiver, modeled by an equivalent circuit with an ideal noiseless receiver whose input is a resistor of temperature T . Additional contributions come from atmospheric conditions (such as absorption, emission, and scattering processes) and the presence of lossy elements in the feed path that absorb some of the signal energy as it travels from the antenna to the receiver such as cables and filters. The system noise level is a critical factor in determining the sensitivity and SNR of a receiving system. The uncertainty in the system temperature, which reflects this noise, is quantified by the radiometer equation:

$$\sigma = \frac{T_{\text{sys}}}{(\Delta\nu \cdot \tau)^{1/2}}, \quad (2.14)$$

where τ is the integration time and $\Delta\nu$ is the bandwidth. This equation illustrates that the uncertainty in measuring the system noise temperature decreases with the square root of the number of samples averaged together. Consequently, increasing the observing or integration time τ leads to a reduction in the root mean square (RMS) error σ , thereby enhancing the SNR and confidence of having detected the source. Understanding and quantifying these various noise sources is crucial for optimizing the performance of radio telescopes and extracting meaningful scientific data from observations.

2.1.2 The Importance of Redundancy

Interferometric arrays come in various configurations, each tailored to specific scientific objectives. Imaging arrays, tasked with producing detailed sky images, require data across various length scales to accurately depict celestial objects and rely on maximizing the number of distinct baselines to capture different spatial frequencies (Monnier and Allen, 2012). This requirement for a multitude of baselines consequently leads to an irregular arrangement of array elements. On the other hand, compact arrays with telescopes closely and uniformly spaced, excel at studying large-scale structures and extended sources. These arrays concentrate on specific length scales and construct regular, grid-like configurations with as many identical baselines as possible to generate statistical information for a particular science goal (Liu et al., 2010). Having identical baselines provides heightened sensitivity at certain scales but sacrifices the wide range of baselines required for images. To achieve redundancy, each element of the array including dishes, feeds, and electronics must be identical. A notable advantage of a redundant array is the ability to average data from identical baselines before storage, resulting in a substantial reduction in data storage requirements (Newburgh et al., 2016). Imperfections in the telescope's construction, such as surface deformations, feed misalignment, and electronic imperfections can pose significant challenges in achieving the desired redundancy. These small non-redundancies can thus introduce systematic errors or distortions in the 21-cm power spectrum estimates. Our goal to perform 21-cm intensity mapping through BAO structures demands a high

degree of geometric redundancy and stringent reflective surface standards, and thus characterizing the redundancy between dishes stands as the main focus of this thesis. In the next section, I will discuss two upcoming redundant radio interferometers that will perform 21 cm intensity mapping of the northern and southern skies.

2.2 Overview of HIRAX and CHORD

The Hydrogen Intensity Real-time Analysis eXperiment (HIRAX) and the Canadian Hydrogen Observatory and Radio-transient Detector (CHORD) are twin radio interferometers being developed for deployment in the Karoo desert, South Africa, and the Dominion Radio Astrophysical Observatory (DRAO) in Kaleden, Canada, respectively. The primary objective of these interferometers is to use 21-cm intensity mapping to provide high-precision measurements of BAOs, which serve as a standard ruler for cosmological distance measurements as discussed in Chapter 1. These instruments will allow us to trace the large-scale structure of the universe and track the formation and evolution of cosmic structures over time thus, enabling more accurate determinations of the expansion history of the universe and the properties of dark energy. HIRAX operates within a frequency range of 400-800 MHz, corresponding to a redshift range of $0.8 < z < 2.5$, while CHORD covers a broader bandwidth from 300 to 1500 MHz, focusing on redshifts < 3.7 . HIRAX

will initially feature a 256-element array³ and is designed to observe approximately 15,000 square degrees of the southern hemisphere (Crichton et al., 2022). CHORD’s central array consists of 512 dishes, complemented by two distant outrigger stations, as depicted in Figure 2.2(a). Both HIRAX and CHORD utilize six-meter parabolic composite dishes characterized by a focal ratio of $f/0.21$, maximizing the collecting area over the minimum baseline lengths and minimizing cross-talk between neighboring dishes (Kuhn et al., 2021). These arrays operate in a drift-scan mode, maintaining a fixed elevation most of the time, with manual adjustments in zenith angle within a $\pm 30^\circ$ range to build up sky coverage. HIRAX plans to include at least two outrigger stations with the longest baseline of approximately 1000 km, each consisting of 8 to 16 dishes (Crichton et al., 2022). CHORD’s outrigger stations will be equipped with a 90×10 -meter CHIME-like cylinder with a focal ratio of 0.25 and a 64-dish array matching the central array’s specifications (Vanderlinde et al., 2019) as given in Table 2.1

The HIRAX feed is a dual-polarization cloverleaf antenna as shown in Figure 2.3(b) that integrates the first stage low noise amplifier (LNA) with the antenna balun to reduce the system noise (Newburgh et al., 2016). Each feed is housed inside a cylindrical can, which circularizes the beam and reduces cross-talk between dishes. The amplified radio frequency (RF) signals are transmitted to the digital backend via a radio frequency over fiber (RFoF) system. In this system, an RFoF transmitter with a laser diode converts the incoming RF

³The HIRAX array is planned to eventually consist of 1024 elements in the future, but this thesis focuses on the currently funded 256-element array.

signals into optical signals. These signals are then converted back to RF at the central hub ~ 1 km away from the telescopes, using an RFoF receiver. The signals are further amplified and filtered before being transmitted to the digital backend, which houses an FX correlator. The F-engine handles digitization and channelization using an ICE-based system (Bandura et al., 2016). For the initial HIRAX-256 array, 32 ICE boards will be deployed, each processing 16 inputs from 8 dual-polarization feeds. The GPU-based X-engine performs full N^2 correlation on the incoming data from 512 inputs⁴, producing raw visibility data for each baseline. The ultrawideband dual-polarisation feed of CHORD (MacKay et al., 2022), on the other hand, is a modified version of the exponentially tapered slot antenna (vivaldi) and quad-ridged flared horn antenna designs as shown in Figure 2.2(b). CHORD currently plans to use coaxial cables to transport signals to the digital backend, as the CHORD collaboration has experience with this reliable technology from working with CHIME. For the digital backend processing, CHORD is exploring two potential designs for the F-engine: the ICE-based system used in CHIME, which would need modifications to handle the full CHORD bandwidth, and the RF-System-on-Chip (RFSoc) based system, which is currently being evaluated and can process the entire CHORD band, offering a smoother and stable signal chain (Hendricksen, 2023). More details about these systems will be discussed later in this chapter.

HIRAX and CHORD are next-generation radio instruments that focus on bandwidth,

⁴Each antenna measures two orthogonal polarizations, hence $2 \times 256 = 512$.

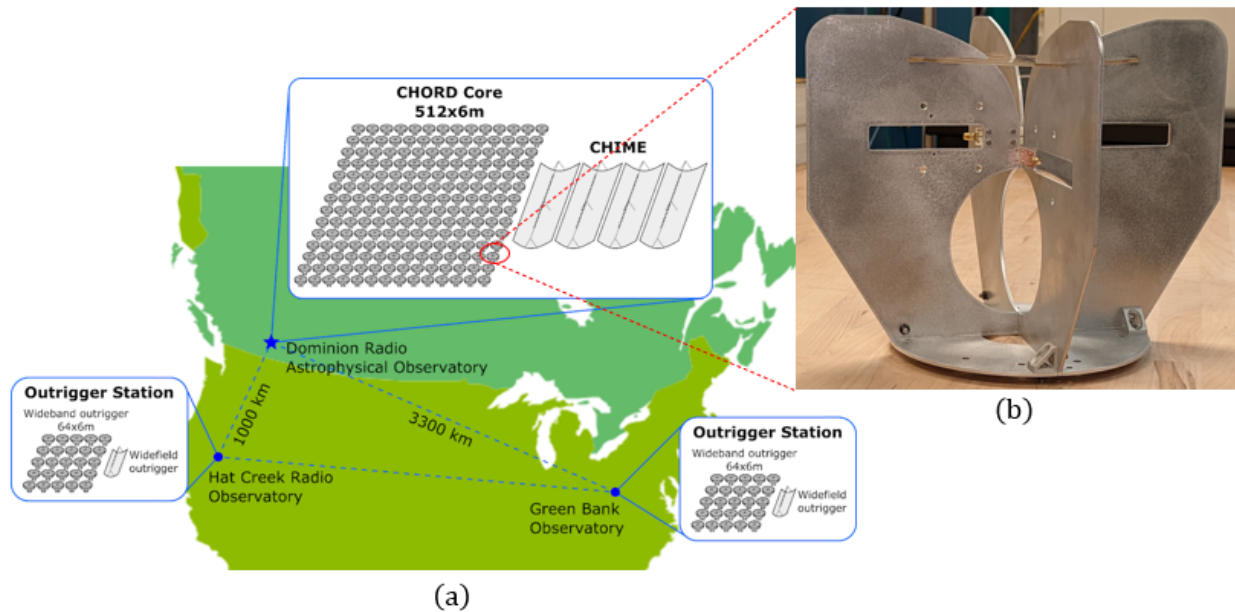


Figure 2.2: Figure (a) from [Vanderlinde et al. \(2019\)](#) illustrates a large array of ultrawideband (UWB) dishes, covering 300-1500 MHz and positioned adjacent to CHIME at DRAO. This central array is augmented by two outrigger stations, with the longest baseline at a distance of ~ 3000 km. Each outrigger station features a 90×10 -meter CHIME-like cylinder operating at 400-800 MHz, along with an array of 64 UWB 6-m dishes, covering 300-1500 MHz. Figure (b) from [MacKay et al. \(2022\)](#) shows the dual-polarization CHORD feed antenna including the microstrip baluns, which are terminated by SMA connectors.

collecting area, and sensitivity as key metrics to achieve their scientific objectives. To maintain a manageable total data volume, both HIRAX and CHORD will leverage their redundant configurations to average visibilities within groups of identical baselines as discussed in the previous section. These instruments aim for centimeter-level precision in baseline spacing and strict adherence to beam conformity among dish elements to take advantage of that redundancy. In addition to their primary goal of 21-cm intensity

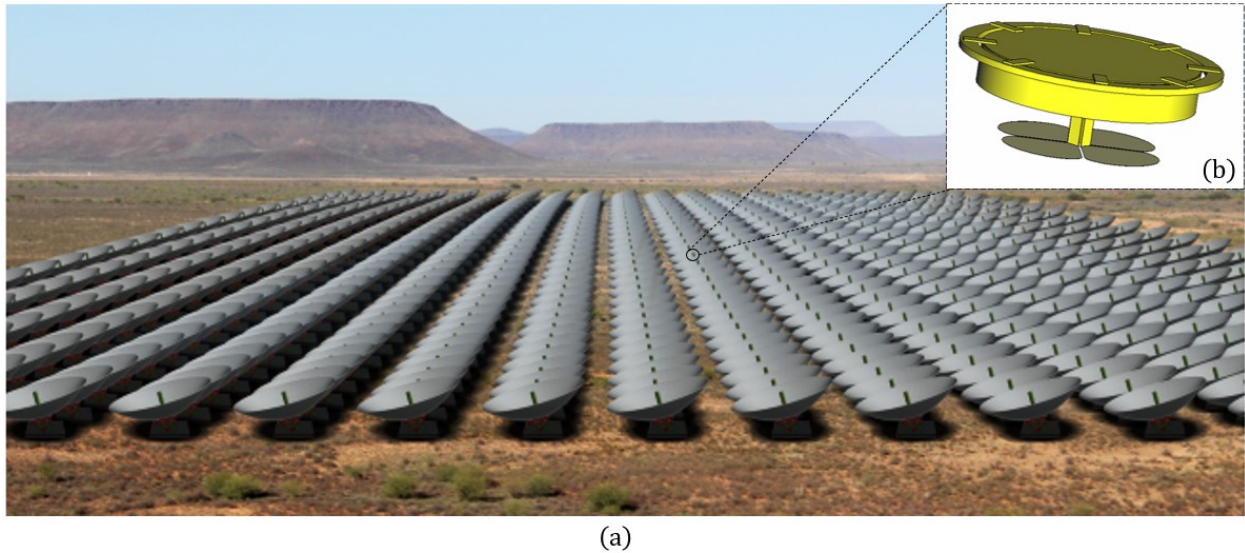


Figure 2.3: Illustration (a) from [Crichton et al. \(2022\)](#) shows a rendering of the complete 1024-element HIRAX array located in the Karoo desert, South Africa. The array is densely packed to enhance sensitivity on BAO angular scales and features highly redundant baselines to aid in calibration and correlation. Figure (b) depicts the dual-polarization cloverleaf antenna, designed with a metal can structure to serve as a backplane and minimize spillover and crosstalk. The HIRAX antenna feed includes first-stage LNA integrated into the antenna itself, which helps reduce feed noise.

mapping, both HIRAX and CHORD are excellent platforms for the following scientific studies:

Fast Radio Bursts (FRBs): FRBs are mysterious, millisecond bursts of radio light of unknown origin coming from far outside our Milky Way galaxy. Localizing FRBs to their host galaxies and specific environments is crucial for understanding their nature and potential as cosmic probes. FRBs can be broadly classified into two categories: repeating and non-repeating. Repeating FRBs emit multiple bursts from the same location over time, while

Table 2.1: Instrumental parameters of HIRAX and CHORD.

Specifications	HIRAX	CHORD
Dish diameter (m)		6
Dish focal ratio		0.21
Number of dishes	256	512
Operating frequency (MHz)	400-800	300-1500
Field of view (degree ²)	15 - 56	5 - 130
System temperature (K)	50	30
Collecting area (m ²) ^a	7200	14,400
Resolution ^b	$\sim 0.2^\circ - 0.4^\circ$	$\sim 0.05^\circ - 0.28^\circ$

^aThe total collecting area for an interferometer is equivalent to the sum of the reflecting surface areas of all of the antennas. For HIRAX-256, this is given by $\pi \times (3 \text{ m})^2 \times 256$ and for CHORD, its $\pi \times (3 \text{ m})^2 \times 512$.

^bNote that the resolution of an interferometer is dependent on the longest baseline (b) and the wavelength observed as given by $\sim \lambda/b$. For example, given a 32×32 regular grid with 7 m spacing (Newburgh et al., 2016), the longest baseline for HIRAX-1024 is ~ 300 m.

non-repeating FRBs have been observed as a single burst with no subsequent emissions detected from the same source (Petroff et al., 2019). It is still unclear whether the two types share a common physical origin and differ only in their activity rates, or if they arise from entirely different astrophysical processes. One of the key properties of FRBs is their dispersion measure (DM), which is the total column density of free electrons between the source of the burst and the observer. The DM provides a measure of the distance to the FRB, as the signal is dispersed by the intergalactic medium, causing lower frequencies to arrive later than higher frequencies (Reischke and Hagstotz, 2023). The CHIME telescope's

extensive collecting area and large field-of-view have proven highly effective, resulting in the detection of over 500 FRB sources, including 18 repeaters (Amiri et al., 2021) in the frequency range of 400-800 MHz. While CHIME has set a high standard for FRB detection, CHORD, and HIRAX can greatly complement and enhance localization efforts through their outrigger stations. CHORD’s wide bandwidth is especially effective for accurately estimating dispersion delays across different frequencies, thereby enabling precise localization.

Search for Pulsars: Pulsars are highly magnetized and rapidly rotating neutron stars that emit beams of radio light from their magnetic poles and function as precise cosmic clocks. Discovering more pulsars raises the chances of finding relativistic binary neutron-star systems, which are ideal testbeds for theories of relativistic gravity. CHORD and HIRAX, with their potential to increase the number of known galactic pulsars⁵ from approximately 3,000 to over 10,000 (Vanderlinde et al., 2019), can serve as powerful engines for pulsar discovery and efficient pulsar monitoring telescopes. These discoveries would greatly complement precision timing experiments of millisecond pulsars in detecting long-wavelength gravitational waves generated by merging supermassive black holes.

Multi-wavelength Science: HIRAX and CHORD’s extensive sky coverage will significantly overlap with current and upcoming optical/infrared galaxy and lensing surveys, such as DESI (Aghamousa et al., 2016), Euclid (Amendola et al., 2018), as well as ground-based CMB surveys like the Simons Observatory (Ade et al., 2019), South Pole

⁵The Australia Telescope National Facility (ATNF) [Pulsar Catalog](#) contains more than 3000 pulsars discovered so far.

Telescope (SPT)-3G (Benson et al., 2014), and Advanced Atacama Cosmology Telescope Polarization (ACTPol) (Henderson et al., 2016), that will enable cross-correlation studies and multi-wavelength follow-ups. Additionally, CHORD’s ultra-wide bandwidth will help investigate the origin and evolution of magnetic fields in the universe by mapping the magnetoionic environment of the interstellar and circumgalactic medium using Faraday tomography, among other secondary science goals.

2.3 Deep-Dish Development Array (D3A)

To achieve precision cosmology using 21-cm intensity mapping techniques, HIRAX and CHORD interferometers must meet stringent requirements for design, alignment, and calibration. To develop redundant front-end electronic systems, feeds, and precise metrology methods, the deep-dish development array (D3A) was deployed at DRAO. This small interferometric prototype array includes two 3-meter and three 6-meter composite dishes as shown in Figure 2.4(a) and (b) and serves as a test-bed for various technologies such as composite dishes and mount design, antenna feeds, low noise amplifiers, the signal conditioning chain, and the readout system for HIRAX and CHORD. The initial demonstration of D3A involved two 3-meter composite reflectors equipped with passive cloverleaf feeds used by the CHIME telescope, with a baseline length of 20 meters between the dish mounts (Islam and Ölçek, 2020). Later, three D3A 6-m dishes (referred to as D3A6), were deployed in the east-west direction as shown in Figure 2.4(b) to develop and

demonstrate the performance and systematic control of the key technologies that will enable CHORD and HIRAX to meet its target specifications (Islam et al., 2022). The separation between Dishes 2 and 3 is 6.5 m while the separation between Dish 2 and Dish 1 is 39 m. In the following sections, I describe a few key technologies that are developed for HIRAX and CHORD through D3A6.

2.3.1 Composite Dishes

To achieve a redundant array, it is crucial that identical dishes are manufactured with repeatable systematic errors to minimize variability among them. The D3A6 dishes, which are prime-focus parabolic reflector antennas with a 6-meter diameter and a focal ratio⁶ of 0.25, are constructed from monolithic composite materials with an embedded aluminum reflective layer. These materials, known for their high strength-to-weight ratios, are ideal for minimizing gravitational distortion of the dish surfaces when the telescopes are tilted, thus enabling the production of low-cost radio dishes with precision surfaces. The HIRAX and CHORD dishes will be produced using a limited number of molds to ensure consistency across the array. The D3A6 dishes are currently manufactured from a 4-piece, 6-meter mold using the vacuum infusion process. This involves placing reinforcing materials into the mold, sealing it, and then applying vacuum pressure to draw resin into

⁶Initial designs for HIRAX and CHORD set the focal ratio at 0.25, which was also implemented in the D3A6 prototype. However, subsequent electromagnetic simulations and testing of the D3A6 dish and feed demonstrated that a focal ratio of 0.21 provided better performance by reducing reflections between antenna elements and cross-coupling between the feeds.

the mold, ensuring complete impregnation and minimizing voids. This technique is commonly used in composite manufacturing to produce high-quality, consistent parts. For HIRAX and CHORD, the final dishes will be made using a single-piece mold to further improve consistency. The D3A6 reflectors are constructed from three layers of fiberglass material (vectorply E-LTM 18084⁷), which is transparent to radio frequencies. The embedded aluminum mesh serves as the reflective surface, and its surface and electromagnetic uniformity are assessed using a technique known as reflectometry, which uses a cylindrical resonance cavity to measure the depth of the embedded mesh surface by analyzing shifts in resonance frequencies (Nitto, 2023; Pieters, 2021). Dish 1 features a circular ring support structure, whereas dishes 2 and 3 have square ring supports. These supports are created using separate molds and affixed to the back of the reflectors (Islam et al., 2022). The dishes are mounted on stainless steel supports, which are anchored to the foundation with steel studs as shown in Figure 2.4(b). The feed support structure is composed of four fiberglass tubes that connect to the central hub and align with feet-locating features on the reflector surfaces. Additionally, a ridgepole structure, which is supported both at the rim and by the feed support framework, provides stability for the radome cover which acts as a weatherproof enclosure.

⁷A specific type of reinforcing fabric used in composite manufacturing. The E in the name typically denotes E-glass, a common type of fiberglass known for its excellent electrical insulation properties and resistance to high temperatures.

2.3.2 Radio Frequency over Fibre System

Traditional coaxial cables have long been used in radio astronomy for transmitting analog signals over short to moderate distances. In a typical setup, the analog signal from the telescope feed is amplified by a low-noise amplifier (LNA) and then sent via coaxial cable to an electronics hut, where the signals are digitized and correlated to obtain visibilities. Although coaxial cables have a well-known performance, they face challenges such as significant signal attenuation over long distances and susceptibility to electromagnetic interference, which can degrade the signal quality (Crichton et al., 2022). Radio frequency over fiber (RFoF) technology offers a promising and less expensive solution for large-array radio instruments. In this technology, an RFoF transmitter with a laser diode converts RF signals into optical signals, which are transmitted via fiber optic cables to a central processing hub. There, the optical signals are converted back into RF by an RFoF receiver equipped with a photo-detector and passed to the digitizer. Tests conducted on the CHIME two-element prototype interferometer, which includes two 9-meter parabolic reflectors each equipped with a four-square feed above a ground plane and spaced 19 m apart, demonstrated the RFoF system's effectiveness in terms of dynamic range, gain, and phase stability, establishing it as a cost-effective solution for analog signal transport in large-array configurations. Detailed performance information about this system is provided in Mena et al. (2013). The D3A6 array is currently being used to demonstrate and test the RFoF signal transport system. While HIRAX plans to employ RFoF technology to

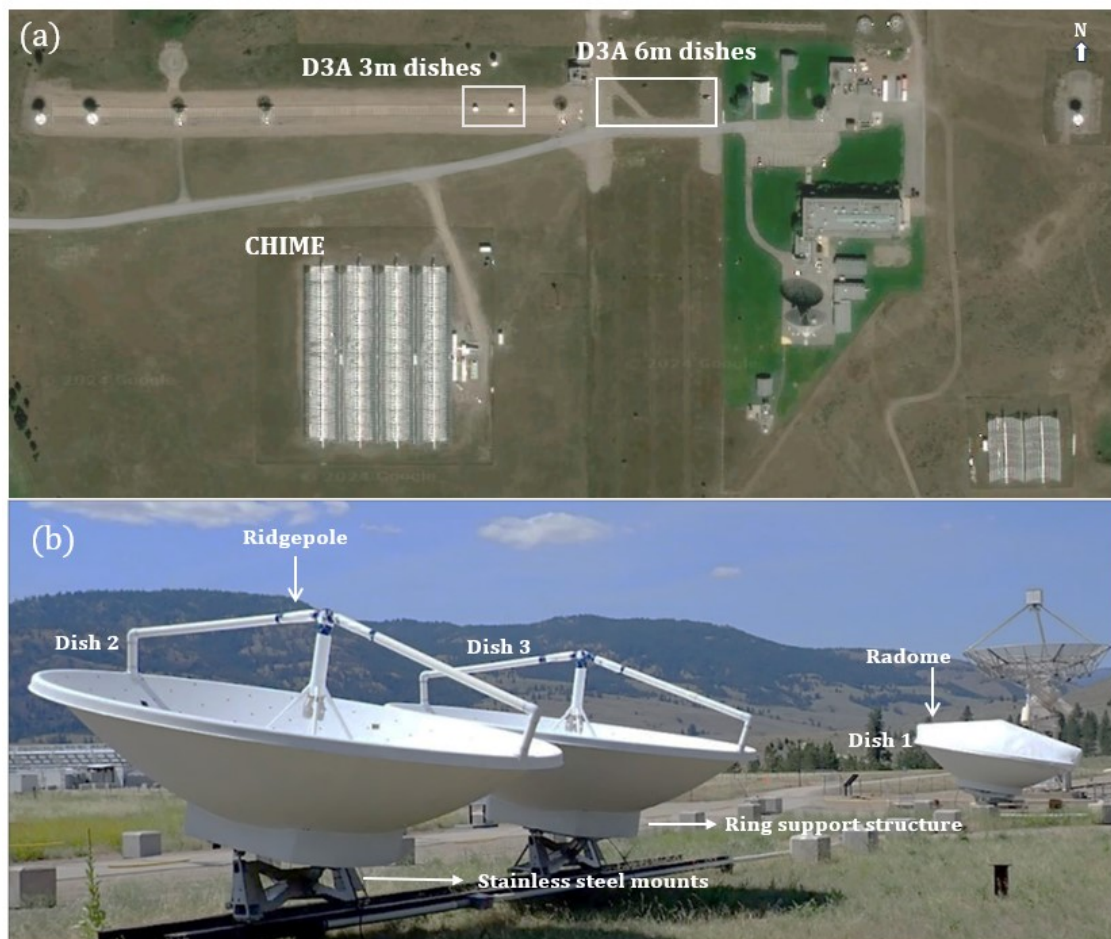


Figure 2.4: (a) displays an aerial view of the DRAO site, marking the positions of the D3A 3-meter dishes, D3A 6-meter dishes, and the CHIME array. (b) This close-up image (from <https://sites.google.com/view/chord-observatory>) features the D3A 6-meter dishes, highlighting key components such as the ridgepole, radome, ring support structure, and stainless steel mounts. Dish 1 is the west-most dish while Dish 2 is the east-most dish.

transmit analog signals to the central hub approximately 1 km away from the telescope, particularly beneficial for its planned 1024-element array, CHORD currently plans to use coaxial cables due to established familiarity and experience from CHIME.

2.3.3 ICE-system vs RFSoc based F Engine

The ICE-based system, developed at the McGill Cosmology Instrumentation Laboratory, provides a cost-effective solution for large-scale digitization, channelization, and corner-turn operations of signals from upstream analog systems ([Bandura et al., 2016](#)). This system, which uses FPGA-based motherboards, has been deployed as the digital backend system for the South Pole Telescope, Simons Array, and CHIME. HIRAX, operating within the same frequency range as CHIME, can utilize this proven ICE-based F-engine for the frequency range of 400 to 800 MHz. For its initial 256-element array, HIRAX will employ 32 ICE boards, each managing 16 inputs from 8 dual-polarization feeds, along with a polyphase filter bank and FFT-based pipeline for channelization. In contrast, CHORD's wide bandwidth of 300 to 1500 MHz presents challenges for the ICE system, particularly with band-splitting and analog filter design, which can lead to aliasing and potential data loss around Nyquist frequencies. To address these challenges, the RF-System-on-Chip (RFSoc) based design, using the AMD Zynq Ultrascale+ RFSoc FPGA, offers a promising alternative with superior ADC performance, higher sampling rates, and greater dynamic range ([Hendricksen, 2023](#)). This design reduces the need for complex band-pass filtering, improving frequency response

smoothness, which is crucial for 21-cm intensity mapping. The RFSoc firmware is currently being characterized and tested on D3A6 to assess its on-sky performance.

Chapter 3

Metrology on D3A6 Composite Dishes

In Chapters 1 and 2, I highlighted the critical need for high-precision calibration in the new generation of radio interferometers, CHORD and HIRAX, which aim to detect BAO structures through neutral hydrogen emissions. Achieving precision cosmology with these instruments requires stringent design, alignment, and calibration standards, as any non-redundancies in subsystems pose significant challenges to the performance needed to meet scientific goals. The HIRAX telescope mechanical assembly (TMA) requirements document ([HIRAX Collaboration, 2021](#)) outlines the accuracy and precision standards for the telescope mechanical structure, including the foundation, dish mount, reflector, and receiver support structure, as dictated by the scientific objectives. Systematics related to the reflector surface and receiver perturbations¹, discussed in this thesis, are among the

¹More about receiver perturbations and their requirements will be discussed in Chapter 5.

critical factors impacting these requirements and demand careful consideration. For example, the TMA document mandates that the reflector surface must have an accuracy of 5 mm or better relative to the ideal paraboloid and a precision of better than 1 mm relative to the mean best-fit paraboloid of revolution. Similarly, the error requirements for D3A6 fabrication and assembly, as outlined in [Islam et al. \(2022\)](#), specify that the dish surface must achieve an accuracy of 1.20 mm and a precision of 0.20 mm. To meet the requirement of manufacturing identical dishes and minimizing variability among them, precise metrology methods based on laser tracker and photogrammetry technologies have been developed. This chapter formulates the mathematical framework necessary to analyze data from these methods and discusses the implementation and results of these metrology techniques in characterizing the surface deformation of the D3A6 dishes.

3.1 Laser Tracker Analysis

A laser tracker is a precision measurement instrument used in metrology to accurately determine the position and orientation of objects in three-dimensional space through laser technology. This device is used in measuring molds and dish parts, aligning the elevation axes of dishes, and assessing dish surface measurements within an array. The procedure involves measuring the 3D coordinates of the dish surface by tracking a retroreflective²

²Unlike standard reflective surfaces that scatter light in various directions, retroreflective materials reflect light rays along the same path they came from. This property allows laser tracker instruments to easily detect and accurately measure the distance to the target.

target as it is maneuvered from one point to another by the user across the surface under examination. The laser beam, upon reflection from the retroreflector and returning to the tracker, allows a distance meter within the tracker to calculate the distance to the target. The gathered coordinate data is then transferred to metrology software, establishing the x , y , and z coordinates for each measured point. The D3A6 mold and dishes are measured using the **FARO vantage laser tracker**, which has a distance measurement accuracy of $15 \mu\text{m} + 5 \mu\text{m}/\text{m}$, and angular measurement accuracy of $20 \mu\text{m} + 5 \mu\text{m}/\text{m}$, to study the surface deformations and understand the different errors associated with them (Islam and Ölçek, 2020). The raw (unprocessed) laser tracker datasets³ of the mold (before and after dish 1 fabrication) and the three 6-meter D3A dishes captured while pointing at the zenith are presented in Figure 3.1. Since the data points are irregularly spaced and vary in density due to the collection process, it is crucial to uniformly grid the datasets to ensure consistent comparison of process repeatability and verification. The primary objectives of this analysis are to (i) calculate the surface RMS errors of the D3A6 dishes using laser tracker datasets to evaluate the accuracy and precision of the dish surfaces, (ii) investigate the surface changes in the mold after the dishes are pulled from it to better understand the fabrication process and its impact on dish surface quality, and (iii) calculate the RMS errors between different dishes to assess the repeatability of the manufacturing and fabrication processes. This analysis facilitates the evaluation of the consistency and reliability of dish production.

³The laser tracker and photogrammetry datasets are provided by *Mohammad N Islam* from the National Research Council Canada.

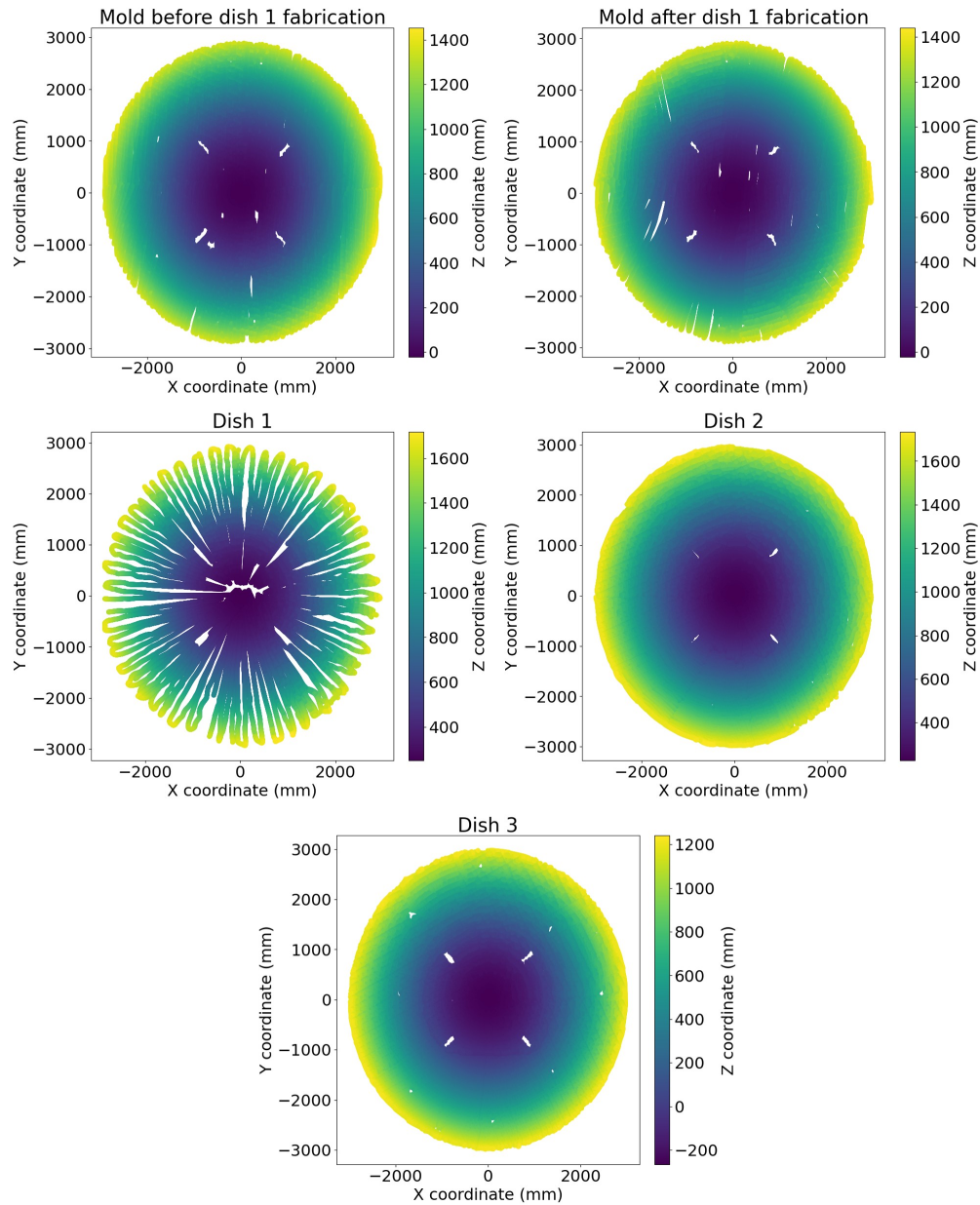


Figure 3.1: Laser tracker datasets of mold before and after dish 1 fabrication, dish 1, dish 2, and dish 3. The boresight axis of these dishes is not aligned with the zenith and the vertex is offset from the origin. The four cross-shaped empty gaps observed in each dataset denote the feet-locating features used to mount the feed support structure.

3.1.1 Nomenclature and Methodology

Before conducting the best-fit procedure for determining the RMS errors, it is essential to undertake data pre-processing. Let us consider x , y , and z to be the world coordinate system where the z -axis is aligned vertically with the zenith. The laser tracker datasets do not have an inherent absolute frame of reference and typically have an arbitrary position offset and orientation angle as shown in Figure 3.2. Hence, it is necessary to perform rotational and translational operations to align the boresight axis with the zenith and position the dish vertex at the origin. Before getting into the analysis procedure, a few variables and their definitions used in this work are introduced in Table 3.1. The following procedure and terminologies are used in laser tracker analysis to calculate the surface RMS errors.

1. Let us denote the original datasets shown in Figure 3.1 as D_i , where $i = 1,2,3...M$ represents the individual dishes and is defined within the global coordinate system x , y , and z . Note that D_i has to be rotated along the x , y , and z axes to align its boresight axis with the zenith as shown in Figure 3.2.
2. As discussed above, it is necessary to rotate and translate D_i so that the boresight axis aligns with the zenith and the vertex is positioned at the origin. This is carried out using the rotational matrices

$$R_x = \begin{bmatrix} 1 & 0 & 0 \\ 0 & \cos(\alpha) & -\sin(\alpha) \\ 0 & \sin(\alpha) & \cos(\alpha) \end{bmatrix}, \quad R_y = \begin{bmatrix} \cos(\beta) & 0 & \sin(\beta) \\ 0 & 1 & 0 \\ -\sin(\beta) & 0 & \cos(\beta) \end{bmatrix}, \quad R_z = \begin{bmatrix} \cos(\gamma) & -\sin(\gamma) & 0 \\ \sin(\gamma) & \cos(\gamma) & 0 \\ 0 & 0 & 1 \end{bmatrix}, \quad (3.1)$$

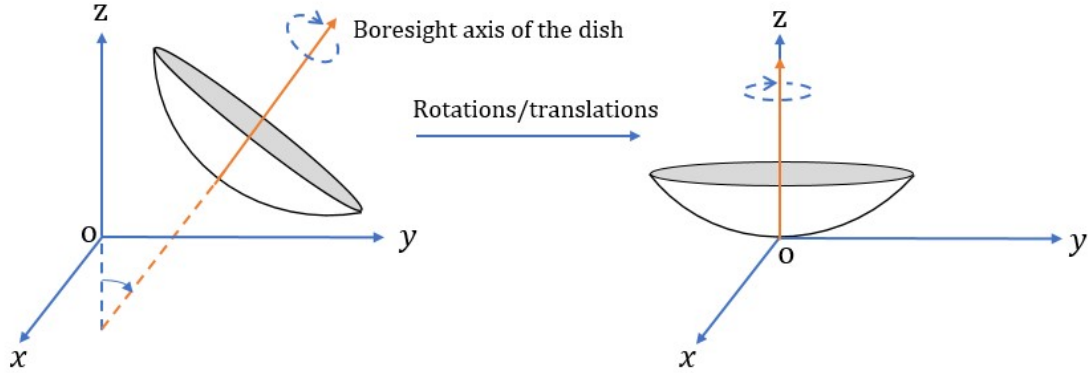


Figure 3.2: This figure depicts the rotational and translational corrections to be performed before fitting the data to the paraboloid equation. The boresight axis is aligned with the zenith using the rotation matrices and the offsets from the origin are calculated using the best-fit parameters which are then subtracted from D'_i to position the dish at the origin.

where R_x , R_y and R_z are the rotations with respect to x , y and z axes (global coordinates) with angles α , β and γ respectively.

3. To find the optimal rotation angles, a minimization procedure is carried out using SciPy's ([Virtanen et al., 2020](#)) *minimize* python package. First, D_i is rotated by trial rotation angles α , β and γ along x , y and z axes to yield the rotated data, D'_i . The rotated data D'_i are then fitted to a rotationally symmetric paraboloid equation

$$z - z_0 = a \left((x - x_0)^2 + (y - y_0)^2 \right), \quad (3.2)$$

where x_0 , y_0 and z_0 represent the origin of the paraboloid. Linearizing the above equation gives us

$$z = m_0(x^2 + y^2) + m_1x + m_2y + m_3, \quad (3.3)$$

Table 3.1: List of laser tracker variables and their definitions.

Variables	Definition
D_i	Original datasets in its coordinate frame (x, y, z)
D'_i	Rotated datasets whose boresight axis are aligned with the zenith and the vertex is positioned at the origin.
P_i	Best-fit paraboloid to D'_i .
σ_i	RMS of the best-fit residuals calculated using D'_i and P_i .
\bar{P}	Average of all the BFPs to D'_i .
D'_0	A reference dish chosen from the rotated datasets D'_i .
D''_i	D'_i rotated with respect to the reference dish D'_0 to define the azimuthal clocking across all the dishes.
\bar{D}	Average of all the azimuthally clocked dishes, D''_i .

where $m_0 = a$, $m_1 = -2ax_0$, $m_2 = -2ay_0$, $m_3 = a(x_0^2 + y_0^2) + z_0$. The linear least squares method is employed to fit the data points to the paraboloid equation as

$$m = (A^T \times A)^{-1} * (A^T \times d). \quad (3.4)$$

In this context, m represents an array of best-fit parameters, A is a matrix constructed according to the linearised parabolic equation, and d denotes the dataset. Once the best-fit parameters are found, one can find the focal distance f and offsets from the origin (x_0, y_0, z_0) using the following equations.

$$f = \frac{1}{4a}, \quad x_0 = -\frac{m_1}{2a}, \quad y_0 = -\frac{m_2}{2a}, \quad z_0 = \frac{m_3}{a(x_0^2 + y_0^2)}. \quad (3.5)$$

Let P_i represent the best-fit paraboloid (BFP) for the rotated datasets D'_i given by the equation:

$$P_i = a \left((x - x_0)^2 + (y - y_0)^2 \right) + z_0, \quad (3.6)$$

which once determined, the offsets x_0 , y_0 , and z_0 from the origin are calculated using the fit parameters and subtracted from D'_i to position the dish vertex at the origin. Later, χ^2 is calculated between the rotated data D'_i and its corresponding BFP, P_i as

$$\chi^2 = \sum_{j=1}^N \left(P_{ij} - D'_{ij} \right)^2, \quad (3.7)$$

where i represents the dish number and j represents the individual data points of the dish. Finally, the χ^2 value is minimized using the *minimize* function from the SciPy library in Python, which is designed for numerical optimization and minimizing multi-variable scalar functions. The Broyden–Fletcher–Goldfarb–Shanno (BFGS) quasi-Newton algorithm (Broyden, 1970) is selected which employs gradient evaluations to approximate the Hessian matrix, providing efficient convergence towards the minimum of the function.

4. Once the optimal rotation angles are determined from the above-discussed minimization procedure, the original data, D_i are rotated by the respective rotation angles to obtain D'_i and fitted to the linearised parabolic equation. The RMS of the best-fit residuals, σ_i is then calculated as

$$\sigma_i = \left(\frac{1}{N} \sum_{j=1}^N (P_{ij} - D'_{ij})^2 \right)^{1/2} = \left(\langle P_i - D'_i \rangle^2 \right)^{1/2}. \quad (3.8)$$

5. As discussed in Section 3.1, the laser tracker point clouds show variations in data density.

Due to differences in x and y coordinates and the varying number of data points across different datasets, performing regular gridding of the datasets is crucial. This gridding process ensures consistent comparison and analysis of the data for precision. For instance, Figure 3.3 illustrates two types of regular grids along with the cubic interpolation result for the dataset of dish 2. Grid structure 1 corresponds to a $f/0.21$ 6-m parabolic grid defined by the equation, $z = (x^2 + y^2)/4f$ while grid structure 2 is a uniform rectangular grid with a spacing of 6 mm. Although both grids are suitable for visualizing large-scale residuals, it is critical to consider the irregular edges of the laser tracker dishes. As observed in the figure, the interpolated dataset of grid 2 exhibits uneven edges, which can pose challenges when comparing datasets or when integrating them into simulations. Therefore, the parabolic grid which matches the geometric characteristics of the dish more closely, is preferred for the entirety of this analysis. It is important to note that although the laser tracker data are recorded from $f/0.25$ dishes, the interpolation is performed using an $f/0.21$ parabolic grid. By interpolating the residuals rather than the z coordinates of the datasets, the integrity of the surface variations is maintained. The interpolated residuals are added to the z coordinates of the grid, effectively replicating the original geometric variations of the datasets. The resulting surface error difference

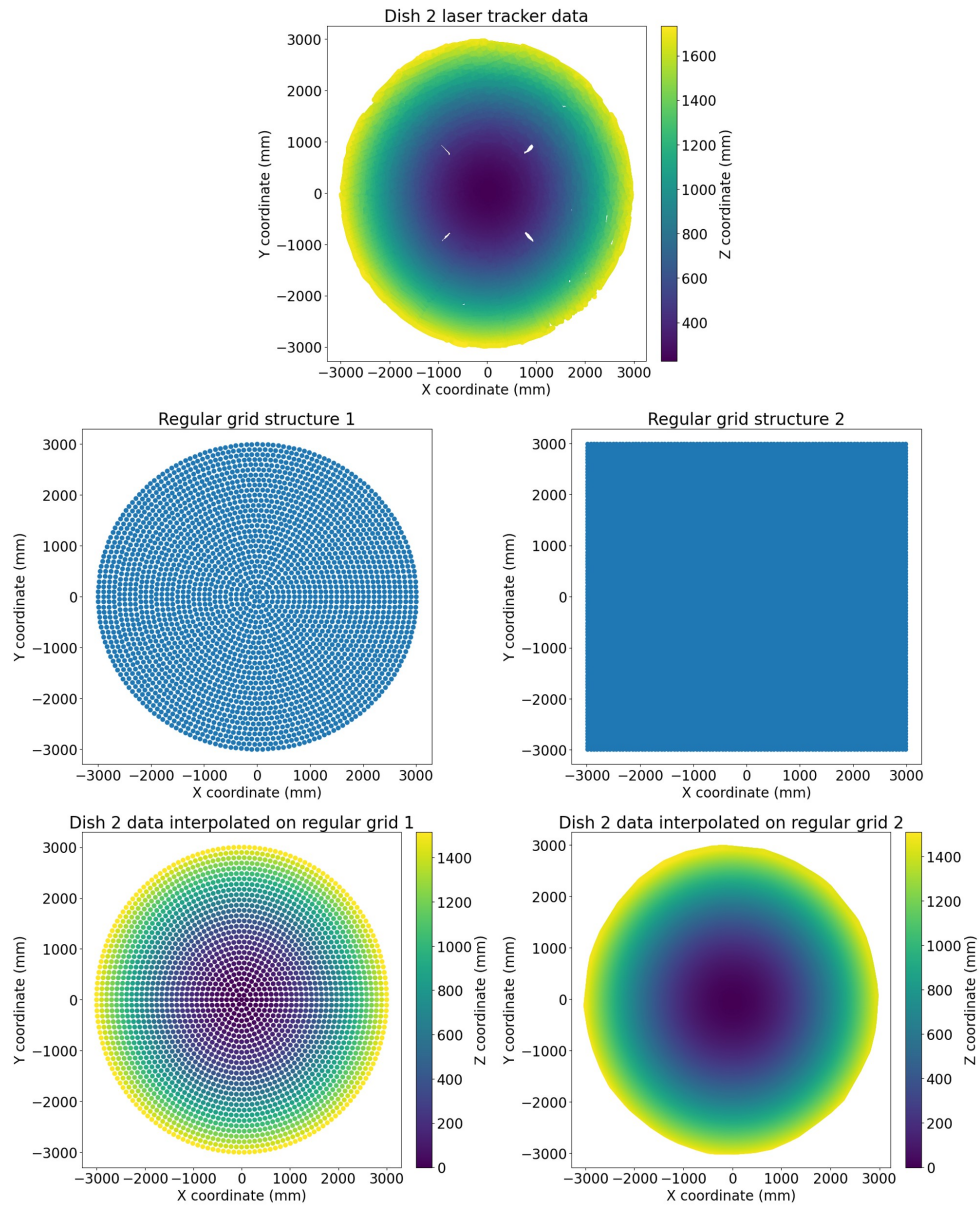


Figure 3.3: Gridding the laser tracker dataset for dish 2 on two distinct types of regular grids. Grid 1 represents an $f/0.21$ parabolic grid, with ~ 5000 grid points while grid 2 is a rectangular grid with around 10000 grid points, offering a higher density of measurement points. The density and spacing between grid points can be adjusted to achieve the desired level of precision and coverage.

between gridding the $f/0.25$ datasets onto an $f/0.21$ grid, as opposed to an $f/0.25$ grid, is on the order of 10^{-14} mm, which is exceedingly small. While it would be totally fine to use an $f/0.25$ parabolic grid for interpolation, the decision to use the $f/0.21$ grid is driven by the need for consistency with the electromagnetic simulations discussed in the next chapter, which employs $f/0.21$ dishes. This consistency is crucial for ensuring accurate comparisons and reliable results across different stages of analysis.

6. Since one of the objectives of this study is to understand the precision of dishes, what we are interested in knowing is the surface variation of each dish with respect to the average of all the rotated/aligned BFPs, \bar{P} given as

$$\bar{P} = \frac{1}{M} \sum_{i=1}^M P_i. \quad (3.9)$$

The resulting residual plots ($D'_i - \bar{P}$) are presented in Figure 3.4 and one notable observation is that the azimuthal clocking is not consistent across the dishes given their symmetrical arrangement around the azimuthal axis. Hence, the dishes have to be rotated with respect to each other in order to define a common azimuthal reference point.

7. After obtaining \bar{P} and the dish residuals, a reference dish denoted as D'_0 (in this case, dish 2) is selected from the pool of rotated/aligned dishes. The remaining D'_i dishes are then rotated with respect to this reference dish. Chi-square values are calculated for the

rotated D'_i (denoted as D''_i) relative to the reference dish D'_0 as

$$\chi^2 = \sum_{j=1}^N (D'_{0j} - D''_{ij})^2, \quad (3.10)$$

where j represents the individual data points of i^{th} dish and reference dish and are minimized following the procedure outlined in step 3. This rotation with respect to a reference dish defines an azimuthal reference point and the resulting azimuthally clocked data are denoted as D''_i . Finally, residuals between the dishes, $D''_i - D''_j$ where $i, j = 1, 2, 3, \dots, M$ represent the individual datasets, are calculated to understand the surface variation among dishes.

3.1.2 Evaluation Metrics

Vertical and perpendicular residuals: Once the data are matched to a BFP using the least squares method, the accuracy of this fit is quantified by calculating the RMS of the residuals, which provides a measure of how well the data conforms to the ideal parabolic shape. *Vertical residuals* (R_{\parallel}) refer to the differences between the measured data points and the fitted paraboloid along the vertical axis and are given as, $P_i - D'_i$. The RMS, σ_i is then calculated as given by Equation 3.8. *Perpendicular residuals* (R_{\perp}), on the other hand, are the orthogonal distances from the measured data points to the best-fit paraboloid surface as shown in Figure 3.5(b). To calculate the perpendicular residuals between D'_i and P_i , the

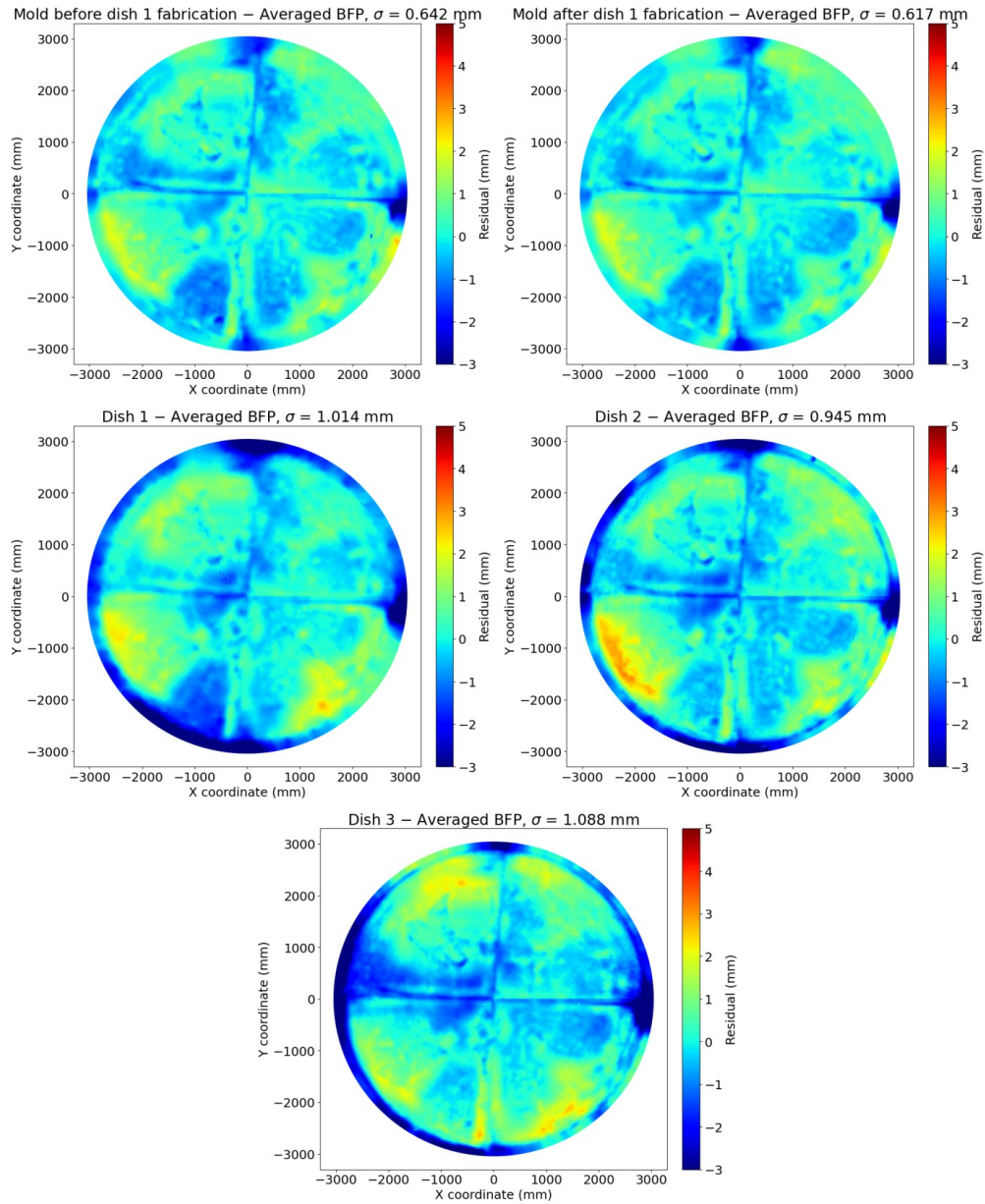


Figure 3.4: Residual plots of the difference between the rotated data D'_i and \bar{P} . The mold is assembled from four pieces, resulting in the joint's imprints on the dishes pulled from it. This accounts for the cross-feature patterns observed in these plots. One can observe that the azimuthal axis of these plots is not aligned with each other and hence D'_i has to be rotated with respect to a reference dish D'_0 before calculating the differences between the dishes

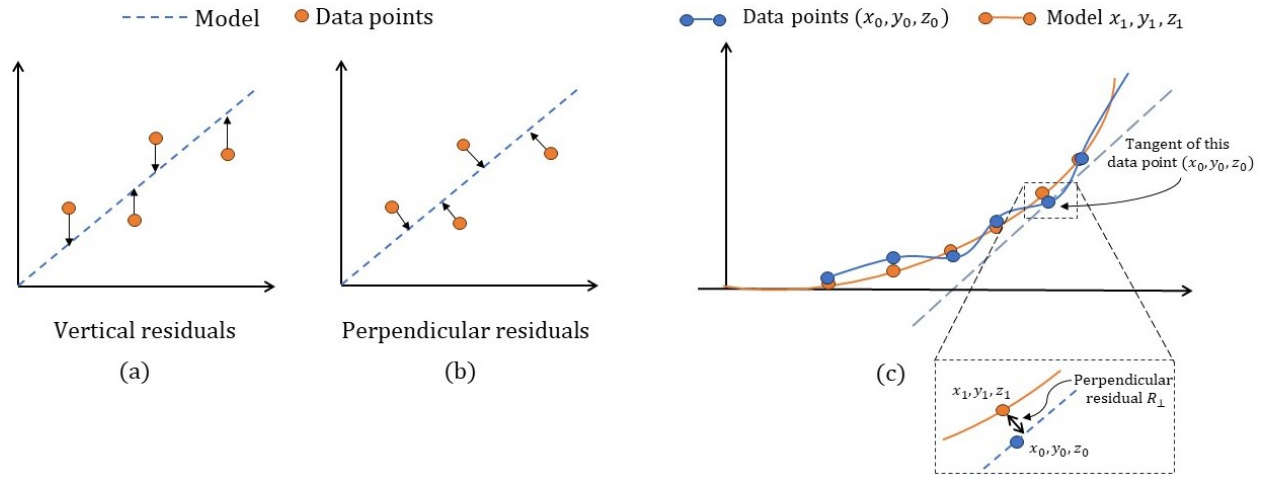


Figure 3.5: Illustration of vertical and perpendicular residuals in a 1D linear fitting model. (a) shows vertical residuals, the differences between the data points (orange), and the model (blue dashed line) measured along the vertical axis. (b) shows perpendicular residuals, the shortest distances from the data points to the model. (c) Once the tangent to the data point (x_0, y_0, z_0) is found, the distance between the tangent line and the corresponding model point (x_1, y_1, z_1) is considered as the perpendicular residual.

equation of the tangent plane to the surface $z = m_0(x^2 + y^2) + m_1x + m_2y + m_3$ —defining D'_i in this case—at a specific point (x_0, y_0, z_0) is determined. Later, the distance d between this tangent plane and the corresponding point on the BFP (x_1, y_1, z_1) is found, as illustrated in Figure 3.5(c).

The equation of the tangent plane to the surface z at a point (x_0, y_0, z_0) is

$$z = z_0 + f_x(x_0, y_0)(x - x_0) + f_y(x_0, y_0)(y - y_0), \quad (3.11)$$

where f_x and f_y are the partial derivatives of the parabolic surface z with respect to x and

y at x_0 and y_0 .

$$f_x = 2m_0x_0 + m_1 \quad , \quad f_y = 2m_0y_0 + m_2. \quad (3.12)$$

The perpendicular residual, which is the shortest distance between the tangent plane at (x_0, y_0, z_0) and the corresponding point on the BFP P_i at (x_1, y_1, z_1) is then given as

$$R_{\perp} = \frac{f_x x_1 + f_y y_1 - z_1 - (f_x x_0 + f_y y_0 - z_0)}{(f_x^2 + f_y^2 + 1)^{1/2}}. \quad (3.13)$$

The RMS errors for both vertical and perpendicular offsets are calculated in the upcoming section. We will see that vertical offsets are well within our accepted tolerances, as perpendicular offsets, being the shortest distance between the data point and the model surface, are usually smaller. Therefore, vertical errors can be considered as the upper limit on the surface errors. Minimizing vertical offsets, rather than perpendicular offsets, simplifies the fitting process, enabling a more straightforward prediction of surface height (z) at given x - y coordinates and easier incorporation of measurement uncertainties.

Accuracy and precision of the dishes: The surface RMS error for each dish i is calculated as Equation 3.8, where $j = 1, 2, 3 \dots N$ represents the total number of data points of i^{th} dish.

The accuracy of the dishes (Islam, 2023) is then calculated from the mean surface RMSE of M dishes as

$$\mu_{dishes} = \frac{1}{M} \sum_{i=1}^M (\sigma_i) \quad (3.14)$$

To understand the precision of the dishes, each dish is compared against two surfaces: (i) The

mean BFP, \bar{P} as discussed in the previous section, $D'_i - \bar{P}$ and (ii) the averaged azimuthally clocked datasets given as $D''_i - \bar{D}$ where

$$\bar{D} = \frac{1}{M} \sum_{i=1}^M D''_i \quad (3.15)$$

While the former evaluates how well each dish conforms to the mean ideal parabolic shape, highlighting the deviations from the desired shape and identifying systematic errors in the dish manufacturing process, the latter assesses the consistency and repeatability of the dishes by averaging out azimuthal variations.

3.1.3 Results and Discussions

The surface errors are obtained as the RMS of the vertical and perpendicular offsets of the data points from the model surface and are tabulated in Table 3.2. According to the error requirements laid out for the D3A6 project, the mold and dish surfaces are required to have an accuracy of 0.65 mm and 1.20 mm respectively (Islam et al., 2022). From Table 3.2, the results are found to be encouraging as the dish surface variations lie within the anticipated surface error budget / sub-millimeter range. Moreover, it can be inferred that the mold surface errors calculated before and after the fabrication of dish 1 are within the requirement of 0.65 mm with the difference being approximately 127 μm . This minimal variation indicates that the mold undergoes negligible degradation during the dish-pulling process, suggesting

Table 3.2: Vertical and perpendicular RMSE of laser tracker dataset, σ_i along with the errors obtained from comparison against \bar{P} and \bar{D} .

Datasets	$D'_i - P_i$ (mm)		$D'_i - \bar{P}$	$D''_i - \bar{D}$
	Vertical RMSE	Perpendicular RMSE	(mm)	(mm)
Mold before dish 1	0.595	0.479	0.642	0.354
Mold after dish 1	0.578	0.464	0.617	0.386
Dish 1	0.825	0.652	1.014	0.527
Dish 2	0.870	0.670	0.945	0.359
Dish 3	1.052	0.806	1.088	0.623

its robustness and reliability in maintaining shape throughout the manufacturing procedure. The accuracy of the dishes is quantified by the mean surface vertical RMSE of M dishes, as defined in Equation 3.14, and has been calculated to be 0.784 mm which is significantly below the dish surface error budget. The residual plots obtained from comparing each dish against both the mean BFP, \bar{P} , and the averaged azimuthally clocked data, \bar{D} , are illustrated in Figures 3.4 and 3.6, respectively and the corresponding RMS errors are presented in Table 3.2. The RMS errors derived from the comparisons $D'_i - \bar{P}$ are noticeably higher than those from $D'_i - P_i$, although they are still within the acceptable error budget. This is expected, as the mean BFP, \bar{P} , is a generalized fit that does not account for the specific surface variations of each individual dataset, unlike their own BFP, P_i . The residual plots against \bar{D} show RMS errors below ~ 0.6 mm, aligning with the HIRAX TMA document's precision requirement of better than 1 mm. While discussions continue on establishing a global method

to define dish precision (Islam et al., 2022), the current analysis offers a convenient tool for assessing the consistency among the dishes. The surface errors of dishes with respect to each other after the azimuthal clocking, $D_i'' - D_j''$ are shown in Figure 3.7. The uneven edges of the laser tracker datasets can introduce systematic errors during interpolation, leading to variations around the edges in the plots. For example, subtracting the mold data before dish 1 fabrication from subsequent datasets shows distinct edge effects, which are not seen when comparing against the mold data after dish 1 fabrication. Therefore, the surface errors shown in Figure 3.7 should be considered as the upper limit, as they include noise introduced during interpolation. Although it is intriguing to observe the nearly identical nature of dish 2 and dish 3 with a difference of $\sim 200 \mu\text{m}$ between them, it is crucial to understand the absence of such similarity in the remaining cases. One possible explanation for the observed differences is that the backup structure for dish 1 differed from that of dishes 2 and 3 as discussed in Chapter 2. This difference is evident in the plots, where comparisons with dishes 2 and 3 show the imprints of the square backing ring, while the comparison with dish 1 (e.g., dish 1 vs mold after dish 1 fabrication) reveals circular imprints. Additionally, the layup direction of the dishes was altered during the data recording process of dishes 2 and 3, contributing to the uncertainties and variations observed. Despite these differences, the variations remain within a maximum value of approximately 0.6 mm and the fact that dishes 2 and 3 turned out to be nearly identical suggests they could serve as reliable representatives for further studies, augmenting the feasibility of achieving redundant arrays.

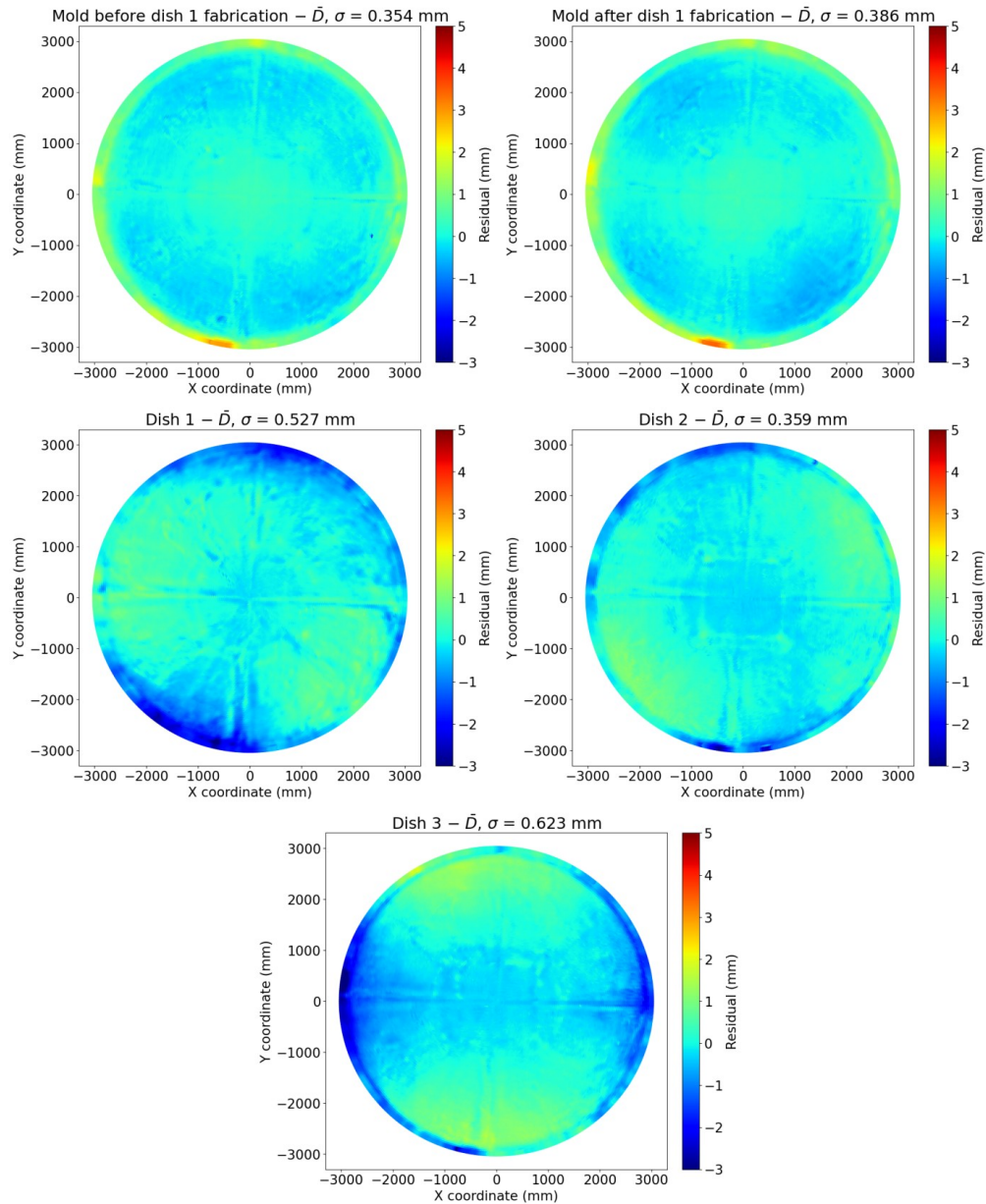
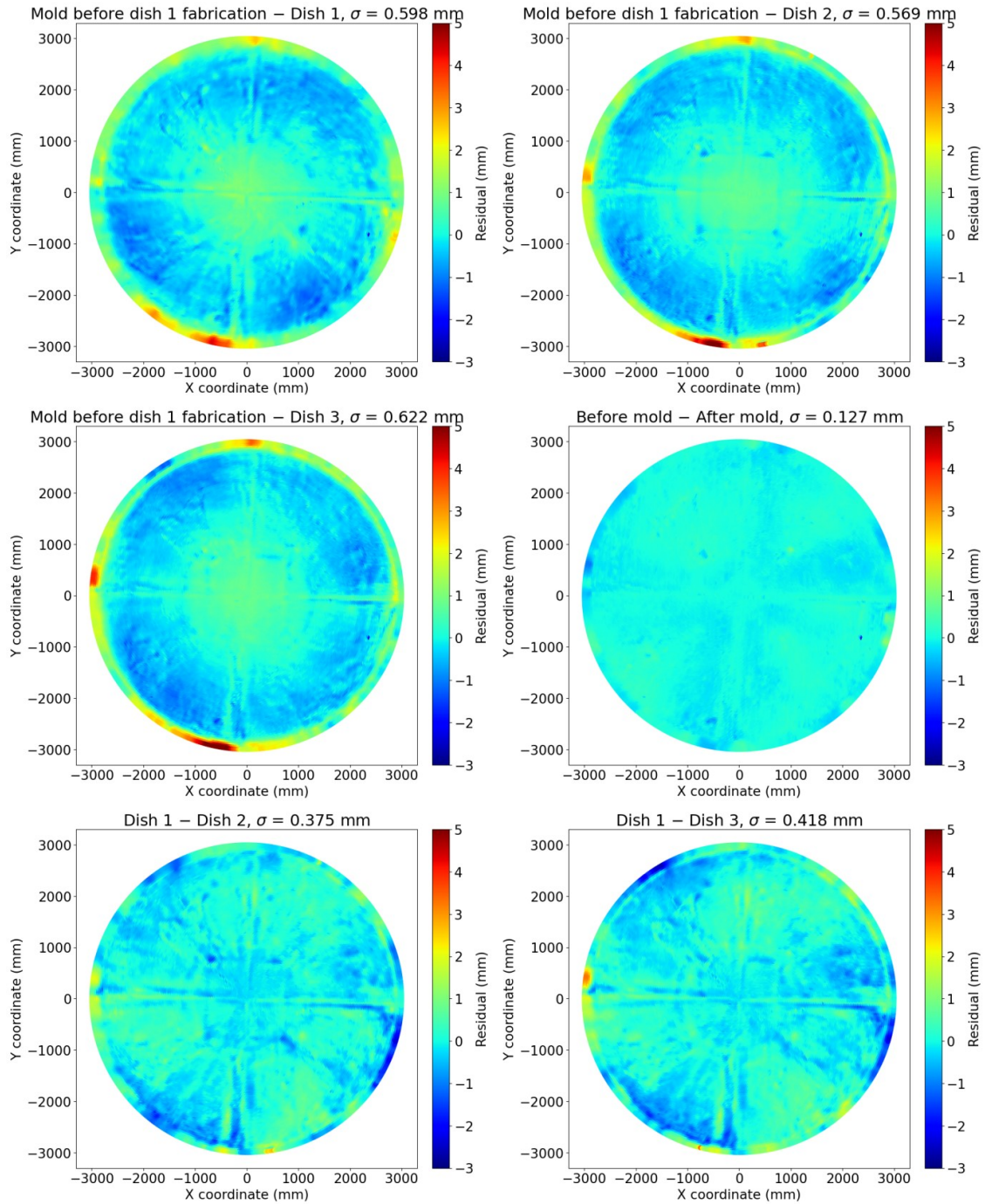


Figure 3.6: This figure shows the residual plots for the datasets of mold before and after dish 1 fabrication, as well as for dishes 1, 2, and 3 compared against the average of azimuthally clocked datasets ($D'_i - \bar{D}$). These residuals highlight the consistency and repeatability of the dishes and include systematics introduced by interpolation due to the uneven distribution of the laser tracker point cloud especially around the edges.



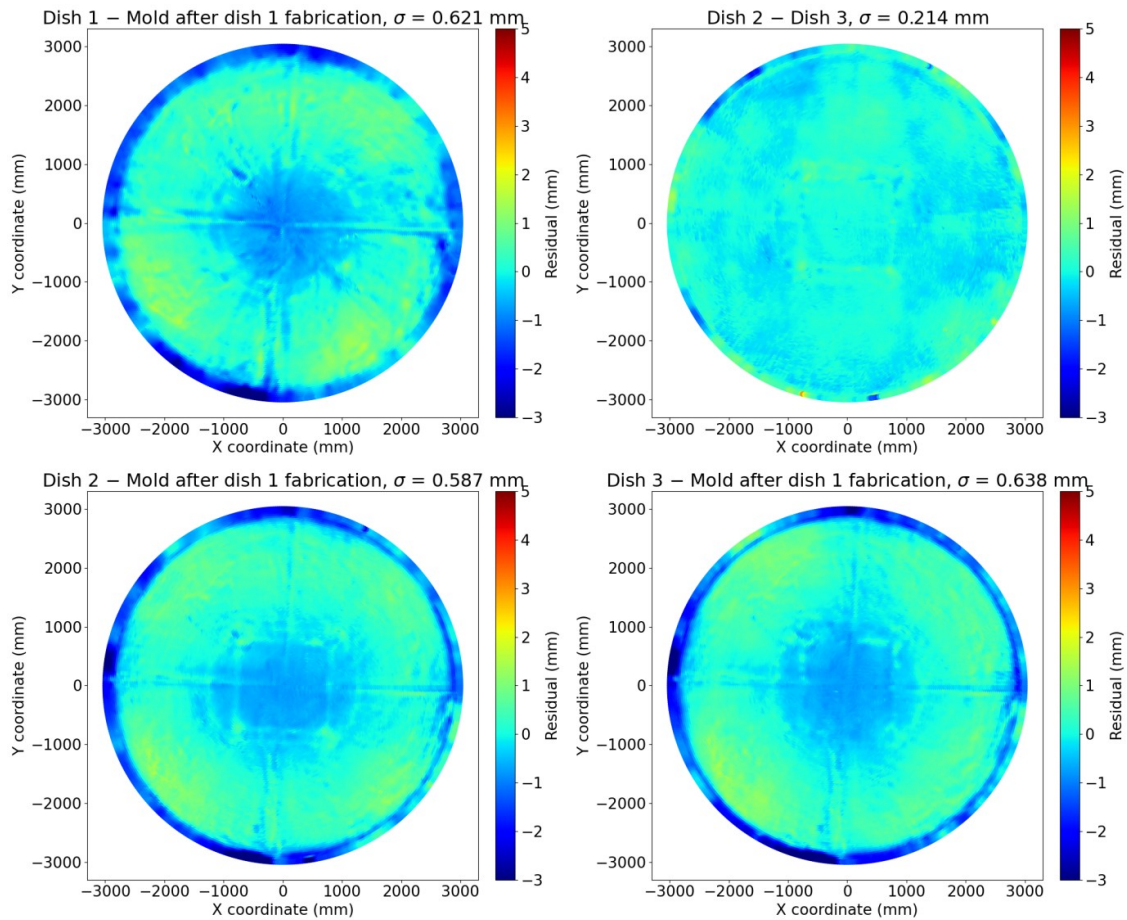


Figure 3.7: Residual plots of the difference between each dish, $D_i'' - D_j''$. Here, the boresight axis of each dish is aligned with the zenith, the vertex is positioned at the origin and the dishes are azimuthally clocked with each other. One cannot see the cross-feature pattern in the ‘before mold–after mold’ and ‘dish 2–dish 3’ plots as the former is the difference between the molds themselves before and after dish 1 fabrication while the latter illustrates the difference between the dishes that exhibit minimal differences with the RMS error of 0.214 mm.

3.2 Photogrammetry Analysis

When using laser tracker metrology to measure the dish surface at off-zenith angles (i.e., $\pm 30^\circ$ from zenith), a significant challenge emerges due to the steepness of the dish surface. As discussed previously, the laser tracker depends on a retroreflective target that is moved across the surface being examined. At higher elevation angles, the dish surface becomes very steep, making it challenging to maintain proper alignment of the target. If the target becomes misaligned or drops out of position, the accuracy of the measurements can be compromised or the measurements may fail altogether. This is where photogrammetry metrology becomes advantageous. It uses a single camera to capture a series of images from multiple viewpoints. Before taking these images, the object must be prepared by marking points of interest with retroreflective targets attached to the dish surface. These targets efficiently reflect light back to the camera. The 3D coordinates of the feature points are then determined by analyzing the images and reconstructing the geometry of the point network as it was during the capture. Thus, photogrammetry metrology allows for surface measurements at various elevation angles and reveals surface distortions caused by gravity. Since photogrammetric measurements are inherently dimensionless, scale bars with known dimensions are often placed in the scene to calibrate the measurements and ensure that the extracted dimensions are accurate. The [V-STARS Silver photogrammetry system](#), which has an accuracy of $5 \mu\text{m} + 7 \mu\text{m}/\text{m}$, was used to record surface deformations of D3A6 dishes. The raw (unprocessed) photogrammetry datasets for dishes 1 and 2, captured at zenith and $+30^\circ$ off the zenith,

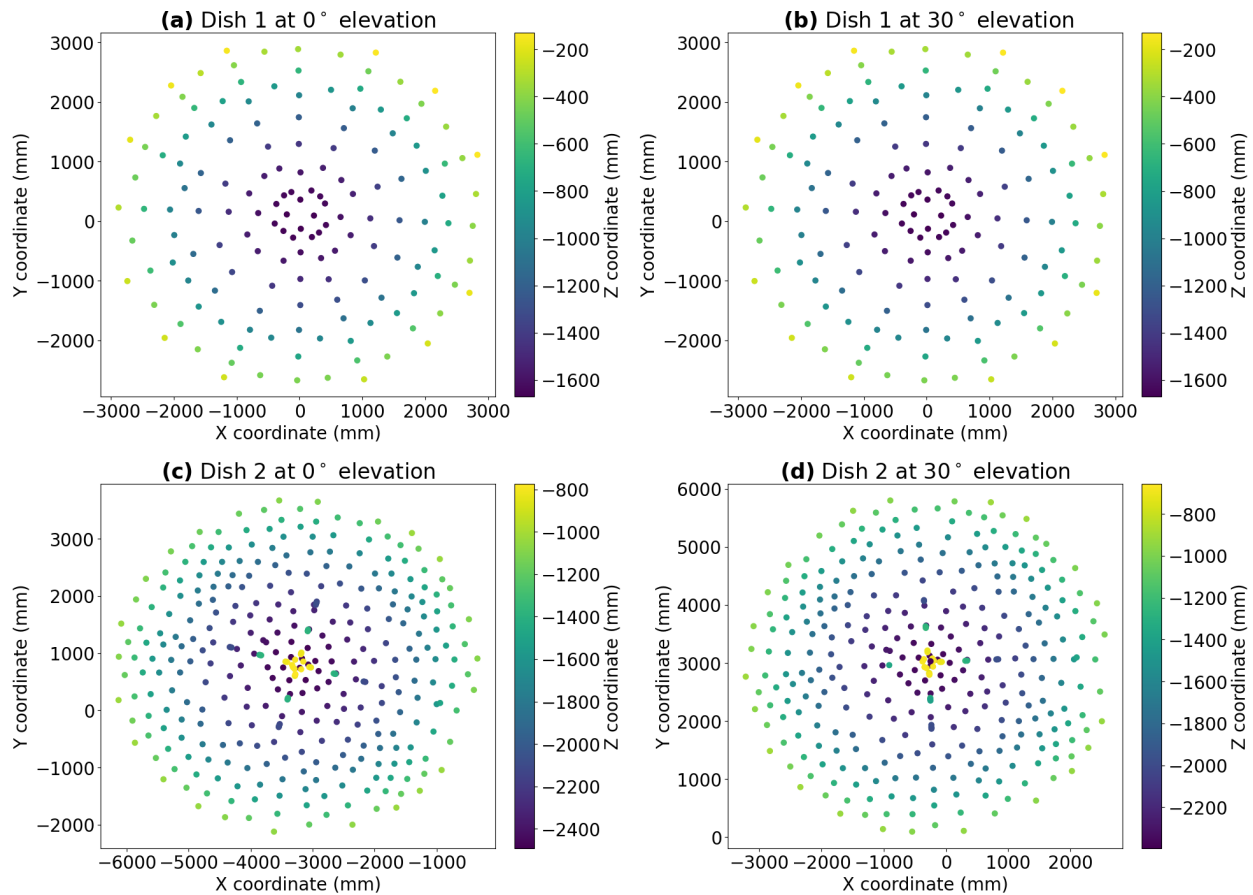


Figure 3.8: The plots presented here display the photogrammetry datasets of dishes 1 and 2 at elevation angles of 0 and 30 degrees, respectively. The boresight axis of these dishes is not aligned with the zenith and the vertex is offset from the origin. The dish 2 dataset contains data points representing the feed support structure which are not required for the surface analysis.

are shown in Figure 3.8. As with the laser tracker analysis, these data need to be regularly gridded for precision analysis of the dishes, following the same procedure outlined in Section 3.1.1. Additionally, the photogrammetry dataset for dish 2 includes data points representing the feed and its support structure, as depicted in Figure 3.8(c) and (d). While these points

can be used to analyze deflections related to the feed support structure, the current analysis is focused solely on the dish surface points, and the additional points will be discarded. The main objectives of this study are to (i) quantify the surface RMS errors of the D3A6 dishes 1 and 2 using photogrammetry datasets at 0 and +30 degrees zenith angles, providing a better understanding of the surface deformations caused by gravity; and (ii) assess how closely the surface deformations obtained from photogrammetry at 0 degrees elevation match those from laser tracker measurements to evaluate their similarity.

3.2.1 Methodology

The analysis of photogrammetry data follows a procedure similar to that used for laser tracker analysis. Initially, the raw data are rotated and translated to align their boresight axis with the zenith and position the dish vertex at the origin, using the minimization procedure described in Section 3.1.1. Once the transformed dataset D'_i and its corresponding BFP are determined, the best-fit residuals are obtained as $D'_i - P_i$. The residual plots are then gridded onto an $f/0.21$ parabolic grid using SciPy's RBFInterpolation. Although the photogrammetry data are recorded from $f/0.25$ D3A6 dishes, we use the $f/0.21$ grid to match the focal length settings for HIRAX and CHORD and to maintain consistency with the electromagnetic simulations discussed in the next chapter. Since the dish 2 data includes points representing the feed and its support structure (which are not required for this analysis), an additional pre-processing step is performed. The photogrammetry data

points for dish 2 are labeled with specific name tags such as ‘code’, ‘nugget’, and ‘target’, each with distinct meanings for this analysis. *Target points* are the critical points of interest or features located on the surface of the parabolic dish and the feed support structure. They are the primary locations where measurements are taken to assess characteristics like the dish’s shape and deformations. Target points are the central focus of the photogrammetry analysis. *Coded Targets* consists of a central circle surrounded by a distinct pattern of dots or squares. The unique pattern serves as an identifier for each specific target. Coded targets are used as reference points for the coordinate system, scale definition, and matching targets across multiple images, which helps in the 3D reconstruction process. *Coded Target Nuggets* are the individual squares surrounding the central dot within a coded target. Since the goal here is to have data points that can define the entire surface of the dish sufficiently, our approach will focus on utilizing the ‘target’ points (shown in Figure 3.8(c) and (d)) while discarding the remaining data.

But remember that the targets are uncoded and placed on both the dish surface and the feed support structure, lacking unique identifiers to distinguish the data points as one would with coded targets. Because there is no any clear demarcation between the data points on the dish surface and those on the feed support structure, they are distinguished by comparing their positions relative to the best-fit paraboloid. Specifically, data points that lie outside of this paraboloid are identified as belonging to the feed support structure, rather than the dish surface. Once the best-fit residuals ($D'_i - P_i$) are obtained, Z -score is

calculated and a threshold value of 1 is set to define the significance level for outliers. The Z score serves as a metric for quantifying the deviation of data points from the mean in terms of standard deviations, aiding in the removal of outliers data points. Data points with Z -scores exceeding the defined threshold are identified and removed as they are considered outliers and may not lie on the dish surface. Finally, the resulting cleaned data undergoes one more rotational/translational correction as outlined in Section 3.1.1 before fitting to the linearised parabolic equation and obtaining the surface RMS error as given by Equation 3.8.

3.2.2 Results and Discussion

The surface errors for photogrammetry analysis are determined in the same way as those for the laser tracker. This involves calculating the RMS of the vertical and perpendicular offsets of the data points from the model surface and the results are presented in Table 3.3. By examining the residual plots ($D'_i - P_i$) presented in Figure 3.9, it is evident that the dish maintains its structural integrity at the maximum zenith angle of $+30^\circ$ and does not exhibit significant deformation. Figure 3.10 shows the differences for dish 1 between zenith angles of 0 and 30 degrees (RMS = 0.217 mm) and for dish 2 between 0 and 30 degrees zenith angle (RMS = 0.287 mm). The residual plots in Figure 3.9 show that the dish's residual patterns remain consistent when compared against a best-fit paraboloid from zenith angle 0 to 30 degrees. Therefore, when the difference between these two zenith angles is analyzed, the residual structure cancels out, revealing a quadrupole-like pattern as seen in

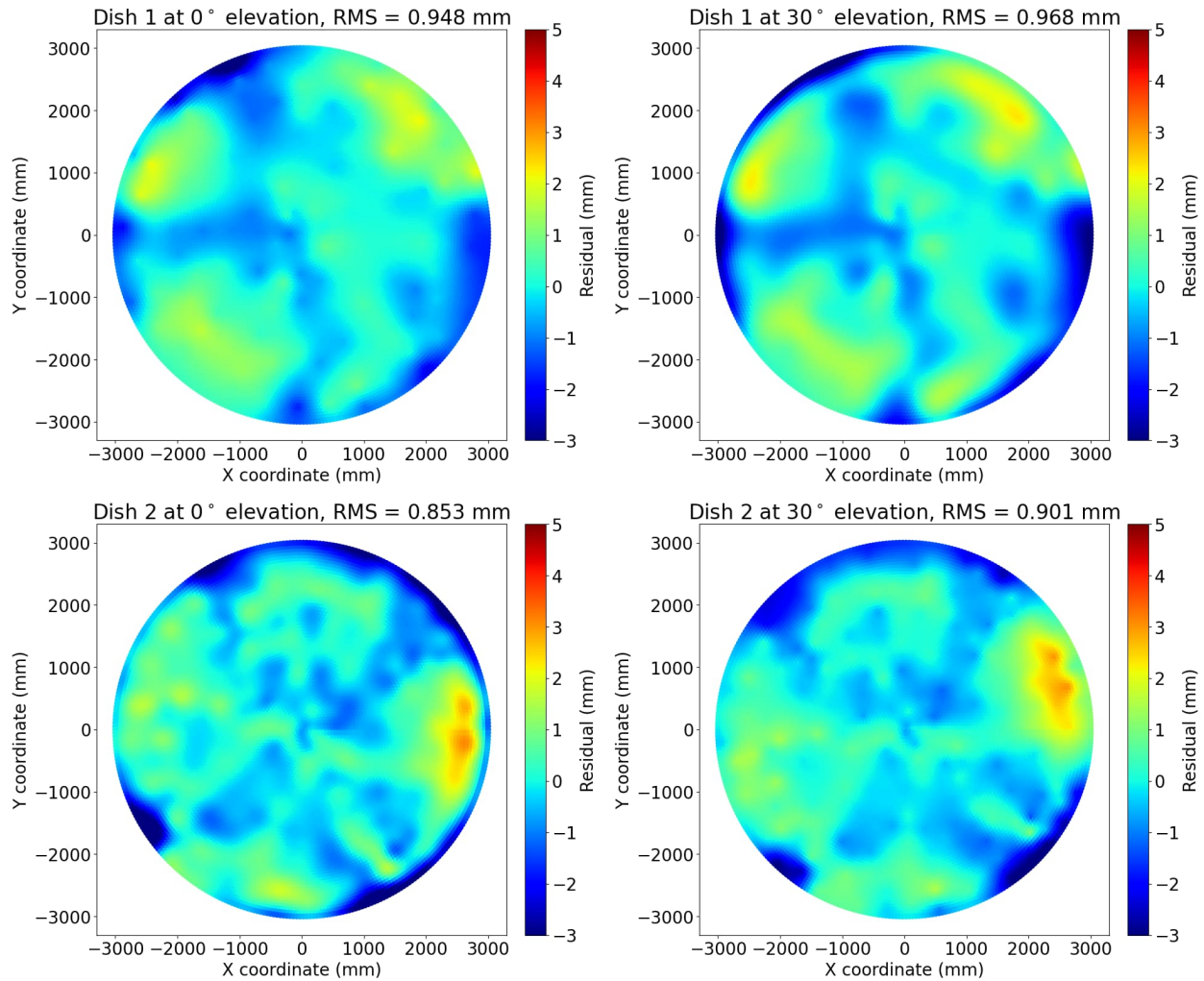


Figure 3.9: Residual plots of D3A6 dishes 1 and 2 at 0 and 30 degrees elevation angles. Here, the boresight axis of the dish is aligned with the zenith, and the vertex is positioned at the origin. The residuals are gridded onto a $f/0.21$ parabolic grid using cubic interpolation through SciPy's RBFInterpolator.

Figure 3.10, attributed to gravitational sagging which in this case refers to the deformation of a dish surface under its own weight due to gravity, particularly at off-zenith angles. In the upcoming section, we will see that similar results are obtained through finite element analysis of a D3A6 dish under various zenith angles. The direct difference between the laser tracker and photogrammetry dishes 1 and 2 at 0° zenith angle are shown in Figure 3.11. Although the vertical RMS errors of dishes 1 and 2 obtained at zenith from both laser tracker data ($\sigma_{dish1} = 0.775$ mm, $\sigma_{dish2} = 0.833$ mm) and photogrammetry data ($\sigma_{dish1} = 0.948$ mm, $\sigma_{dish2} = 0.853$ mm) are within a comparable range, the difference observed in Figure 3.11 can be attributed to several factors.

Table 3.3: Vertical and perpendicular RMS errors of photogrammetry dataset, σ_i .

Dataset	Vertical RMSE (mm)		Perpendicular RMSE (mm)		$0^\circ - 30^\circ$ (mm)
	0°	$+30^\circ$	0°	$+30^\circ$	
Dish 1	0.948	0.968	0.729	0.745	0.217
Dish 2	0.853	0.901	0.658	0.695	0.287

First, the laser tracker data set is substantially larger ($N \sim 100,000$) compared to the photogrammetry data set ($N \sim 250$). This larger dataset from the laser tracker allows for more detailed and dense surface measurements, potentially capturing more surface features that might be missed in the sparser photogrammetry data. Another contributing factor could be systematic errors from interpolation. Because both laser tracker and

photogrammetry datasets are interpolated, this process can introduce noise, especially in regions with sparse data points which could lead to discrepancies when comparing the photogrammetry results with the laser tracker data. Also, the variations in the data collection process with different backing structures and layup direction (as discussed above in Section 3.1.3) can contribute to the differences observed. Despite these differences, both methods provide valuable insights into the dish's structural behavior. The comparable RMS error values indicate that both techniques are reliable for surface characterization where the laser tracker offers high precision and density, making it ideal for detailed surface mapping, while photogrammetry provides flexibility in measuring at various elevation angles.

3.3 Effects of Radome on CHORD dishes

Within the framework of CHORD, located at DRAO, where frequent snowfall and adverse weather prevail, protecting the dishes and feed systems against environmental elements is essential to maintain operational efficiency and longevity. This section is dedicated to examining the surface distortions induced by the incorporation of a radome (a weatherproof enclosure) structure onto the D3A6 dishes, as shown in Figure 2.4, through finite element analysis (FEA). FEA is a computational technique used to predict how structures respond to environmental forces, material properties, and boundary conditions. By simulating the impact of the radome on the D3A6 dishes, we can evaluate potential

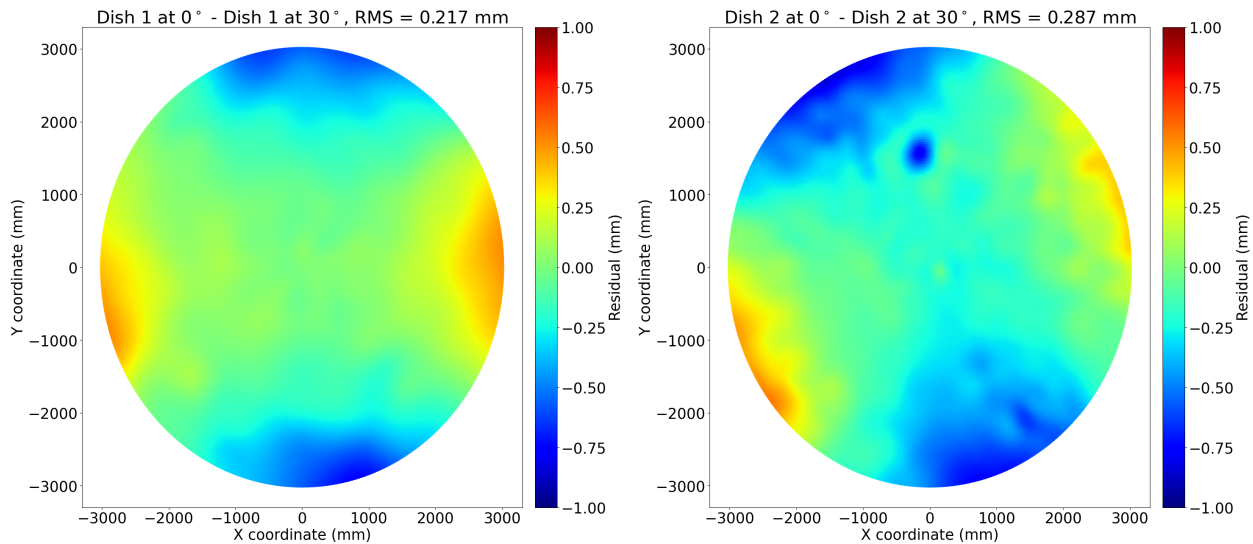


Figure 3.10: A comparison of residual plots depicting the difference between D3A6 dish 1 at 0 and 30 degrees elevation and D3A6 dish 2 at 0 and 30 degrees elevation. Before the residual calculation, azimuthal adjustments were applied to align the data at 0 and 30 degrees elevation. The residual plots are gridded onto an $f/0.21$ parabolic grid using cubic interpolation through SciPy’s RBFInterpolator for enhanced visualization.

deformations and identify design improvements to minimize any adverse effects. The FEA simulations⁴ consider the forces and stresses applied to a D3A6 dish with and without a radome structure at 0° and $\pm 30^\circ$ zenith angles⁵ under wind speeds of 0, 40, and 80 kilometers per hour (kph). For each scenario, the wind load was applied at the mount, the gravity load was accounted for, and the elevation axis was aligned along the y coordinate.

The FEA point cloud data contains (i) the x , y , and z coordinate values of each node after

⁴The FEA simulations were carried out by *Mohammad N Islam* from NRC and the deformed nodal results were provided as point cloud data.

⁵Note that zenith angles of 0° , $+30^\circ$, and -30° correspond to elevation angles of 90° , 60° , and 120° respectively. Zenith angles are measured relative to the zenith, while elevation angles are measured relative to the horizon.

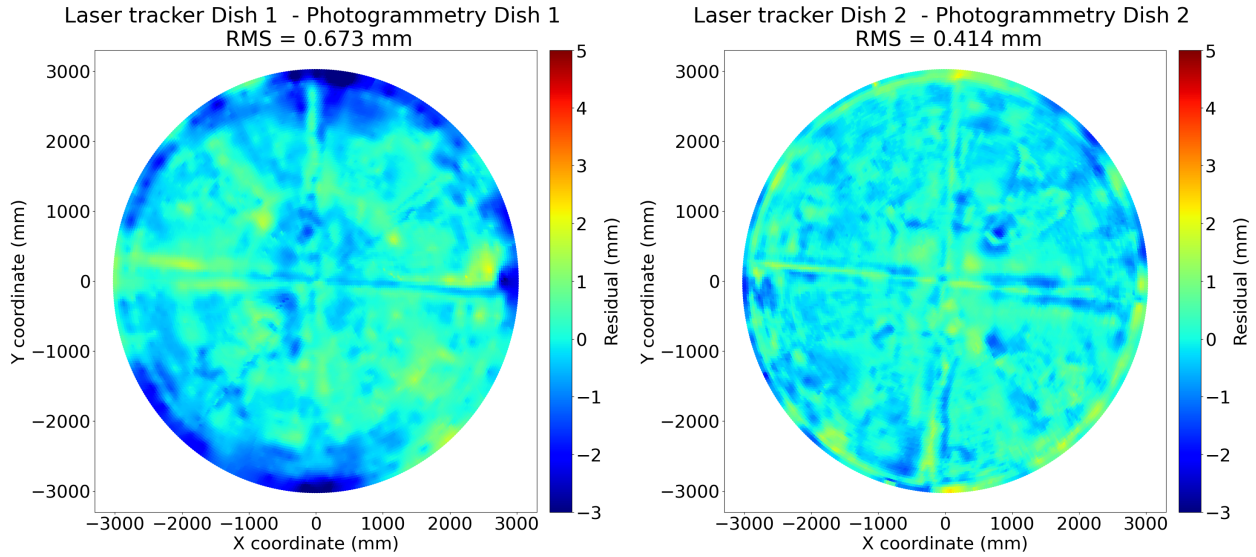


Figure 3.11: A comparison of residual plots depicting the difference between laser tracker and photogrammetry dishes 1 and 2 at 0° zenith angle. Before the residual calculation, azimuthal adjustments were applied to align both the laser tracker and photogrammetry datasets. The residual plots are gridded onto an $f/0.21$ parabolic grid using cubic interpolation through SciPy’s RBFInterpolator for enhanced visualization.

the wind and gravity loads were applied, (ii) the nodal displacement components dx , dy , and dz for each node, which can be used to determine the original positions of the nodes before the loads were applied and (iii) the magnitude of the nodal displacement at each node given by, $(dx^2 + dy^2 + dz^2)^{1/2}$. Furthermore, the FEA analysis also includes data on feed center displacement, including nodal displacement components, magnitude, and the final coordinates of displaced nodes. This information helps understand how the feed moves under different loads, offering important insights into structural responses and potential implications for overall system performance.

3.3.1 Methodology and Results

The FEA point cloud data are analyzed similarly to the laser tracker analysis procedure. First, rotational and translational corrections are applied using the minimization procedure outlined in Section 3.1.1. After these corrections, the data is fitted to a rotationally symmetric paraboloid equation using the linear least squares method. The resulting best-fit residuals are then calculated as described in Equation 3.8. The FEA surface residual plots of the D3A6 dish at 0° , $+30^\circ$ and -30° zenith angles with 0, 40, and 80 kph wind speeds are shown in Figures 3.13 - 3.15 and the surface RMS errors, σ_i for each load case are plotted in Figure 3.12(a). The FEA surface residual plots for 0 kph wind speed reveal distinct differences in RMS values with and without the radome at various elevation angles. These plots show most deformations occurring around the edges of the dish with the central area appearing relatively stable. Specifically, the ‘with radome’ cases yield lower RMS values compared to the ‘without radome’ cases at 0° zenith angle, indicating that the radome helps in stabilizing the dish surface. However, this trend does not hold at $+30^\circ$ and -30° zenith angles where the presence of the radome introduces surface deformations in the range of ± 2 around the edges. The residual structures across all wind speeds also show the Quadrupole-kind of patterns where the surface distortions are arranged in four distinct poles of alternating high and low residuals (for example, look at the surface residual plot of 0° 0 kph no radome case in Figure 3.13). These patterns are indicative of gravitational sag, where the weight of the dish causes it to deform in a predictable four-lobed pattern and

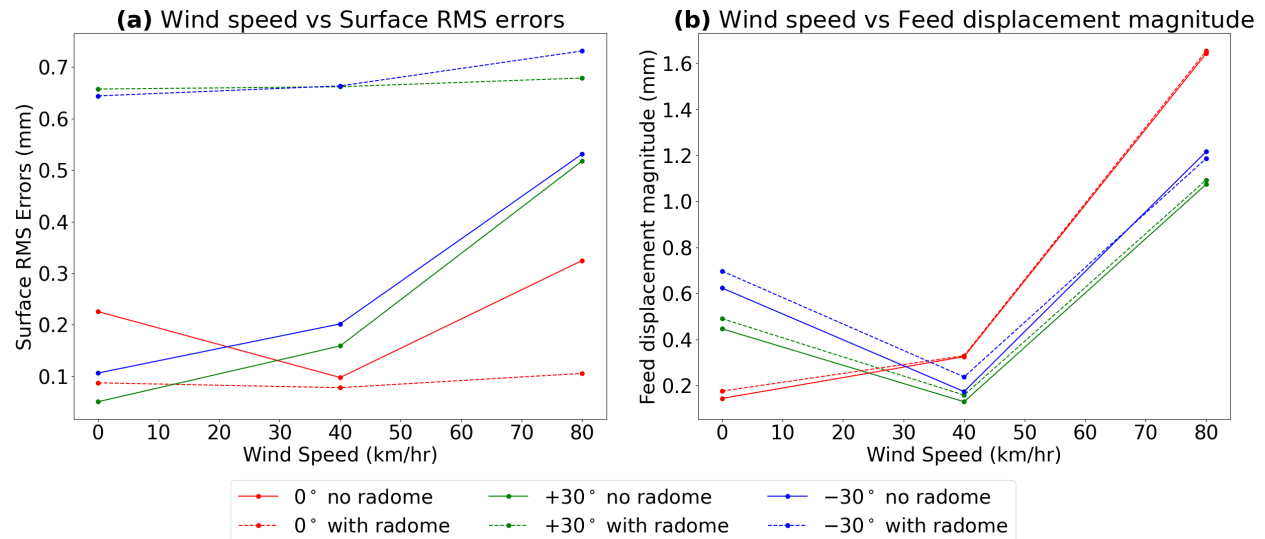


Figure 3.12: Plot (a) presents the FEA surface RMS errors calculated using Equation 3.8 for wind speeds of 0, 40, and 80 kph, both with and without the radome, at 0°, +30° and -30° zenith angles. Solid lines depict scenarios without the radome, while dashed lines represent cases with the radome. Plot (b) shows the feed displacement magnitudes obtained after applying gravity corrections for wind speeds of 0, 40, and 80 kph, both with and without the radome, at various zenith angles. Notably, displacements greater than 1 mm occur at wind speeds exceeding ~55 kph, which are relatively uncommon at DRAO.

become more evident with radome structure at off-zenith scenarios. Across each wind speed, the RMS values for ‘with radome’ cases remain within a comparable range, while those for ‘without radome’ cases exhibit significant variability. Notably, for off-zenith scenarios, the RMS values follow a similar pattern. Despite these variations, all RMS values are within the sub-millimeter range, peaking at approximately 0.7 mm for the 120° elevation at 80 kph. To accurately determine the true feed displacement values—those induced solely by the radome structure—gravity corrections (especially for $\pm 30^\circ$ zenith

angles) must be applied to the given feed displacement nodes. This process involves first calculating the original, undeformed nodal positions of the feed center based on the provided nodal displacement values (dx , dy , and dz) and performing rotational corrections similar to those used in the laser tracker analysis. The same rotational corrections obtained from the undeformed nodes are then applied to the given feed center displacement values. Figure 3.12(b) shows the magnitude of the true feed displacement for zenith and off-zenith cases across wind speeds of 0, 40, and 80 kph. It is seen that there are no significant differences between the cases with and without the radome structure. Additionally, the displacement magnitudes remain below ~ 0.75 mm for typical wind speeds at DRAO, which are below 25 kph including gusts for 80% of the time. However during the small fraction of time when the wind speeds are high (above ~ 55 kph), we see that the magnitude of feed displacement approaches more than ~ 1 mm. However, understanding the impact of feed displacements and surface deformations under normal operating conditions is more critical, with a focus on determining acceptable levels of feed shifts and surface deformations, which will be examined in detail in Chapters 4 and 5 through electromagnetic simulations.

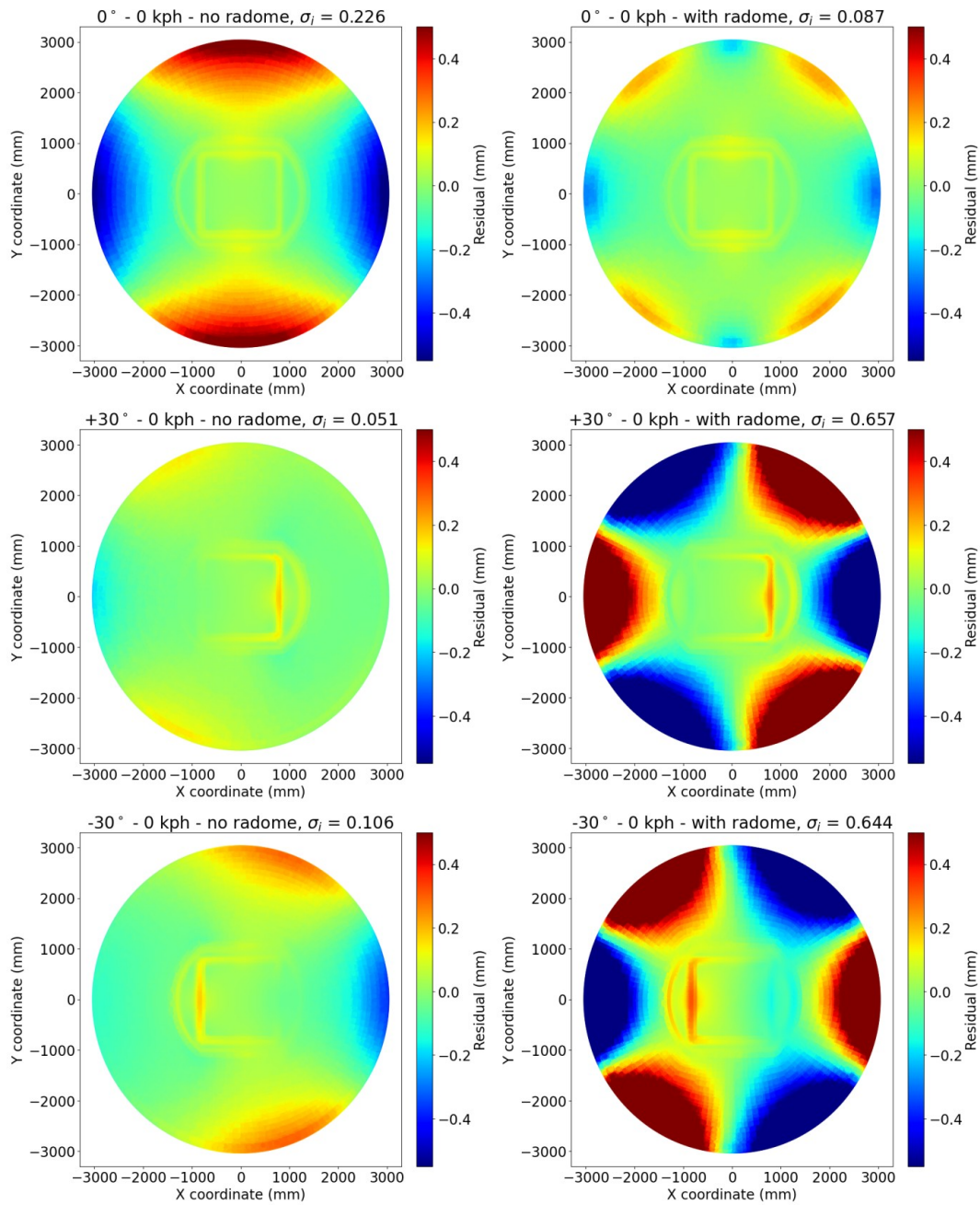


Figure 3.13: FEA residual plots of D3A6 dish for 0 kph wind speed with and without a radome structure at 0°, +30° and -30° zenith angles.

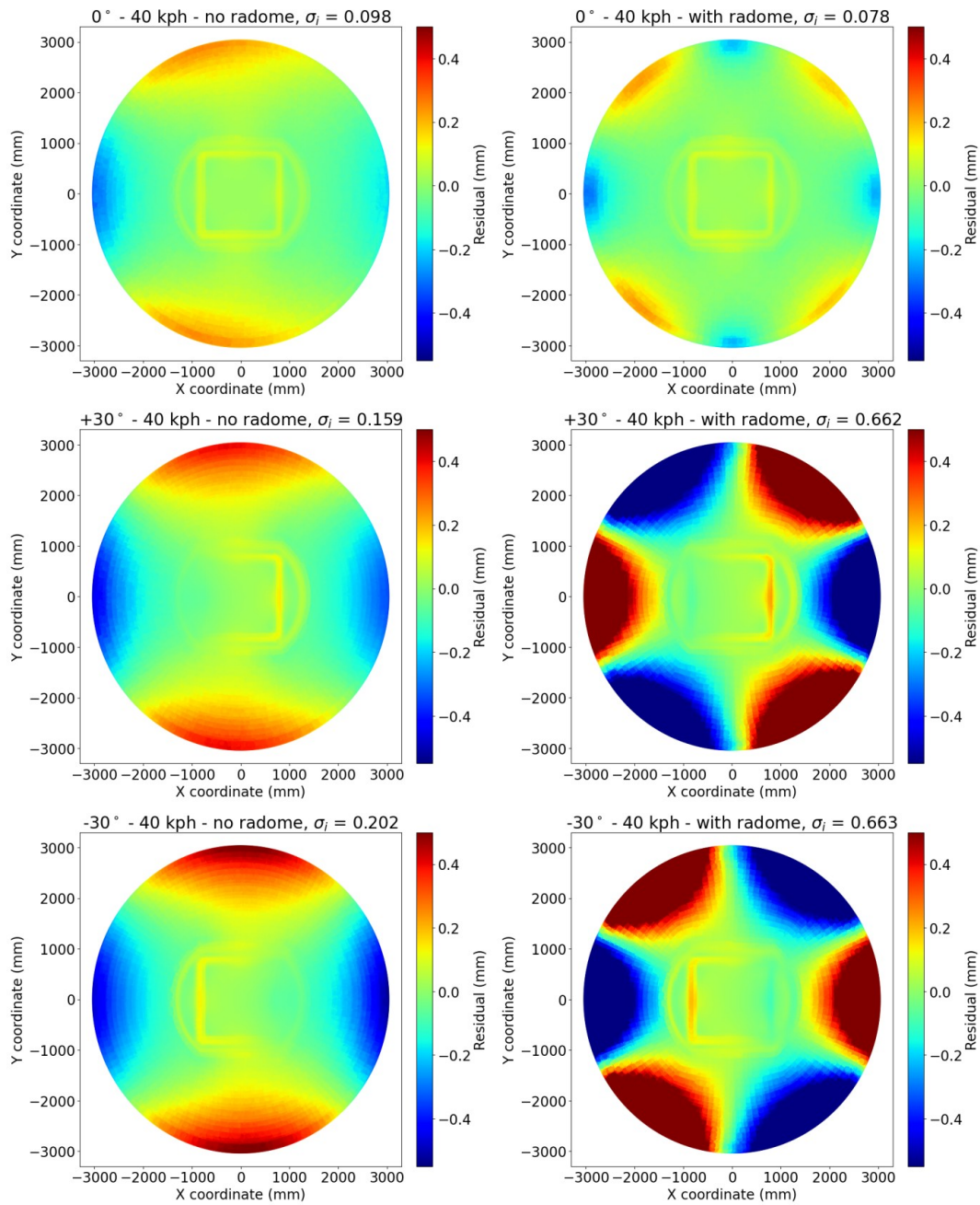


Figure 3.14: FEA residual plots of D3A6 dish for 40 kph wind speed with and without a radome structure at 0° , $+30^\circ$ and -30° zenith angles.

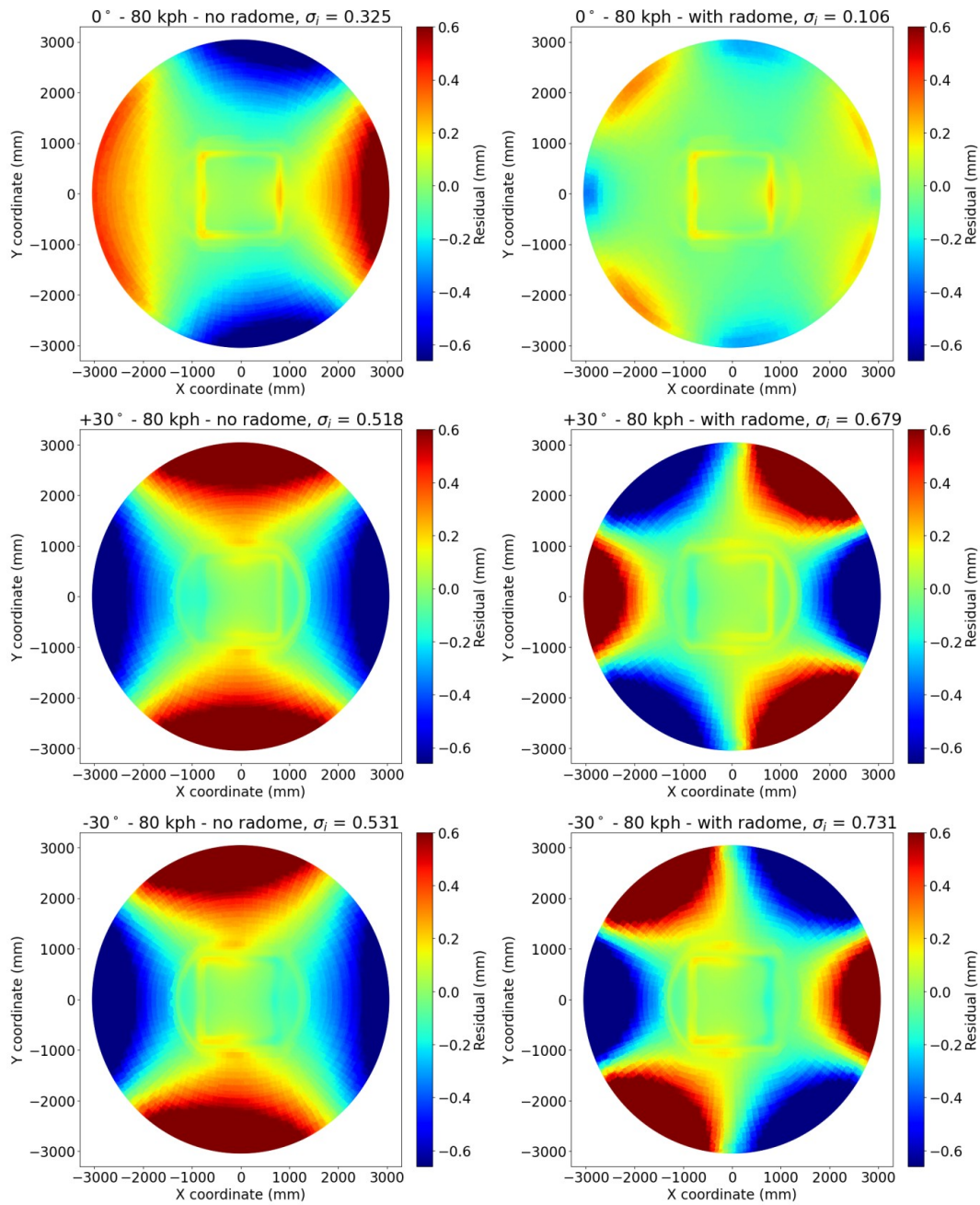


Figure 3.15: FEA residual plots of D3A6 dish for 80 kph wind speed with and without a radome structure at 0°, +30° and -30° zenith angles.

Chapter 4

Surface Deformation Effects on Beam Patterns through EM Simulations

Understanding the impact of dish surface deformations on the performance of radio telescopes requires more than just measurement; it demands integration with simulation tools to predict how these physical imperfections translate into systematic errors in scientific data. To bridge this gap, surface deformations captured through metrology are incorporated into electromagnetic (EM) simulations to investigate their effects on the beam (or radiation) pattern of radio telescopes. The farfield beam pattern of an aperture antenna is the Fourier transform of the electric field distribution illuminating the aperture and illustrates how the telescope's sensitivity changes with direction. This means that any distortions or imperfections in the dish surface will alter the electric field distribution of

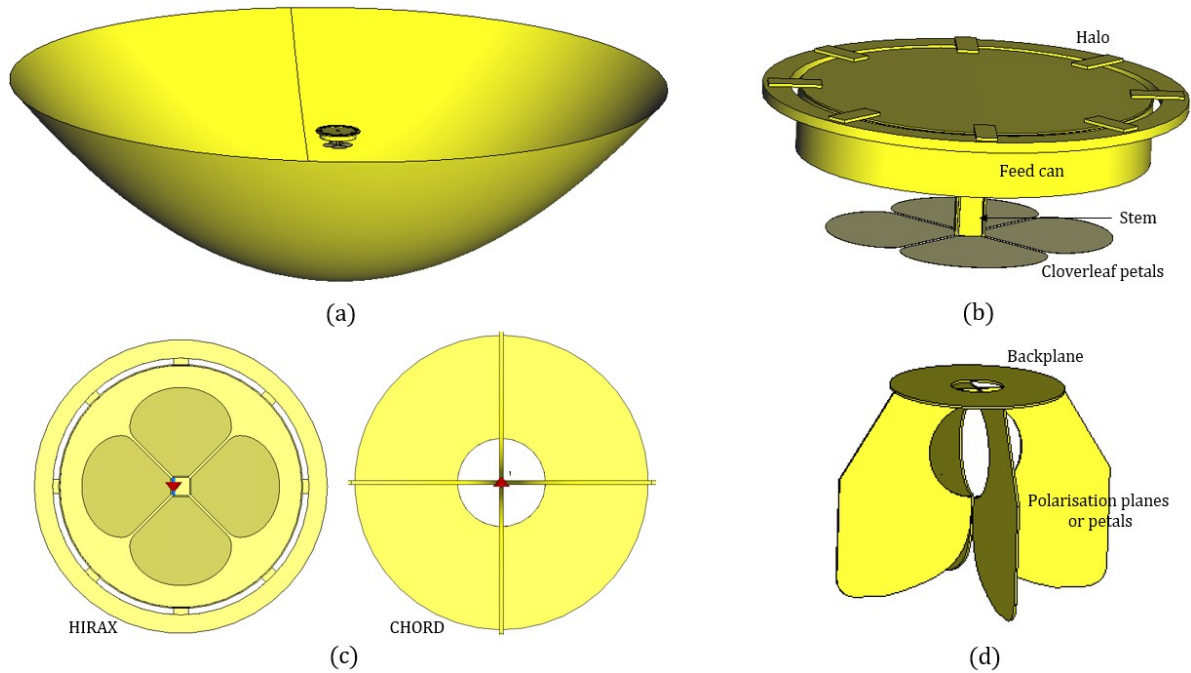


Figure 4.1: (a) The 6-m D3A6 dish characterized by a focal ratio of $f/0.21$ and paired with the HIRAX feed situated at the focus. (b) The HIRAX CAD feed, illustrating its halo, stem, feed can, and cloverleaf-shaped petal components. (c) The rear view of HIRAX and CHORD feeds, highlighting the excitation port (red arrow) defined in the y direction. (d) The CHORD CAD feed featuring its two perpendicular polarization petals and a backplane.

the aperture, thereby affecting the resulting beam pattern. To study the EM properties of these radio telescopes, CST Studio Suite, an electromagnetic and multiphysics simulation software package is utilized. All simulations presented here were conducted using the CST license server hosted by the Department of Physics at McGill University and executed on a system equipped with 128 GB RAM and AMD Ryzen Threadripper 32-core processor.

The CST CAD model¹ consists of an $f/0.21$ 6-meter parabolic dish made of aluminum

¹The CST template containing the CAD models of the dish and HIRAX feed was provided by PhD student *Kit M Gerodias*.

and the HIRAX/CHORD feed component, as shown in Figure 4.1(a). This simplified model, which includes only the dish and feed, does not accurately represent the actual setup. In reality, feed support structures and cables that power the LNA integrated within the feed obstruct parts of the aperture, leading to a decrease in aperture efficiency. Additionally, these cables can induce polarization structures in the beam, thus enhancing sidelobe levels and introducing asymmetries in the beam pattern. The reason for using this simplified model is that by focusing solely on the dish and feed, it becomes easier to isolate the effects of surface deformations without the confounding variables introduced by the support structures and cables. Furthermore, it provides ease of comparison with predictions made through metrology and reduces computational complexity, making the simulations more manageable.

The HIRAX feed CAD model includes (i) a metal structure called the *feed can*, which acts as a ground plane, aids in circularizing the beam, and reduces the beam's full-width half maximum (FWHM) to avoid over-illuminating the dish and causing spillover (Saliwanchik et al., 2021), (ii) a circular ring with 8 rectangular tabs called the *halo* which gets connected to the feed support structure and (iii) the *cloverleaf-shaped antenna* (including the stem and petal-like structure in Figure 4.1(b)) set to perfect electric conductor (PEC) material. Only a single pair of cloverleaf-shaped petals (i.e., y -polarization) is excited, using a discrete excitation port with a reference impedance of 50Ω , while no x -polarization is present in the structure. The phase center of the feed, which typically refers to the point from which electromagnetic waves radiate spherically, maintaining a uniform phase at any point on the

wavefront, is located 61.3 mm behind the front surface of the cloverleaf petal. Consequently, the base of the cloverleaf is placed 1198.7 mm above the vertex of the dish, ensuring that the phase center aligns with the focus. The simulation employs the *time domain* (or *transient*) solver, which is based on the finite integration technique and Maxwell’s equations to compute the evolution of farfield radiations over time and utilizes nine frequency channels spanning from 400 to 800 MHz, with a step size of 50 MHz. Finally, the simulation outputs the absolute electric field in decibel (dB) units and the phase values of co-polarisation and cross-polarization radiations as a function of the spherical coordinates θ and ϕ surrounding the dish.

The simplified CAD model of the CHORD feed², on the other hand, includes: (i) two perpendicular polarization planes, referred to as petals, and (ii) a circular plane at the back, known as the *backplane*, primarily used for mounting purposes (MacKay et al., 2022)—both set to aluminum material. Only one polarisation—along the y direction—is excited during the simulations using a discrete excitation port. The feed is positioned such that the backplane is located 190 mm above the focus (1260 mm from the vertex), ensuring that the phase center aligns with the focal point. The simulation settings and outputs are similar to those for the HIRAX case, except that the farfields are computed over seven frequency channels ranging from 300 to 1500 MHz, with a step size of 200 MHz. The resulting 2D beam patterns as a function of θ (ranging from 0° to 80°) and ϕ (from 0° to 360°) for the dish and

²The CAD model for the CHORD feed was provided by *Vincent MacKay*, Postdoctoral Scholar, MIT.

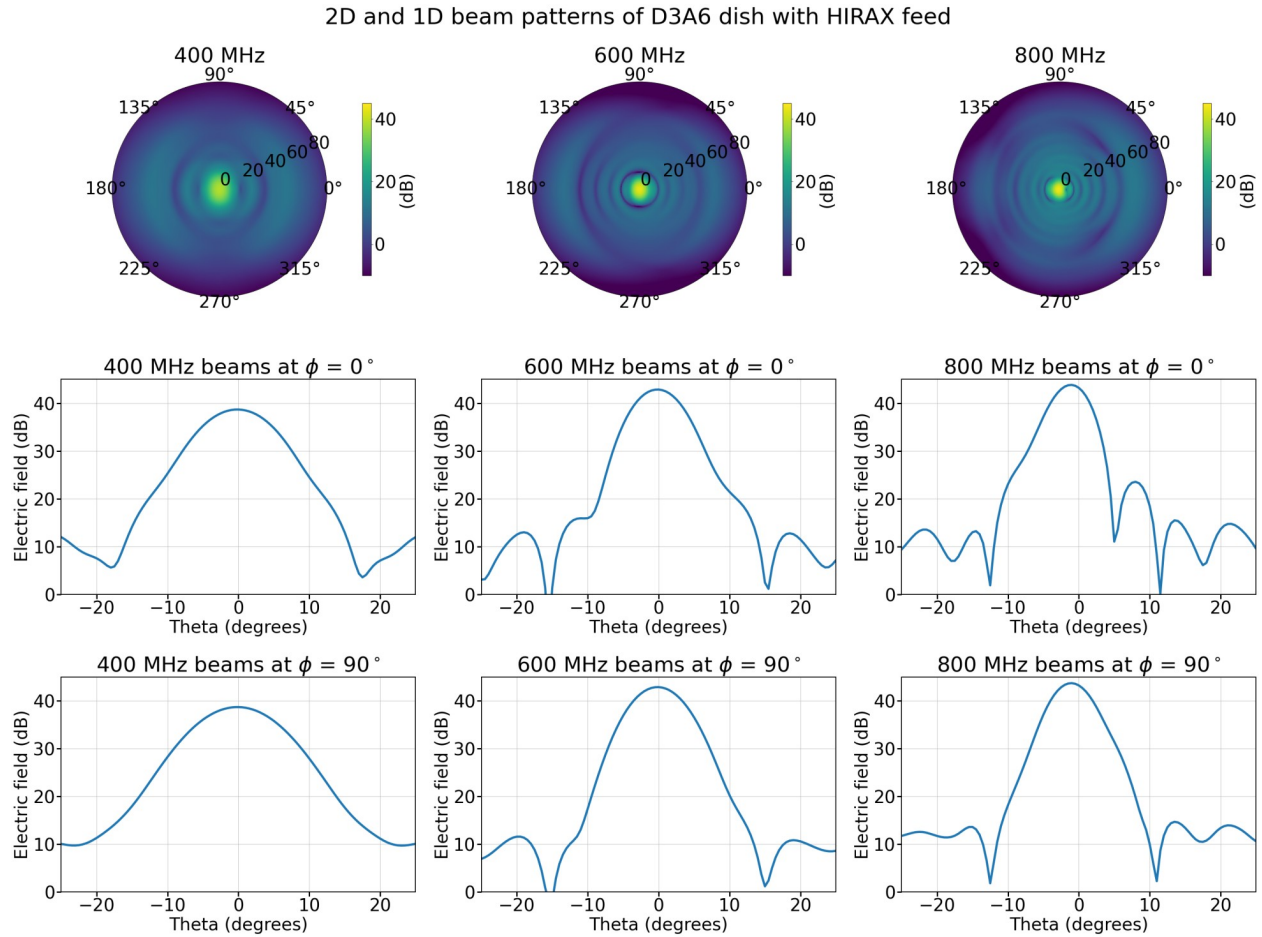


Figure 4.2: Top row: 2D polar plots showing the electric field distribution in dB (V/m) as a function of θ and ϕ at 400, 600 and 800 MHz for the dish and HIRAX feed model. Middle and bottom rows: 1D linear plots showing the electric field patterns for beams at $\phi = 0^\circ$ and 90° . The θ range is limited to -25° to $+25^\circ$ to highlight the main lobe.

HIRAX/CHORD feed models are shown in the top rows of Figures 4.2 and 4.3, respectively. Here, the color scale represents the electric field intensity in dB units. Similarly, the primary beams (1D beam cuts at $\phi = 0^\circ$ and 90°) for the dish with HIRAX/CHORD feeds are displayed in the middle and bottom rows of Figures 4.2 and 4.3, respectively. The θ range

Table 4.1: Primary beams parameters of HIRAX and CHORD fiducial models characterized by a focal ratio of 0.21.

Models	Mainlobe peak (dB)		FWHM (degrees)		SLL (dB)	
	$\phi = 0^\circ$	$\phi = 90^\circ$	$\phi = 0^\circ$	$\phi = 90^\circ$	$\phi = 0^\circ$	$\phi = 90^\circ$
HIRAX fiducial						
400 MHz	38.7	38.7	9.0	12.2	-25.8	-32.2
600 MHz	42.9	42.9	6.3	7.8	-29.9	-32.2
800 MHz	43.8	43.2	4.8	6.5	-20.3	-27.7
CHORD fiducial						
300 MHz	37.0	37.0	10.1	12.5	-17.8	-24.2
700 MHz	44.7	44.7	4.4	6.3	-19.9	-30.5
1100 MHz	47.5	47.5	2.9	3.4	-18.8	-10.8
1500 MHz	49.5	49.5	2.4	2.6	-26.4	-16.3

is limited to -25° to $+25^\circ$ to focus on the main lobe, providing a detailed comparison of the beam shape and characteristics in the most critical region of the antenna’s performance. Table 4.1 presents the main lobe’s peak value, FWHM, and sidelobe levels for both HIRAX and CHORD primary beams. The FWHM is the angular width of the beam at half its maximum power and is crucial for characterizing the antenna’s resolution and directivity. A smaller beamwidth indicates better telescope resolution and is typically approximated by the observed wavelength (λ) and the diameter of the reflector (D) as $\approx \lambda/D$. It is observed from these figures that the beams at $\phi = 90^\circ$ are wider than those at $\phi = 0^\circ$. While the centroid (the direction of the main lobe’s maximum) for the CHORD beams remains at $\theta = 0^\circ$ across

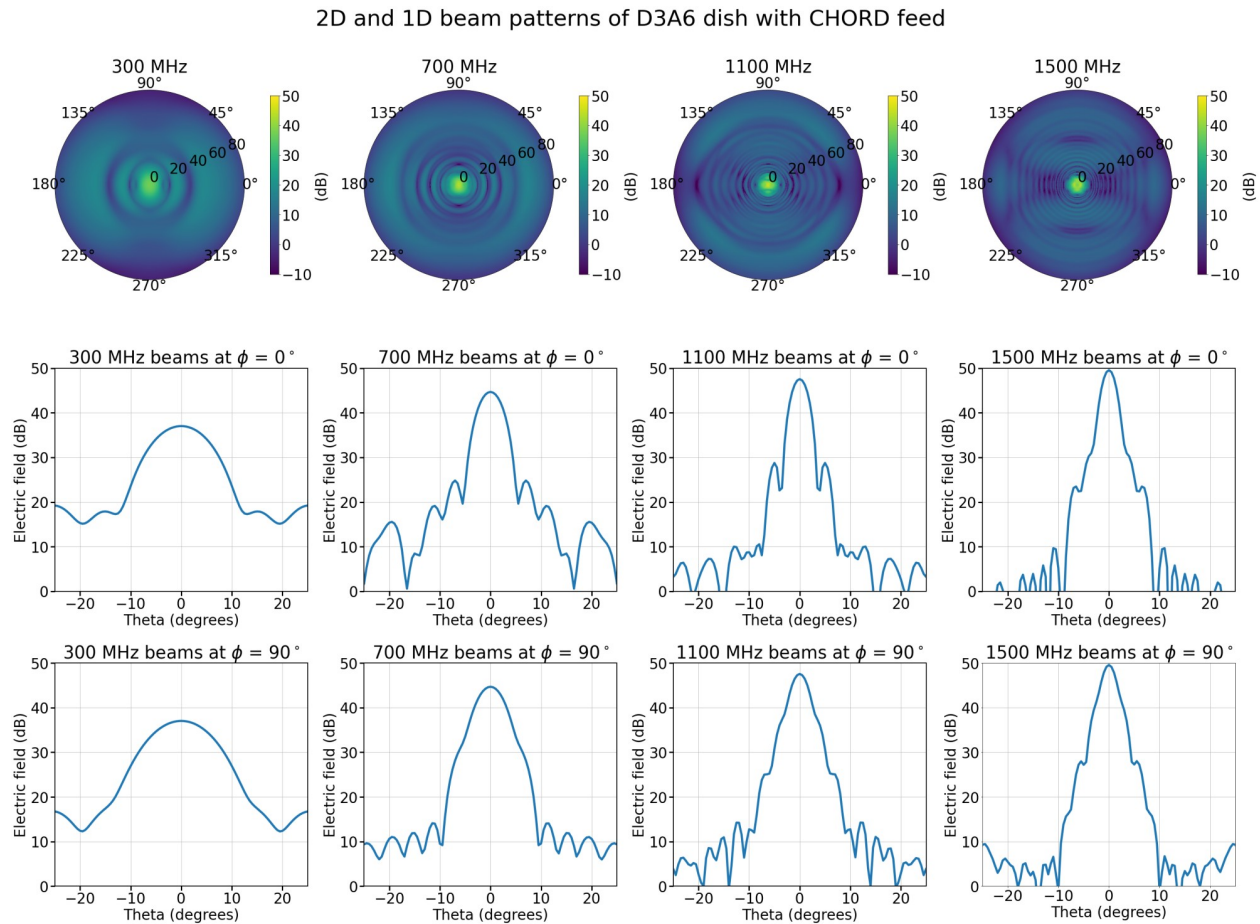


Figure 4.3: Top row: 2D polar plots showing the electric field distribution in dB (V/m) as a function of θ and ϕ at 300, 700, 1100 and 1500 MHz for the dish and CHORD feed model. Middle and bottom rows: 1D linear plots showing the electric field patterns for beams at $\phi = 0^\circ$ and 90° . The θ range is limited to -25° to $+25^\circ$ to highlight the main lobe.

its operating frequencies, the centroid of the HIRAX's primary beam shifts to $\theta \approx -1^\circ$ for frequencies above 700 MHz. The sidelobe levels (SLL) expressed in Table 4.1 indicate the relative size of the peak sidelobe in the radiation pattern of an antenna compared to the maximum level of the main lobe. For example, the SLL of -25.8 dB at 400 MHz for a HIRAX

feed model means that the maximum level of side lobes (12.9 dB) in the radiation pattern is attenuated by 25.8 dB, compared to the main beam. In contrast to the symmetry around the pointing axis ($\theta = 0^\circ$) observed in CHORD beams, HIRAX beams exhibit asymmetry, which becomes more pronounced at higher frequencies. This asymmetry is due to the current feed design, where the excitation port is positioned to the left (as shown in Figure 4.1(c)) of the antenna instead of being centered, based on practical geometrical considerations. While ongoing studies aim to address this issue, these beams currently serve as the fiducial (ideal) reference against which all simulations incorporating surface deformations are compared.

4.1 Propagating Surface Deformations to CST

The process of propagating dish surface deformations from metrology to CST involves interpolating photogrammetry or laser tracker point cloud data onto a regular grid, converting the point cloud grid into a faceted (or discretized) surface, and importing that into CST. Before delving into the complexities of deformed dish surfaces, it is essential to first focus on the undeformed, discretized models. In the simulations, the ideal or fiducial model as described above and shown in Figure 4.1(a) is parametrically defined and describes the smooth, theoretical parabolic shape of the dish. However, when dealing with a dish surface that includes deformations, it becomes impractical to define it parametrically because these deformations introduce irregularities that cannot be easily captured with simple parametric equations. Therefore, a different approach, such as using a mesh of

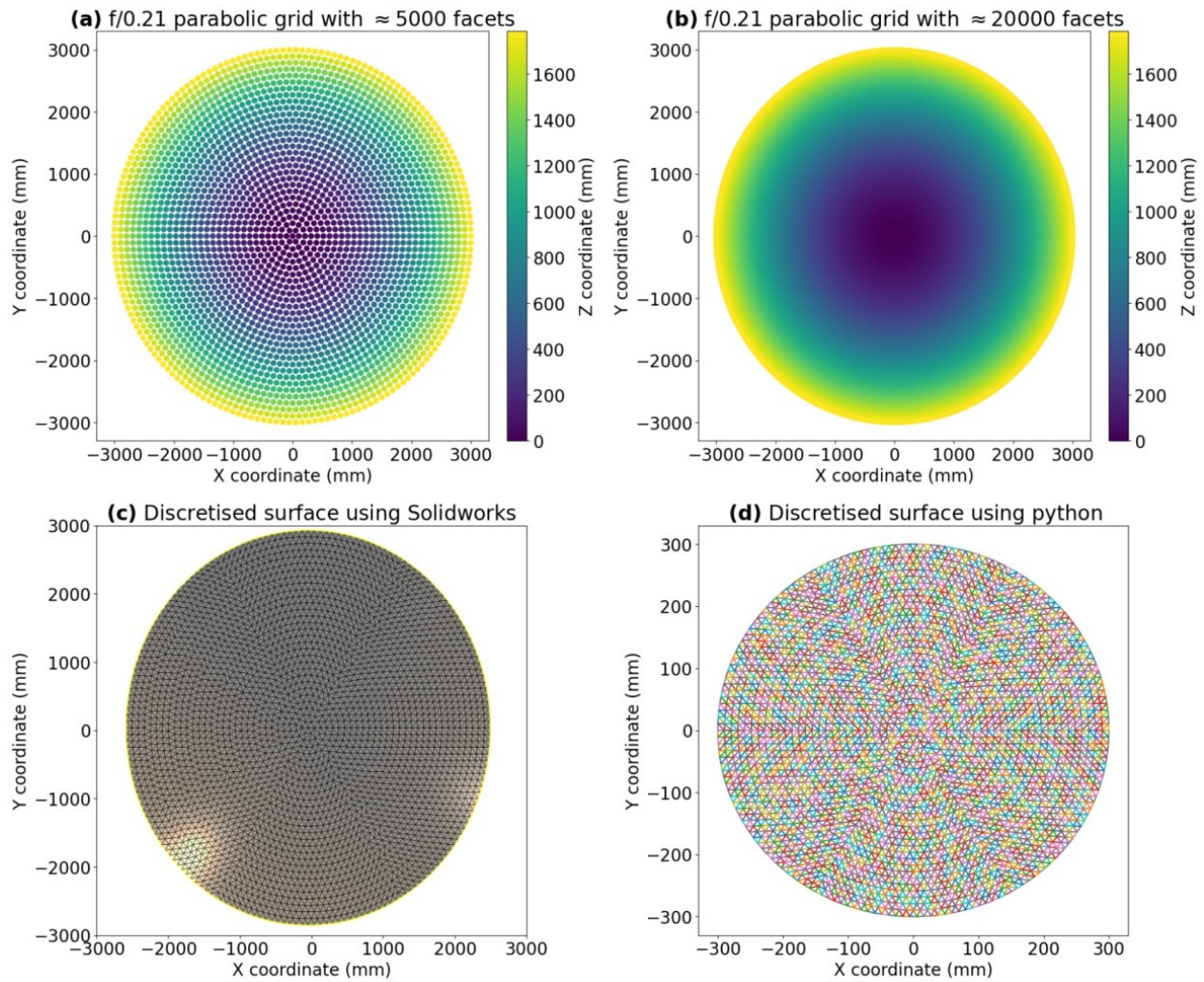


Figure 4.4: Plots (a) and (b) show a standard $f/0.21$ parabolic grid with approximately 5000 and 20000 facets, respectively. Panel (c) illustrates the discretized surface with ~ 5000 facets rendered using SolidWorks, while (d) presents the surface generated using Python's Delaunay triangulation.

discrete points, is necessary to model the perturbed surface. A detailed study on various dish surface discretization schemes is presented in the thesis by Gerodias (2023). Among them, our focus here is specifically on a discretization scheme where the dish is divided into triangular facets, with the number of facets increasing from the vertex to the edge of the dish, due to its close resemblance to the fiducial model and better performance at capturing the surface perturbations. The method for generating an undeformed, discretized regular parabolic grid³ begins by defining the number of circular rings, m , which determines the resolution of the dish surface, as illustrated in Figures 4.4(a) and (b). For each circular ring (or row), the number of points n_i is arbitrarily set to $6 \times m$, where $i = 1, 2, 3 \dots m$ represents the row index. The radial (r), and angular (θ) coordinates are then calculated as

$$r = \frac{n_{ij} \times n_i}{6m} \quad , \quad \theta = \frac{n_{ij}}{n_i} \times 2\pi, \quad (4.1)$$

where n_{ij} represents the index of points in the i^{th} row (considered as an array of ones), with $j = 0, 1, 2, \dots, n_i$. Here, r is normalized to range from 0 to 1, while θ varies linearly from 0 to 2π . These parameters represent positions from the vertex to the edge of a circular parabolic dish, serving as the basis for determining the coordinates of points on the dish. These coordinates are then converted into 3D Cartesian coordinates, where the x and y points are determined as

$$x = r \cos \theta \times R \quad , \quad y = r \sin \theta \times R. \quad (4.2)$$

³Thanks to *Jonathan Sievers* from the McGill Radio Lab for realizing this gridding scheme.

Here, $R = 3000$ mm is the radius of the dish and the z coordinate is calculated based on the parabolic equation, $(x^2 + y^2)/4f$ with f being the focal length (1260 mm). This grid, shown in Figures 4.4(a) and (b), serves as the foundation for further analysis, allowing for the incorporation of surface deformations and detailed simulations.

The regular parabolic grid is then converted into a discretized surface using two main methods: (i) SolidWorks CAD simulation software and (ii) Python's Delaunay triangulation scheme. The *ScanTo3D* functionality in SolidWorks facilitates the conversion of mesh or point cloud data into a surface or solid model. This tool allows for importing the point cloud data, which represents the grid points on the parabolic dish, and converting it into a surface model, as illustrated in Figure 4.4(c). The conversion process involves several steps, including mesh preparation where the point cloud is cleaned and filtered to eliminate any noise or irrelevant points, section and boundary curve creation, followed by trimming and knitting the surface according to the user's specifications. The resulting faceted surface can be exported to Stereolithography (STL) file format, which CST recognizes as a triangulated surface geometry of a 3D object. In Python's triangulation method, the parabolic grid data is transformed into a triangulated 3D surface through Delaunay tessellation which divides a set of points into non-overlapping triangles, ensuring no point lies within the circumcircle of any triangle. Using SciPy's Delaunay functionality, the 2D coordinates (x, y) of the parabolic grid are extracted, forming the basis for creating a Delaunay tessellation. This process generates a network of triangles covering the entire surface. Finally, the discretized

2D difference between HIRAX fiducial and discretized beams with 5000 facets rendered from SolidWorks and python

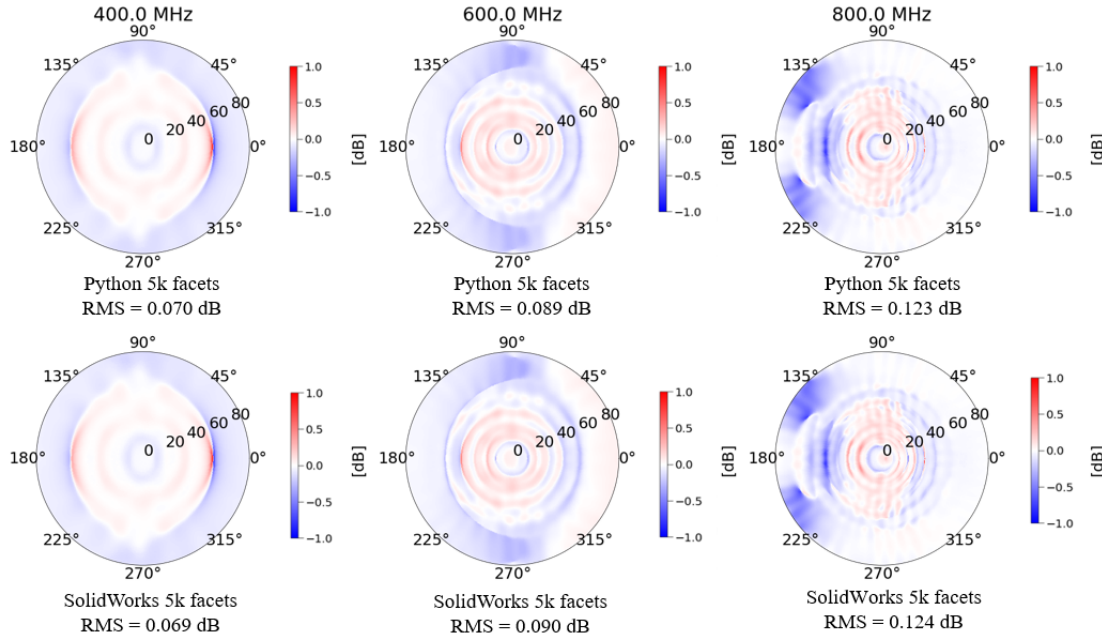


Figure 4.5: 2D polar plots depicting the difference between the fiducial and discretized surface beams for a dish and HIRAX feed model. The top row displays the results obtained using Python’s Delaunay tessellation to render the dish surface with 5000 facets, while the bottom row shows the dish surface generated from SolidWorks.

surface is exported to STL file format using the *surf2stl*⁴ python library which takes into account the parabolic grid points and the indices of the triangle vertices. To validate both approaches for rendering grid points into a discretized surface, a simulation was conducted with a dish and HIRAX feed model. Both SolidWorks and Python’s triangulation methods were employed to generate and render the dish surface using an $f/0.21$ 6-meter parabolic grid with 5000 facets. Figure 4.5 illustrates the comparison of the electric field data between

⁴surf2stl - A python package for converting 3D surface data to STL file format. For more details, refer <https://github.com/asahidari/surf2stl-python>

the fiducial and discretized model beams as a function of θ and ϕ . Here (and throughout this thesis), the residuals represent the difference in electric field data in dB units, which directly corresponds to the difference in logarithmic values and thus reflects the ratio of electric field levels between the two scenarios. It is evident from the residual structures and RMS errors that both approaches yield similar results, with beam deviations becoming more pronounced as frequency increases. At 800 MHz, the fiducial beams exhibit distorted sidelobe levels, resulting in beam deviations of approximately ± 0.5 dB. Despite the nearly identical outcomes of both approaches, Python's Delaunay method will be adopted for further simulations due to its straightforward execution within a single platform, enabling smoother workflow management.

4.2 Simulations of Deformed Dishes with HIRAX Feed

Ideally, one would expect that increasing the number of facets (grid points) would make the discretized dish model more closely resemble the smooth fiducial model. However, previous studies by [Gerodias \(2023\)](#) have demonstrated that this was not the case for the model incorporating the dish and HIRAX feed. For instance, a model with 20000 facets deviated more from the fiducial than a model with just 5000 facets. One potential explanation for this observed systematic lies in the CST mesh generator. Time domain solvers in CST typically utilize hexahedral meshes, generating them based on factors such as the structures employed and the frequency range, with provisions for setting maximum/minimum cell sizes

4. Surface Deformation Effects on Beam Patterns through EM Simulations 100

per wavelength or geometrical dimensions of the structure. Increasing the number of facets can demand a more complex mesh to represent the dish surface structure well. Ongoing studies aim to understand the interaction of CST meshes on dish surface discretization and mitigate any underlying simulation systematics. Despite encountering systematic errors associated with the dish surface discretizations, as shown in Figure 4.5 and discussed in Gerodias (2023), we will proceed with the simulations using both 5000 and 20000 facets. This decision is based on the fact that the amplitude of the surface deformations is larger than the systematic errors associated with dish surface discretization, acknowledging that some amount of systematics will be present in the results discussed in the upcoming sections.

4.2.1 Surface Deformations from Laser Tracker Analysis

To analyze how the surface deformations affect the telescope’s observation of the sky with the HIRAX feed, the residual data of dishes 1, 2, and 3 from the laser tracker analysis are integrated into the simulation models. The procedure begins by interpolating the laser tracker residuals onto the regular $f/0.21$, 6-m parabolic grid (as described in Section 4.1) with 5000 and 20000 facets respectively. Let x , y , and z denote the 3D Cartesian coordinates of the parabolic grid as shown in Figure 4.4(a) and σ represent the residuals from the laser tracker dataset interpolated onto the grid. This interpolation is carried out using SciPy’s radial basis function (RBF) interpolation, which uses a weighted sum of functions whose value varies only with the distance between the interpolant and some reference point and is

4. Surface Deformation Effects on Beam Patterns through EM Simulations 101

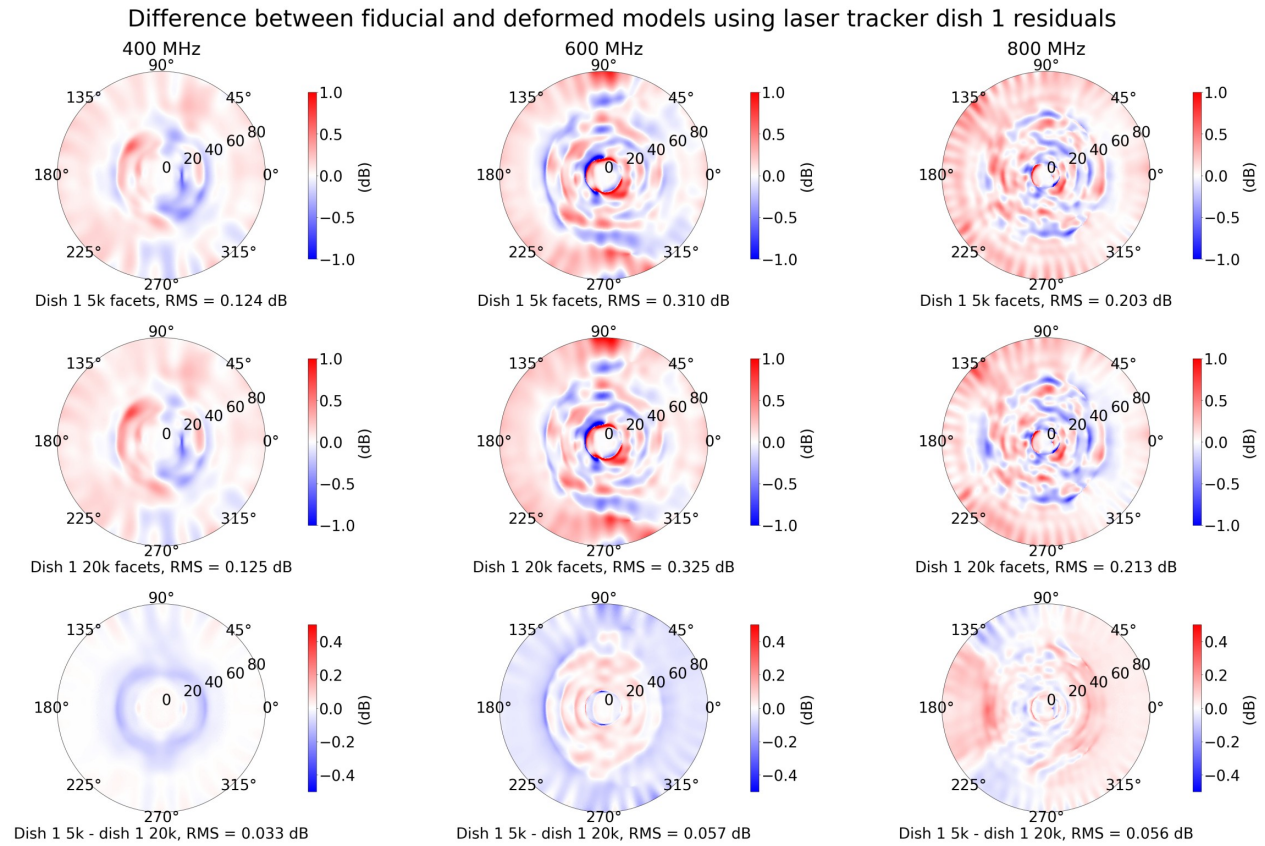


Figure 4.6: The plots illustrate the 2D beam differences between the fiducial and deformed surface models using laser tracker dish 1 residual. Additionally, the comparison between the 5000 and 20000-faceted models is shown to highlight the systematic structures of surface discretization. The beam differences from dish 1 residuals are exclusively shown here, as dishes 2 and 3 exhibit qualitatively similar results.

well-suited for scattered data in any dimension. The z -coordinates of the grid points and the interpolated residuals σ are then added together, resulting in a newly deformed parabolic grid with adjusted coordinates x , y , and $z + \sigma$ that now represent the actual geometric variations of the dish. The deformed grid is finally converted into a faceted surface using Python's Delaunay functionality, and subsequently, it is imported into CST as an STL file. The first

4. Surface Deformation Effects on Beam Patterns through EM Simulations 102

and second rows of Figure 4.6 depict the beam differences between fiducial and deformed models as a function of θ and ϕ , based on surface errors measured from laser tracker dish 1, using both 5000 and 20000-faceted models respectively. The third row illustrates the differences between the 5000 and 20000-faceted models (i.e., the first 2 rows) to visualize the systematic effects associated with discretization. The color scale represents the intensity of electric field deviations, set to ± 1 dB for the difference between fiducial and deformed surface models, and ± 0.5 dB for the difference between the 5000 and 20000-faceted models, highlighting systematic structures. Beam deviations from laser tracker dishes 2 and 3 were also analyzed, with RMS errors presented in Table 4.2, revealing qualitatively similar residual structures as depicted in Figure 4.6.

Initially, it is evident that the RMS errors for the 5000 and 20000-faceted models are within a similar range (e.g., 0.124 dB and 0.125 dB for the deformed surface based on the laser tracker dish 1 residual at 400 MHz), although the 20,000 faceted model shows a slight increase in the RMS errors in all the scenarios. Additionally, beam perturbations at 600 MHz, with RMS values around ~ 0.3 dB, are higher than those at 800 MHz, which are around ~ 0.2 dB, warranting further investigation. One potential factor could be linked to the defined location of the phase center in the simulations. Since the phase center's position can vary with frequency, previous studies conducted by HIRAX collaboration members identified it as 61.3 mm above the base of the cloverleaf antenna at the central frequency of 600 MHz, which is used across the HIRAX's operating range in the simulations. Ongoing studies aim

4. Surface Deformation Effects on Beam Patterns through EM Simulations 103

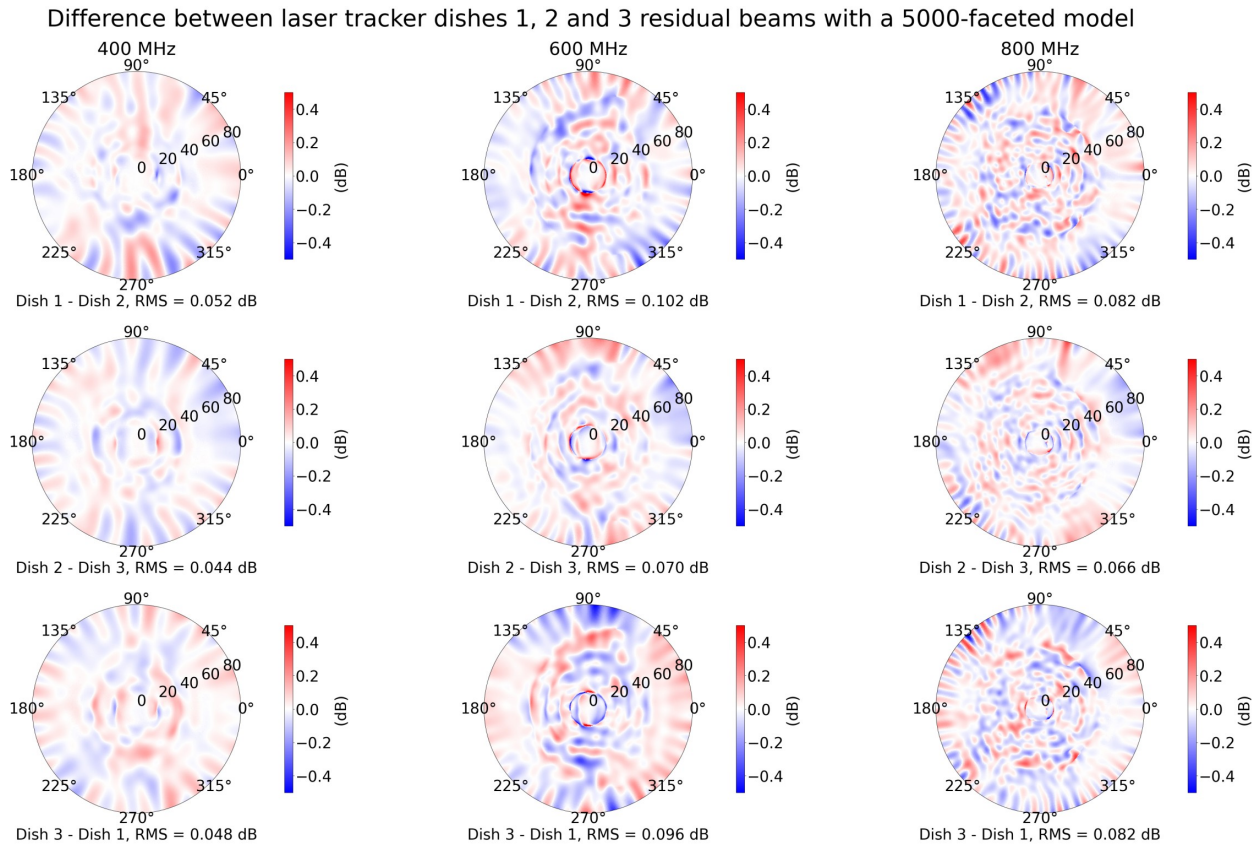


Figure 4.7: The plots illustrate the 2D beam differences among the laser tracker dishes 1, 2, and 3 for the 5000-faceted surface models. The beam differences for the 20,000-faceted models exhibit similar RMS errors and qualitative residual structures.

to validate and determine the location of the phase center for other frequencies which will help us understand the influence of the phase center on the simulation results. Similar to the increasing trend observed in the dish surface errors of laser tracker dishes 1, 2, and 3 from Chapter 3, it is intriguing to see a corresponding trend in the beam perturbations across all three dishes from Table 4.2. For instance, at 400 MHz for a 5000-faceted model, the RMS of the beam perturbations for laser tracker dishes 1, 2, and 3 are 0.124 dB, 0.126 dB, and

4. Surface Deformation Effects on Beam Patterns through EM Simulations 104

1D beam patterns of fiducial and deformed models using laser tracker dishes 1, 2 and 3 residuals

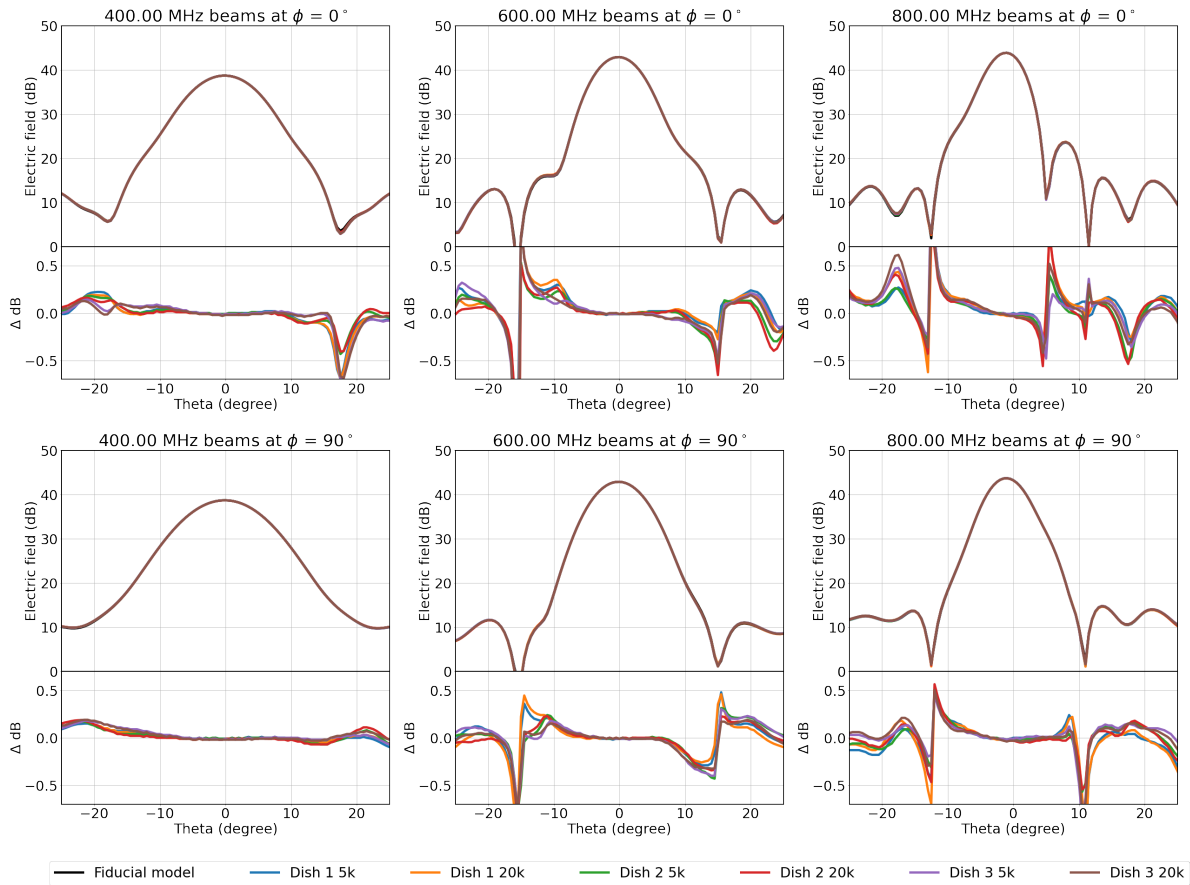


Figure 4.8: This figure presents the primary beams of the fiducial and deformed surface models using the residuals from laser tracker dishes 1, 2, and 3. The difference between the primary beams, for a polar range between -25° and $+25^\circ$, is shown as Δ dB below each plot.

0.129 dB, respectively, and at 800 MHz for a 20,000-faceted model, the beam perturbations are 0.213 dB, 0.218 dB, and 0.225 dB. The explicit differences between the beam patterns of laser tracker dishes 1, 2, and 3 with 5000 facets are shown in Figure 4.7 with the color scale set to ± 0.5 dB. Similar RMS errors and residual structures are observed in the beam differences among laser tracker dishes 1, 2, and 3 for a 20,000-faceted model. At 600 MHz, the differences

4. Surface Deformation Effects on Beam Patterns through EM Simulations 105

are observed to be higher compared to 400 and 800 MHz, with the maximum difference reaching approximately 0.1 dB between dishes 1 and 2. Consistent with metrology studies, the beam differences between dishes 2 and 3 are relatively smaller across all frequencies in comparison to other scenarios. Figure 4.8 illustrates the primary beams of the fiducial and deformed surface models, incorporating surface errors derived from laser tracker dishes 1, 2, and 3. The deformed surface model's primary beam closely follows the fiducial beam, maintaining the asymmetry and shifted-centroid behavior observed in the fiducial model, especially at higher frequencies. Beam deviations are approximately within a tenth of a dB at 400 MHz, increasing to a range of ± 2 dB at frequencies above 600 MHz. The peak of the main lobe in the deformed surface models differs from that of the fiducial by just 0.01 dB and ranges between 0.02 and 0.04 dB at 800 MHz. Despite these variations, the RMS errors remain below 0.5 dB, and the main lobe shows minimal impact, as illustrated in the Δ dB plots of Figure 4.8 with significant perturbations observed primarily in the far off-axis regions of the beam patterns.

4.2.2 Surface Deformations from Photogrammetry Analysis

Similar to the above section, the beam deviations are studied using photogrammetry residuals, allowing us to incorporate the surface errors for $+30^\circ$ zenith angle and offering a complementary perspective to the laser tracker measurements. Here, the photogrammetry residuals are interpolated onto a $f/0.21$, 6-m parabolic grid, converted into a discretized

4. Surface Deformation Effects on Beam Patterns through EM Simulations 106

Difference between fiducial and deformed models using photogrammetry dish 1 0° zenith angle residuals

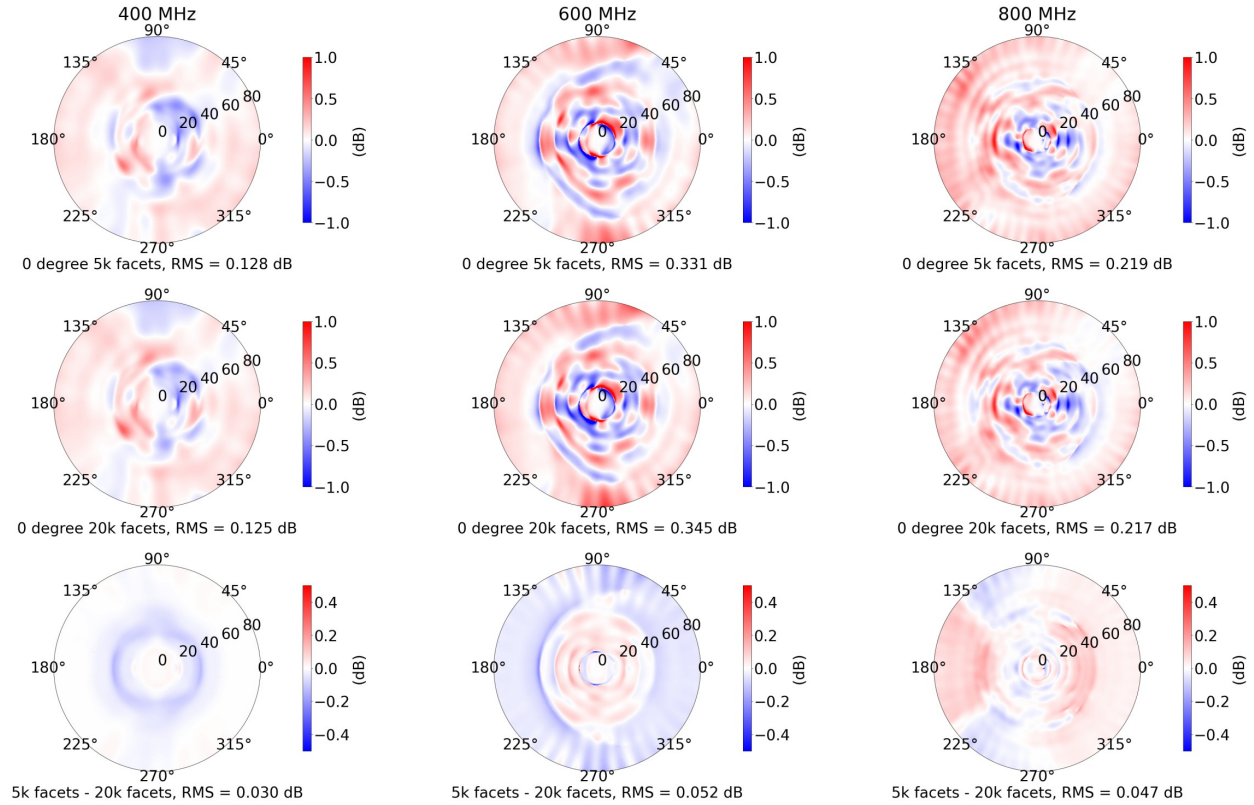


Figure 4.9: This plot shows the 2D beam difference between fiducial and deformed surface models using photogrammetry residuals from dish 1 at 0° zenith angle. The first 2 rows depict deviations from 5000 and 20000-faceted models, while the third two rows compare deviations between these two models, highlighting discretization structures. Similar residual structures are observed for dish 2 at 0° zenith angle.

surface using Python’s Delaunay triangulation, and subsequently imported into CST for analysis. The 2D polar plots depicting the beam differences between the fiducial and deformed surface models using photogrammetry dish 1 residuals at both 0° and +30° zenith angles are shown in the first and second rows of Figures 4.9 and 4.10 respectively. Additionally, the beam differences between the 5000 and 20000-faceted models at both

4. Surface Deformation Effects on Beam Patterns through EM Simulations 107

zenith angles are also presented in the third row of the figures with the color scale set to ± 0.5 dB to visualize the systematic structures of surface discretization. The residual patterns for photogrammetry dish 2 look qualitatively similar to that of dish 1 with the RMS errors for both the dishes presented in Table 4.2. Similar to the findings from the laser tracker residuals, the deviations between models with 5000 and 20000 facets are nearly identical. However, the 20000-faceted models exhibit slightly lower RMS errors at both the zenith angles, which contrasts with the trend observed with the laser tracker residuals. The beam differences at 600 MHz show higher RMS errors when compared to those at 800 MHz, as observed with the laser tracker residuals, thus reinforcing the connection between the phase center location and highlighting the need for further study. Figure 4.11 displays the beam differences between the 0° and $+30^\circ$ zenith angles for dishes 1 and 2, utilizing both 5000 and 20000-faceted models, with the color scale set to ± 0.1 dB. Both Table 4.2 and Figure 4.11 indicate that the beams of dishes 1 and 2 at these zenith angles remain nearly consistent, with maximum differences around ~ 0.04 dB. This consistency matches predictions from photogrammetry analysis, suggesting minimal dish surface deformations at maximum zenith angle. However, Figure 4.11 also shows that, compared to dish 1, dish 2 exhibits higher beam deviations between 0° and $+30^\circ$ zenith angles across all frequencies. This trend aligns with metrology data, which in Chapter 3 quantified the differences between dishes 1 and 2 at these zenith angles as 0.217 mm and 0.287 mm, respectively. Table 4.2 shows comparable beam difference results for laser

4. Surface Deformation Effects on Beam Patterns through EM Simulations 108

Difference between fiducial and deformed models using photogrammetry dish 1 30° zenith angle residuals

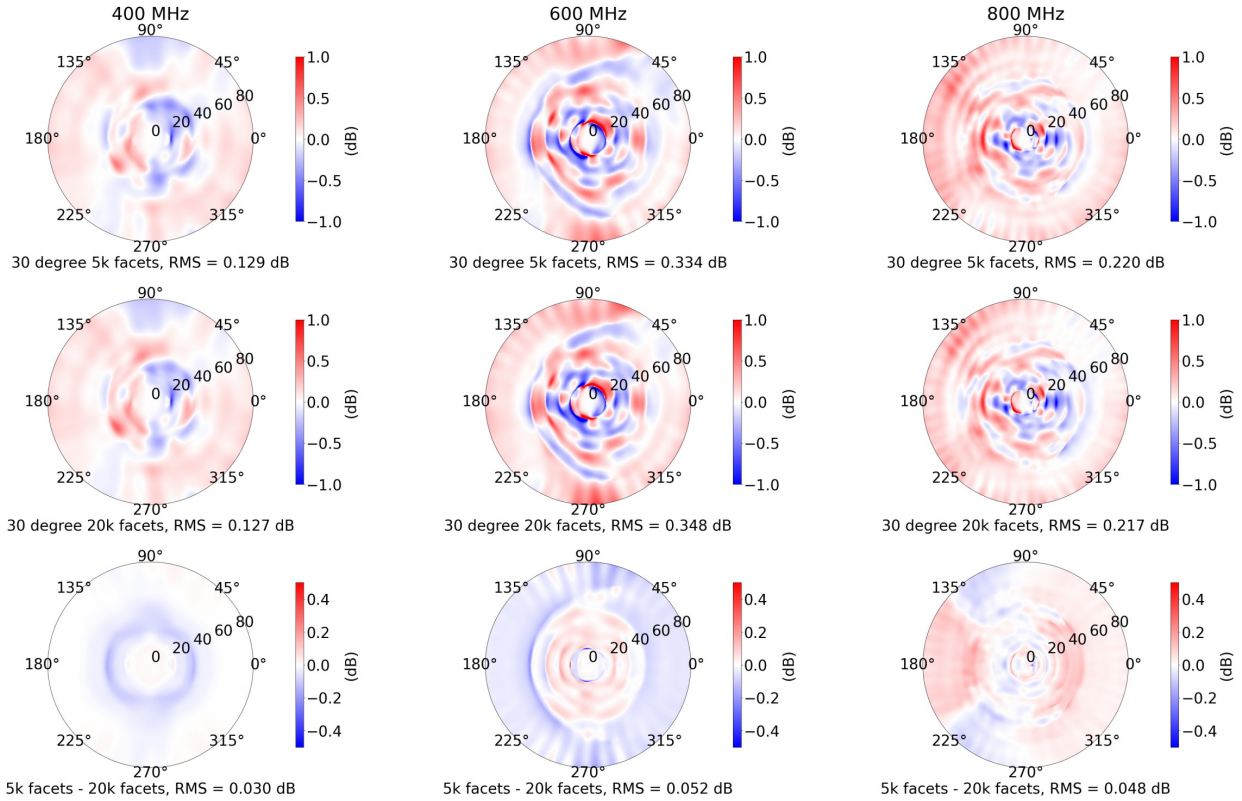


Figure 4.10: This plot shows the 2D beam difference between fiducial and deformed surface models using photogrammetry residuals from dish 1 at 30° zenith angle. The first 2 rows depict deviations from 5000 and 20000-faceted models, while the third two rows compare deviations between these two models, highlighting discretization structures. Similar residual structures are observed for dish 2 at 30° zenith angle.

tracker and photogrammetry residuals. For instance, a 5000-faceted model with laser tracker dish 1 residuals yields RMS errors of 0.124 dB, 0.310 dB, and 0.203 dB at 400, 600, and 800 MHz, respectively, while photogrammetry dish 1 residuals produce beam differences of 0.128 dB, 0.331 dB, and 0.219 dB at the same frequencies. The agreement between these independent datasets not only validates the measurement techniques but

4. Surface Deformation Effects on Beam Patterns through EM Simulations 109

Table 4.2: RMS errors in dB units for the deformed surface models with residuals from laser tracker and photogrammetry analyses at 400, 600, and 800 MHz frequencies (ν).

Surface		Laser tracker			Photogrammetry			
deformation models		Dish 1	Dish 2	Dish 3	Dish 1		Dish 2	
Resolution	ν (MHz)				0°	30°	0°	30°
~5000 facets	400	0.124	0.126	0.129	0.128	0.129	0.122	0.124
	600	0.310	0.316	0.318	0.331	0.334	0.361	0.358
	800	0.203	0.209	0.217	0.219	0.220	0.196	0.195
~20000 facets	400	0.125	0.127	0.131	0.125	0.127	0.120	0.119
	600	0.325	0.331	0.333	0.345	0.348	0.355	0.347
	800	0.213	0.218	0.225	0.217	0.217	0.189	0.189

also provides confidence in the simulation models used for predicting dish performance. This indicates that the dish fabrication methods developed at DRAO not only achieved sub-millimeter precision, as demonstrated in Chapter 3 but also successfully translated this precision into beam patterns of the telescopes. Figure 4.12 presents the primary beams of fiducial and deformed surface model for the photogrammetry dishes 1 and 2 residuals at both 0° and +30° zenith angles. The main lobe region receives very minimal impacts as inferred from the Δ dB plots whereas the major perturbations in the range ± 3 dB are found at the far off-axis pattern in the beams. Although using RMS as a metric would provide an absolute magnitude difference, not accounting for the spatial variations, it has been a convenient tool to quantify the beam difference. In the upcoming chapter, we will

4. Surface Deformation Effects on Beam Patterns through EM Simulations 110

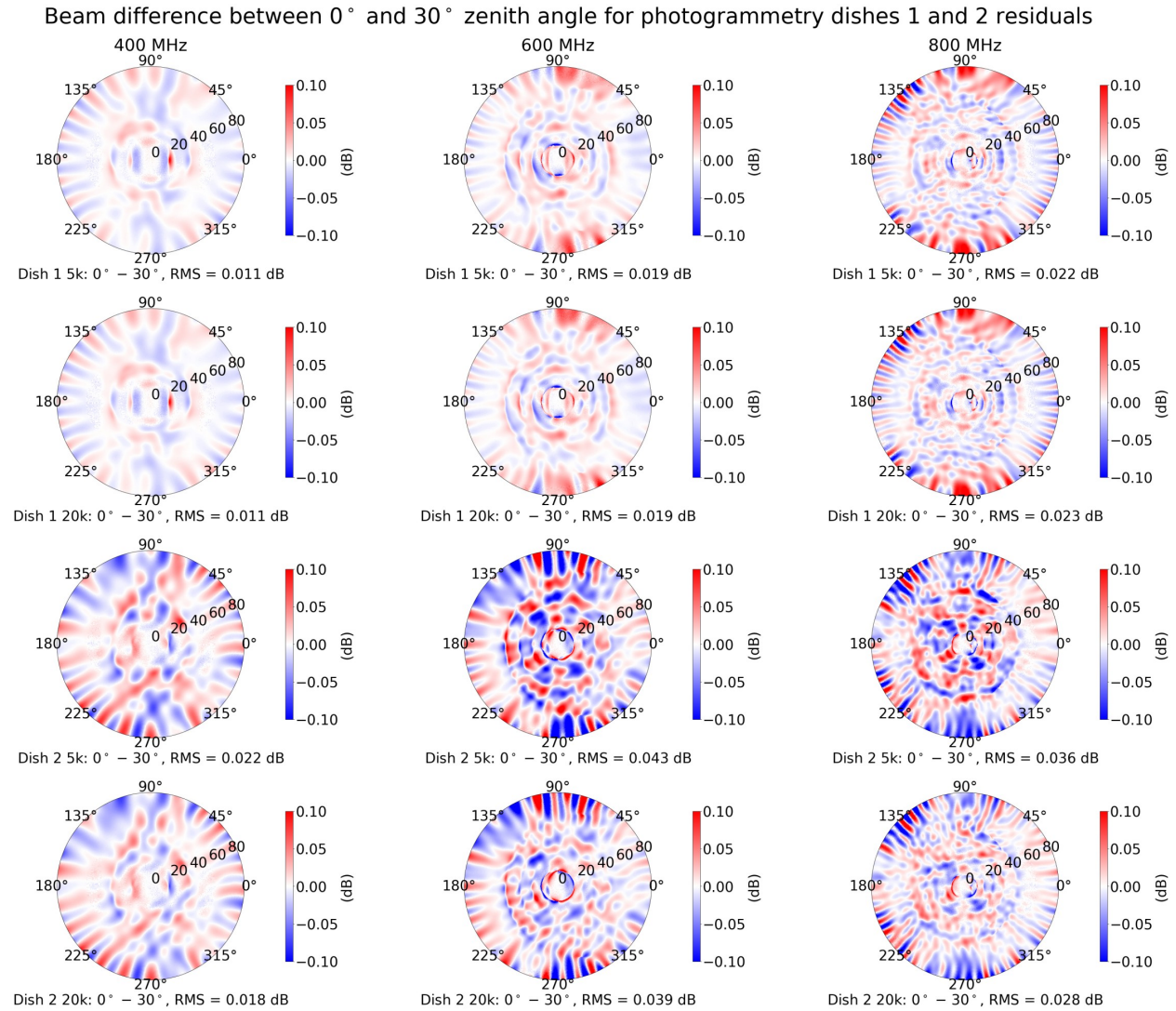


Figure 4.11: These plots show the beam difference between the 0° and $+30^\circ$ zenith angles for photogrammetry dishes 1 and 2 with both 5000 and 20000-faceted models. The color scale is set to ± 0.1 to highlight the residual structures between the beams.

introduce the beam covariance metric, which will be used to calculate beam perturbations and observe notable changes occurring within the main lobe regions.

4. Surface Deformation Effects on Beam Patterns through EM Simulations 111

1D beam patterns of fiducial and deformed models using photogrammetry dishes 1 and 2 residuals

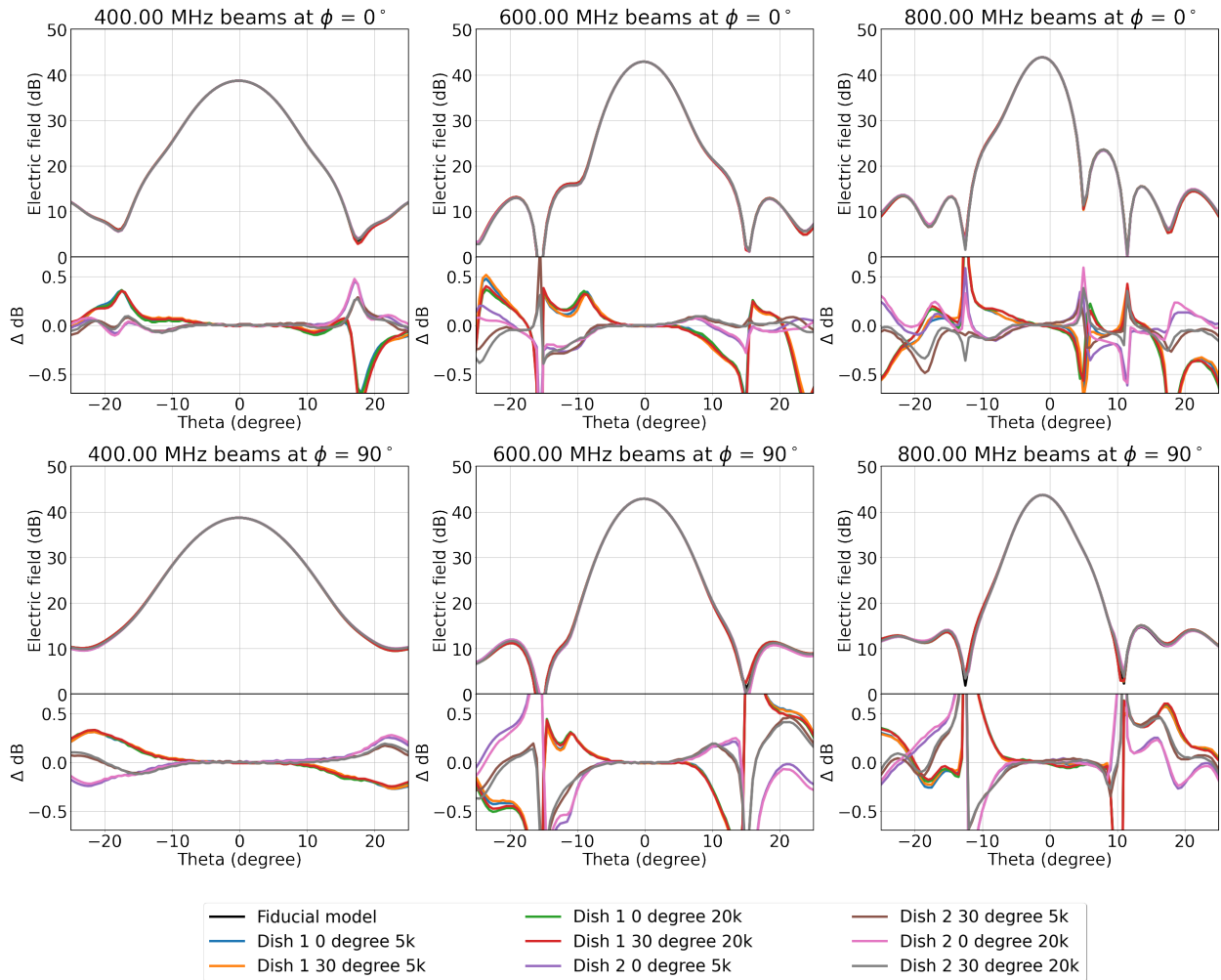


Figure 4.12: The primary beams of fiducial and deformed surface models with residuals propagated from photogrammetry dishes 1 and 2 at both 0° and $+30^\circ$ zenith angles are presented here. The difference between the primary beams, for a polar range between -25° and $+25^\circ$, is shown as ΔdB below each plot.

4.3 A Glimpse of CST Simulations with CHORD Feed

Before delving into the intricacies of deformed dishes, it is essential to first comprehend how the beams from discretized dish surface models deviate from the fiducial beams (depicted in Figure 4.3) for the dish and CHORD feed model, as intensively studied for HIRAX in Gerodias (2023). Understanding these deviations is essential for accurately modeling the performance of radio telescopes, especially when considering real-world deformations in the dish structure. The study begins by generating an $f/0.21$, 6-meter parabolic grid with 5000, 20000, and 47000 grid points, which is then rendered into a discretized surface using Python’s Delaunay tessellation method, as outlined in Section 4.1. The discretized surface is subsequently imported into CST as an STL file, and the farfield radiations are computed using the time domain solver settings. The resulting beams are then compared to the fiducial beam by calculating the direct difference between their electric field data in dB units. Figure 4.13 displays the 2D difference plot illustrating the beam deviations along with the RMS errors, while Figure 4.14 shows the primary beams (1D beam cuts at $\phi = 0^\circ$ and $\phi = 90^\circ$) for both the fiducial and discretized models. The centroid, which is the direction of the main lobe’s peak, remains at 0° for both the fiducial and discretized models across all frequencies. This consistency preserves the symmetric nature of the CHORD feed, even for the discretized models. Unlike the case with HIRAX, where increasing the resolution from 5000 to 20000 facets results in worsened beam deviations, here, the model with 20,000 facets closely approximates the fiducial beams. However, further discretizing

4. Surface Deformation Effects on Beam Patterns through EM Simulations 113

the dish surface into 47,000 facets increases beam deviations, suggesting that higher facet counts do not necessarily improve beam accuracy beyond a certain point. Although the 20,000 facet model offers a close resemblance to the fiducial, with a maximum RMS error of 0.09 dB at 1500 MHz, it is important to validate this result further. Current efforts involve conducting simulations using CST integral solvers, which enable the use of a farfield source excitation instead of the physical feed structure. This approach decouples the dish from the feed, thereby avoiding any dish-feed interaction and allowing a focused analysis of the influence of dish surface discretization.

Similarly, examining the primary beams of the discretized models in Figure 4.14, it is inferred that for frequencies below 700 MHz, the beam deviations are relatively small, around a tenth of a dB. However, as the frequency increases beyond 700 MHz, the deviations become more pronounced, reaching ± 3 dB for a 5000 facet model at 1500 MHz. The peak of the main lobe in the deformed surface models deviates from the fiducial beam by a maximum of 0.1 dB for the 47,000-facet model at 1500 MHz, while at lower frequencies, the deviations range between 0.01 and 0.02 dB across all the discretized models. This first set of CST simulations with the CHORD feed provides a foundation for future simulations that will incorporate surface errors from laser tracker and photogrammetry metrology, as performed for the HIRAX feed.

4. Surface Deformation Effects on Beam Patterns through EM Simulations 114

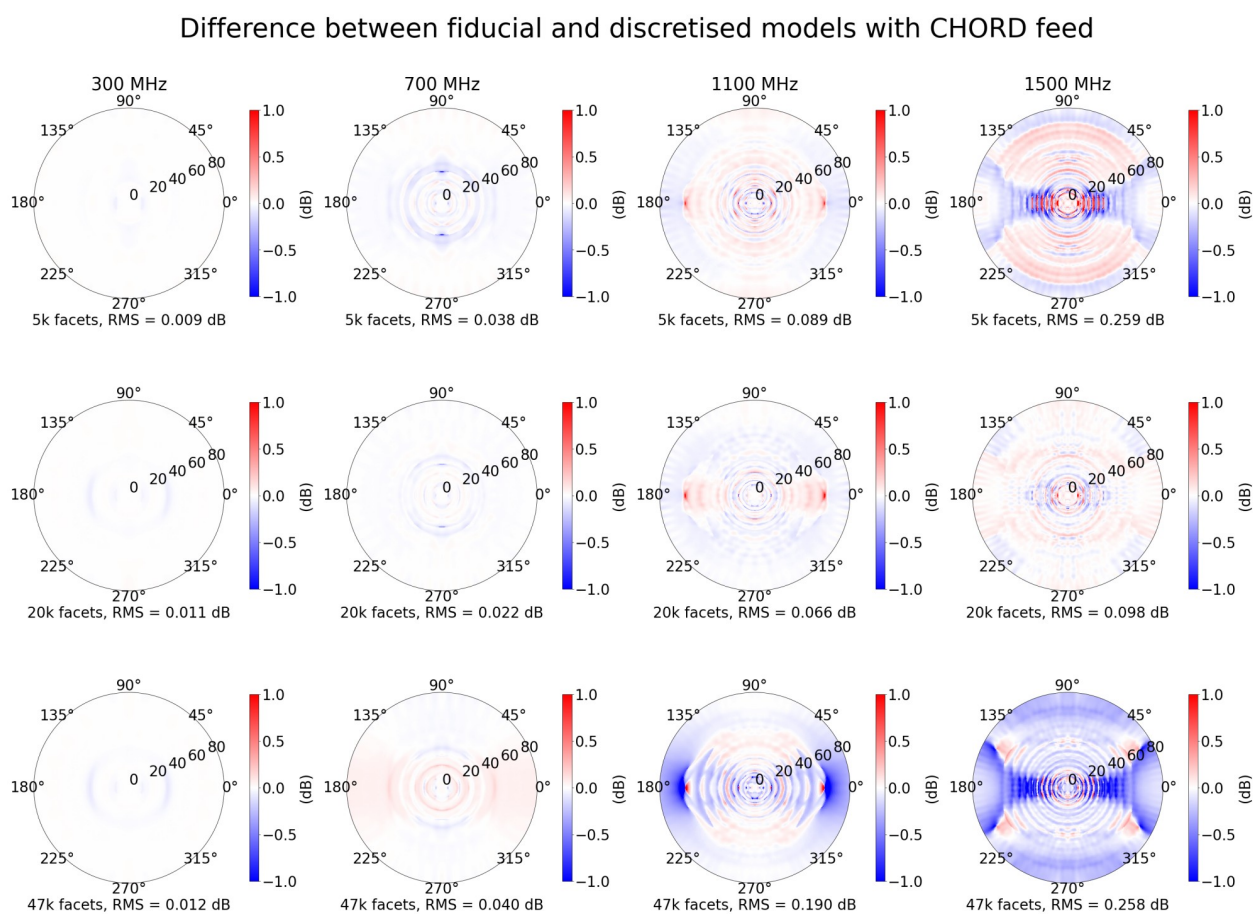


Figure 4.13: These 2D polar plots illustrate the differences between the beams from the fiducial and discretized surface models for the CHORD feed. The four columns correspond to frequencies of 300, 700, 1100, and 1500 MHz, respectively, while the three rows represent the levels of discretization resolution: 5000, 20000, and 47000 facets. In contrast to HIRAX, the beam deviations show improvement as the number of facets increases from 5000 to 20000, but degrade upon further increasing to 47000 facets.

4. Surface Deformation Effects on Beam Patterns through EM Simulations 115

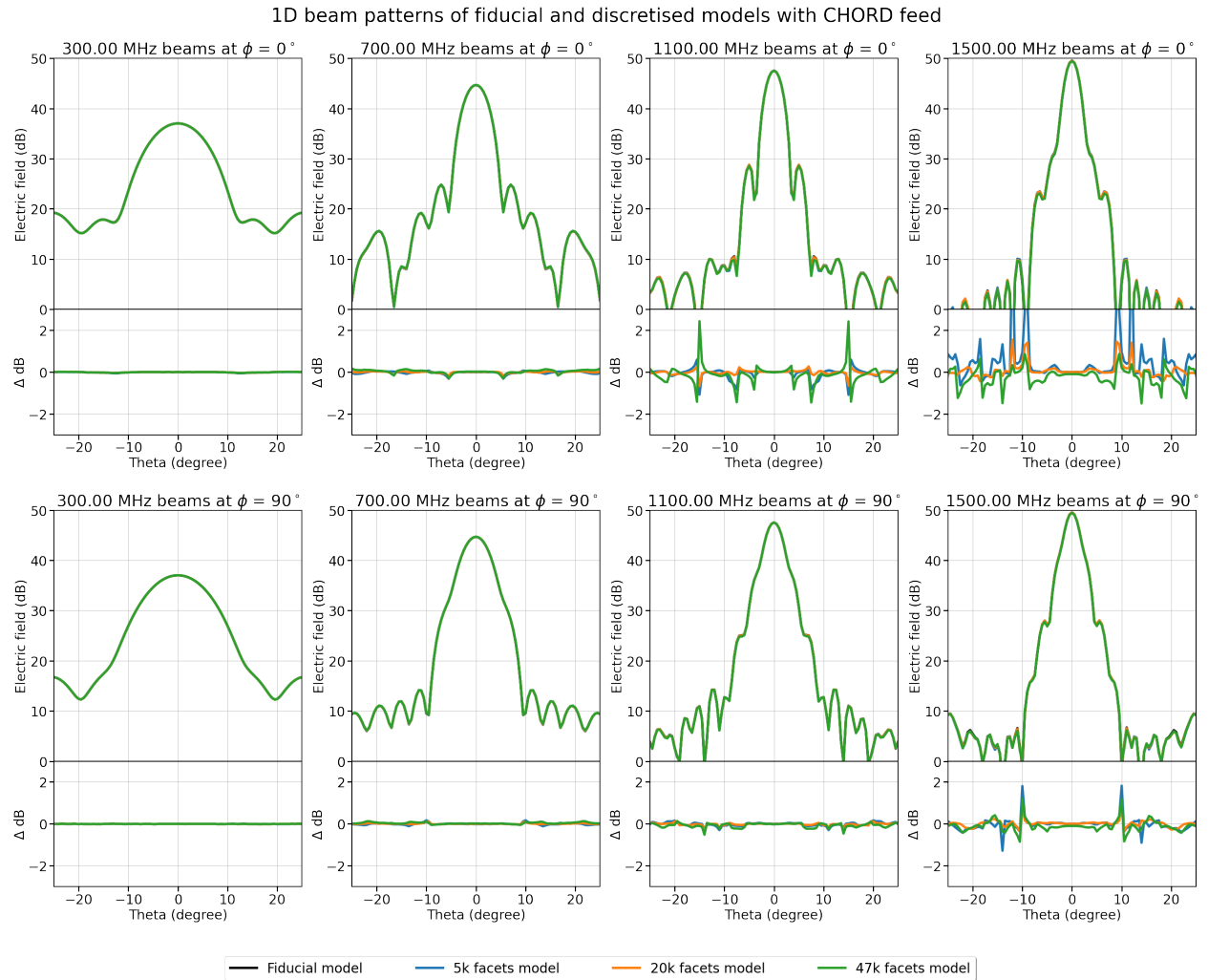


Figure 4.14: The 1D beam cuts at $\phi = 0^\circ$ and $\phi = 90^\circ$ for both the fiducial and discretized models using the CHORD feed are presented in this figure. These plots also include the error, ΔdB , which signifies the difference between the electric field data of the fiducial and discretized models.

Chapter 5

Beam Covariance

5.1 A Metric to Quantify the Beam Differences

In Chapter 4, the comparison between the fiducial and deformed beams was evaluated using a metric based on the RMS of their direct subtraction. However, relying solely on RMS has its limitations, as it only considers the absolute magnitude of differences between datasets and reduces the variation across the beam to a single value, ignoring their spatial distribution. To address this, beam covariances are introduced as a more comprehensive metric. Beam covariances provide valuable insights into the spatial relationships between different points in the antenna's radiation pattern. This chapter outlines the procedure for computing beam covariances and demonstrates their utility in quantifying beam deviations across various simulations involving perturbed dish models, such as offsetting the feed position/orientation

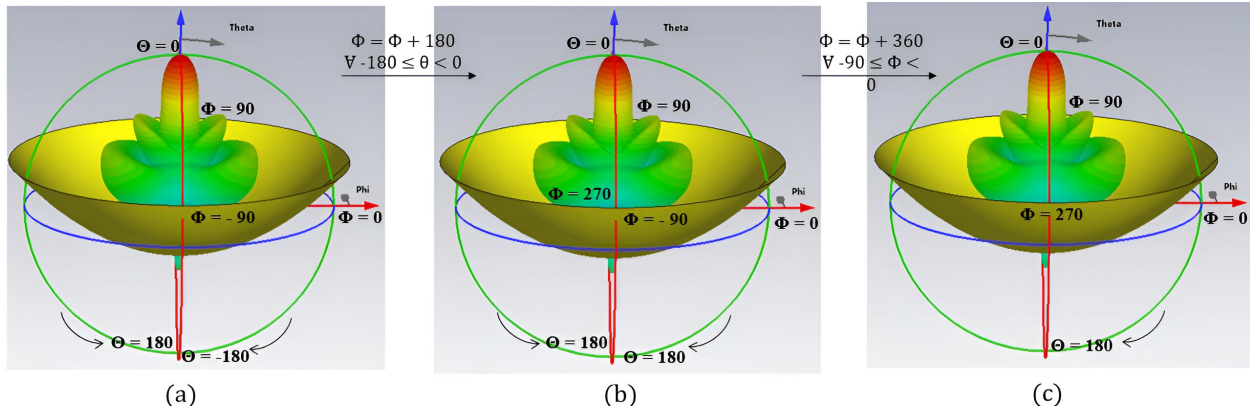


Figure 5.1: (a) A glimpse of the coordinate system (θ, ϕ) surrounding the dish along with its radiation pattern at 400 MHz. The ϕ coordinate spans from -90° to $+90^\circ$, while for each ϕ value, the θ angles are defined from -180° to $+180^\circ$. (b) For all angles θ within the range of -180° to 0° , their corresponding ϕ values are modified by adding 180° . (c) All angles ϕ in the range from -90° to 0° are adjusted by adding 360° .

and incorporating discretization/deformation effects. Before delving into the calculations, it is important to understand how CST Studio Suite outputs the desired results. The electric field (E) is presented in units of decibels (dB) as a function of two spherical coordinates, θ and ϕ (in degrees), surrounding the dish. The ϕ coordinate spans from -90° to $+90^\circ$, while for each ϕ value, the θ angles are defined from -180° to $+180^\circ$ as shown in Figure 5.1(a). To obtain the electric field data for the complete angular coverage of $0^\circ \leq \theta \leq 180^\circ$ and $0^\circ \leq \phi \leq 360^\circ$ (i.e. transforming the coordinate system presented by CST into something usual that is easy to implement in further calculations), the following manipulations are carried out:

1. The θ values initially defined from -180° to 0° for each ϕ are equivalent to the θ values

defined from 0° to 180° at their respective $\phi + 180^\circ$ angle as shown in Figure 5.1(b). This adjustment results in ϕ being defined in two sets: (i) -90° to $+90^\circ$ and (ii) 90° to 270° , with each having their θ definitions spanning from 0° to 180° .

2. Similarly, the ϕ values initially defined from -90° to 0° are equivalent to values from 270° to 360° by simply adding 360° to each ϕ as shown in Figure 5.1(c). As a result, we obtain an electric field pattern defined as $0^\circ \leq \theta \leq 180^\circ$ and $0^\circ \leq \phi \leq 360^\circ$, which is suitable for subsequent calculations.

5.2 Mathematical Framework of Beam Covariance

Let us derive the mathematical framework for beam covariance by first understanding the antenna's beam solid angle, denoted as Ω_A and represented as

$$\Omega_A = \int_0^\pi \int_0^{2\pi} P(\theta, \phi)_{\text{norm}} d\Omega. \quad (5.1)$$

Here, $d\Omega = \sin\theta d\theta d\phi$ is the differential solid angle in spherical coordinates, and $P(\theta, \phi)_{\text{norm}}$ is the normalized power received by the antenna as a function of θ and ϕ in dB and is given as

$$P(\theta, \phi)_{\text{norm}} = \frac{P(\theta, \phi)}{\max(P(\theta, \phi))}. \quad (5.2)$$

Equation 5.1 describes the process of assigning weights to the angular coordinates

surrounding the antenna based on its power pattern. Notably, the main lobe coordinates are given greater weight due to the higher beam amplitude in that region, while the side lobe coordinates are assigned proportionally less weight, reflecting their smaller contributions to the overall radiation pattern. Thus, using this concept we can quantify the beam differences in a way that down-weights the edges and emphasizes changes within the main lobe regions. It is important to recognize that the magnitude of the electric field pattern, $|E|$, and power pattern, P are the same when expressed in units of dB, as given by

$$P(\theta, \phi)_{dB} = 10 \times \log_{10} P(\theta, \phi) = 10 \times \log_{10} |E(\theta, \phi)|^2 = 20 \times \log_{10} |E(\theta, \phi)| = |E(\theta, \phi)|_{dB}. \quad (5.3)$$

So, one can convert the power (electric field data given by the CST) from dB to watts using the equation

$$P(\theta, \phi)_{\text{watts}} = 10^{\left(\frac{P(\theta, \phi)_{dB}}{10}\right)}, \quad (5.4)$$

and plug the normalized version of $P(\theta, \phi)_{\text{watts}}$ into Equation 5.1. Beam covariance is a valuable metric for evaluating the spatial variations between the beams of antennas. Let $P_1(\theta, \phi)$ and $P_2(\theta, \phi)$ denote the normalized power pattern of any two beams. Utilizing the concept of beam solid angle, which characterizes the spatial coverage of individual antennas as discussed above, the covariance between the two beam patterns $P_1(\theta, \phi)$ and $P_2(\theta, \phi)$ can be formulated as,

$$C_{12} = \int_0^{\pi/2} \int_0^{2\pi} [P_1(\theta, \phi) \times P_2(\theta, \phi)] d\Omega. \quad (5.5)$$

Since the majority of the beam spans between 0° and 90° in the θ direction as seen in Figure 5.1, the θ integration is performed within this range. For a set of 2 beams, one can create a 2×2 covariance matrix, A , such that it stands for representing the covariance values of each pair of beams as

$$A = \begin{bmatrix} C_{11} & C_{12} \\ C_{21} & C_{22} \end{bmatrix}, \quad (5.6)$$

where each element of the matrix represents the covariance calculated using Equation 5.5. The diagonal elements in the above matrix represent the variance of the individual beams while the off-diagonal terms represent the covariance between the pair of beams used. Unlike correlation, covariance values do not have a limit between -1 and 1 . Covariance values are sensitive to the scale of the variables involved and it might not be sufficient to conclude the strength of a relationship between two beams based on the matrix A . Normalizing the covariance matrix is essential to mitigate the influence of differing beam areas, ensuring that the comparison between beams reflects their true spatial correlations. This is done by scaling

the variance of individual beams to 1 as

$$\Sigma = D^{-1/2}AD^{-1/2} = \begin{bmatrix} 1 & C_{12} \\ C_{21} & 1 \end{bmatrix}, \quad (5.7)$$

where D is the diagonal of the covariance matrix A and Σ is the resulting correlation matrix. This normalization ensures a more robust comparison between the beams. To quantitatively assess the differences between the two beams $P_1(\theta, \phi)$ and $P_2(\theta, \phi)$, the eigenvalues (λ_1, λ_2) of the correlation matrix Σ is determined by solving the characteristic equation

$$|\Sigma - \lambda I| = 0, \quad (5.8)$$

where I is a 2×2 identity matrix. The ratio of the largest to smallest eigenvalue, called the condition number (R_{cond}) serves as an indicator of the power distribution between the average and difference components of two beams. To assess the amplitude of the difference relative to the amplitude of the beam average, the inverse square root of R_{cond} (denoted as r) can be computed as

$$R_{\text{cond}}^{-1/2} = r = \left(\frac{\lambda_{\min}}{\lambda_{\max}} \right)^{1/2}, \quad (5.9)$$

which provides a quantifiable measure to understand the non-redundancy between the two beams. The value of r ranges from 0 to 1, where 0 indicates no variations between the beams (i.e., they are identical), and 1 indicates distinct beams with zero commonality. This

procedure is not restricted to two beams but can be generalized to n beams, providing a quantifiable measure to understand the variations across multiple beam patterns. To further understand this mathematical concept, I will work through the following three pedagogical examples.

(i) Covariance between 2 identical beams: Let us consider two beams that are identical to each other. Since every corresponding point in the radiation patterns of the two beams will be the same, the covariance between the two beams, C_{12} and C_{21} , is equivalent to the variance of the individual beams, C_{11} and C_{22} . This results in a correlation matrix Σ where all the elements are identical. We can represent this case with a 2×2 matrix of ones as

$$\Sigma = \begin{bmatrix} 1 & 1 \\ 1 & 1 \end{bmatrix}. \quad (5.10)$$

The eigenvalues of this matrix, consisting entirely of ones, are determined to be $\lambda_1 = 2$ and $\lambda_2 = 0$. The presence of 0 as one of the eigenvalues indicates that the amplitude of the difference between the beams is zero, implying $r=0$ and no variations (or complete overlap) between the beams.

(ii) Covariance between 2 partially overlapping beams: Let us consider two beams that partially overlap. This scenario will be reflected in the off-diagonal terms of the correlation matrix, which will be non-zero while the diagonal terms remain one. For

simplicity, let us assume

$$\Sigma = \begin{bmatrix} 1 & 0.5 \\ 0.5 & 1 \end{bmatrix}. \quad (5.11)$$

The eigenvalues of this matrix are $\lambda_1 = 1.5$ and $\lambda_2 = 0.5$. The difference between the beams is then quantified as $r = \left(\frac{0.5}{1.5}\right)^{1/2} = 0.57$, which indicates some degree of non-redundancy between the beams.

(iii) Covariance between 2 non-overlapping beams: Now, consider two beams that do not overlap at all, meaning they are entirely distinct from each other. Because there is no commonality or shared variation between the beams, the covariance between the two beams, C_{11} and C_{22} approaches zero. For example, let us represent the resulting correlation matrix with a 2×2 identity matrix

$$\Sigma = \begin{bmatrix} 1 & 0 \\ 0 & 1 \end{bmatrix}, \quad (5.12)$$

where the off-diagonal elements represent the correlation between the beams which is zero and the diagonal elements are the variance of individual beams, scaled to one. The eigenvalues of this diagonal matrix are $\lambda_1 = 1$ and $\lambda_2 = 1$. The parameter $R_{\text{cond}}^{-1/2}$, which quantifies the difference between the beams is determined to be 1 which indicates zero commonality between the beams.

Now that these examples have demonstrated the effective use of beam covariance in quantifying beam perturbations, we can apply this concept to calculate the deviations

between fiducial and perturbed beams obtained from CST simulations.

5.3 Results and Discussions

In addition to examining the impact of dish surface discretization and deformations on the beam pattern, various other systematic perturbations were introduced into the CST models and studied in detail by Gerodias (2023). These perturbations included (i) shifting the feed position from the nominal focal point by increments ranging from -5 mm to $+5$ mm in steps of 1 mm along the x , y , and z directions and (ii) tilting/rotating the feed about the center of its physical structure in both the polar (x and y) and azimuthal (z) directions, varying from -2.5° to $+2.5^\circ$ in steps of 0.5° . Now that we have a robust metric for quantifying beam deviations, it would be intriguing to compute the beam covariances for these perturbation models along with the deformed surface models and gain a fresh perspective on their behavior.

The simulation setup included an $f/0.21$, 6-meter parabolic dish and a HIRAX feed as depicted in Figure 4.1(a), with a discrete excitation port specified only along the y direction. Farfield radiation patterns were computed using the time-domain solver for frequencies of 400, 600, and 800 MHz, covering HIRAX's operational frequency range. The beams obtained from the perturbed CST models are subsequently compared to the fiducial model, quantifying the difference between the beams as shown in Equation 5.9. Figure 5.2 shows the beam deviations, $R_{\text{cond}}^{-1/2}$, calculated for the HIRAX feed offsets ranging from -5 to $+5$ mm and dish surface discretization models with 5000 and 20000 facets. According to the HIRAX

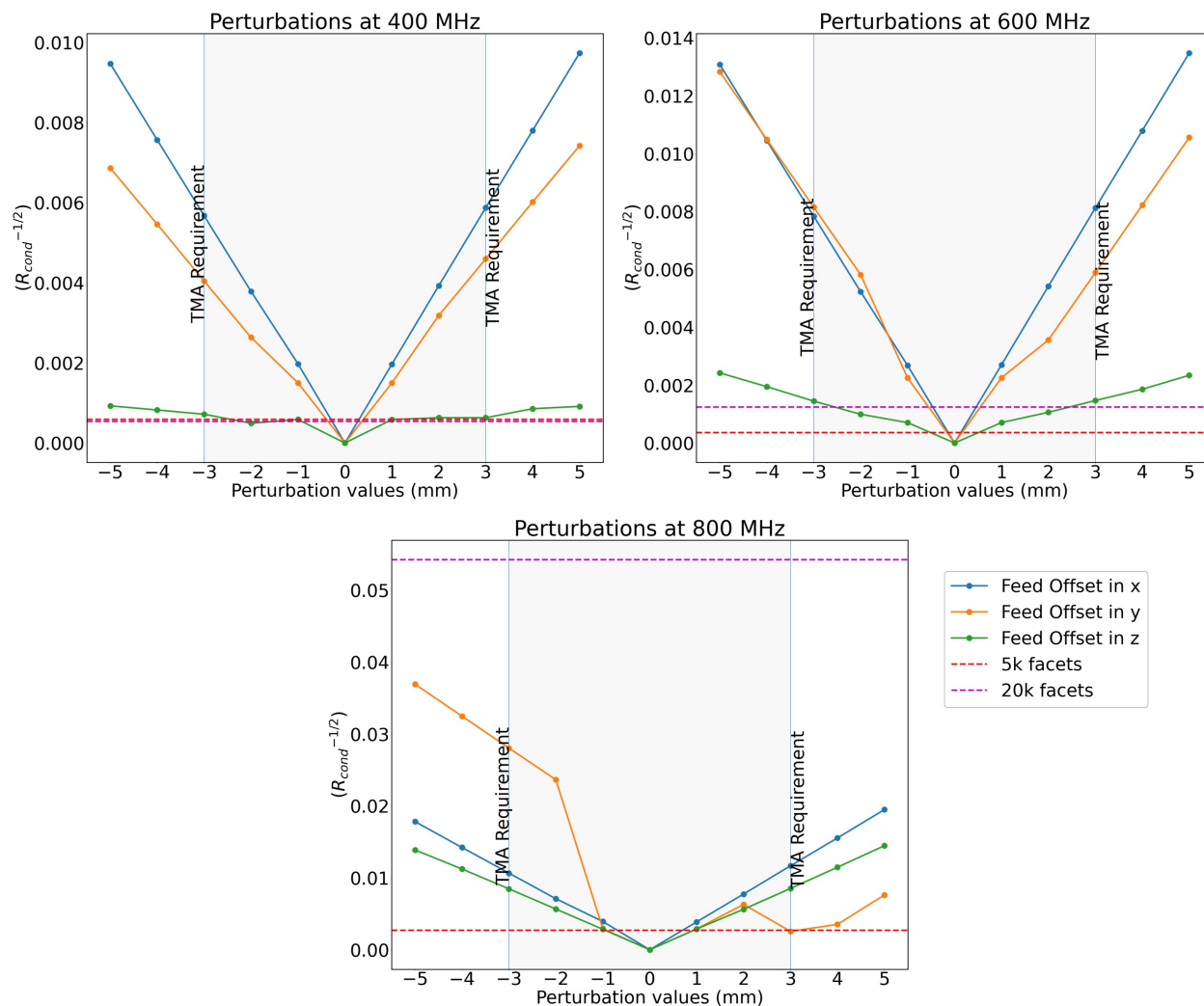


Figure 5.2: Beam deviations quantified as $R_{\text{cond}}^{-1/2}$ between the HIRAX fiducial and perturbed models, incorporating feed offsets in the x , y , and z axes, and surface discretization models with 5000 and 20000 facets. The plots emphasize the TMA requirement for feed position accuracy, which must be within ± 3 mm along all three axes relative to the focus.

TMA document, the feed position accuracy relative to the focus should be within ± 3 mm in the x , y , and z directions, as indicated in the figure below, with a precision better than 0.5 mm. From Figure 5.2, we infer that offsets in the x axis result in higher beam deviations,

followed by the y and z directions. However, at 800 MHz, this trend is not observed, as offsets in the y direction produce higher deviations, ranging from 0.01 to 0.04. At 400 MHz, beam deviations are symmetric between negative and positive perturbations across all three axes. As the frequency increases, we observe asymmetric behavior, particularly in the y direction. For example, at 800 MHz in the y axis, a perturbation of -2 mm results in a deviation of 0.023, while a $+2$ mm perturbation yields a deviation of 0.0063. One potential reason for this asymmetry is the offset placement of the excitation port in the HIRAX feed, as discussed in Chapter 4. This offset placement causes an uneven distribution of surface currents¹ on the cloverleaf petals, which in turn affects the electromagnetic field pattern, leading to the asymmetries observed in the HIRAX beams. For the 5000-faceted model, beam deviations reach a maximum of 0.002 at 800 MHz. However, for the 20000-faceted model, deviations increase by a factor of 10 as the frequency increases, highlighting the systematics introduced by increasing the surface resolution.

Table 5.1 presents the beam deviations calculated using the beam covariance approach for the deformed surface models, with surface errors propagated from laser tracker and photogrammetry analyses. Similar to the trends observed in Chapter 4 using the RMS metric, the beam deviations among the 5000 and 20000-faceted models are within a comparable range at 400 and 600 MHz. However, at 800 MHz, the beam deviations increase by a factor of 10 for both resolutions, with the 20000-faceted model showing a slightly greater difference

¹The study of surface currents on the HIRAX feed was conducted by PhD student *Kit M. Gerodias*, who is focusing on mitigating these asymmetries.

Table 5.1: Beam differences, $R_{\text{cond}}^{-1/2}$ for the deformed surface models with residuals propagated from laser tracker and photogrammetry analysis at 400, 600, and 800 MHz frequencies (ν).

Surface		Laser tracker			Photogrammetry			
deformation models		Dish 1	Dish 2	Dish 3	Dish 1		Dish 2	
Resolution	ν (MHz)				0°	30°	0°	30°
~5000 facets	400	0.00076	0.00078	0.00108	0.00077	0.00077	0.00065	0.00066
	600	0.00071	0.00062	0.00089	0.00094	0.00096	0.00073	0.00080
	800	0.00103	0.00114	0.00125	0.00116	0.00094	0.00148	0.00121
~20000 facets	400	0.00073	0.00075	0.00103	0.00083	0.00083	0.00062	0.00058
	600	0.00067	0.00063	0.00083	0.00092	0.00095	0.00051	0.00064
	800	0.00173	0.00233	0.00232	0.00233	0.00201	0.00108	0.00089

compared to the 5000-faceted model. Deviations between 0° and +30° zenith angles, as measured using photogrammetry residuals, are found to be nearly identical, with only minor variations observed at 800 MHz. Nevertheless, the beam deviations remain minimal, staying within a range of 0.003, confirming that the main lobe regions are not significantly affected. Figure 5.3 illustrates the beam deviations between the fiducial and perturbed CST models, incorporating feed tilts in the x , y , and feed rotation in z axes, ranging from -2.5° to $+2.5^\circ$. The grey-shaded region represents the perturbation limits set by the TMA document for x and y tilts ($\pm 0.083^\circ$ or 5 arcminutes) while the blue-shaded region indicates the limits for rotation around z ($\pm 0.125^\circ$ or 7.5 arcminutes) with a precision of 2.5 arcminutes in both

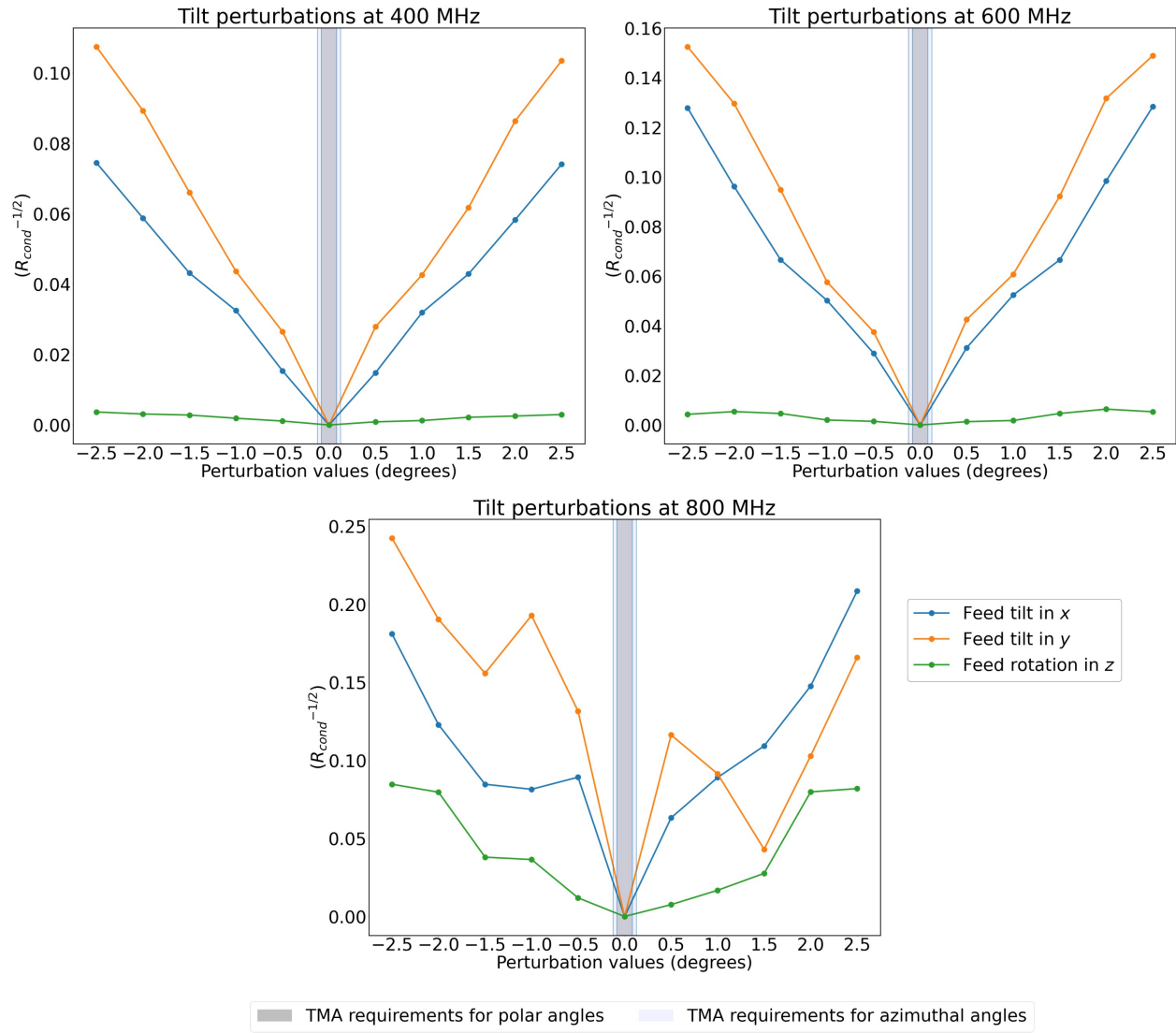


Figure 5.3: Beam deviations quantified as $R_{\text{cond}}^{-1/2}$ between the HIRAX fiducial and perturbed models, considering feed tilts in x , y , and feed rotation in z axes. The plots emphasize the TMA requirement for feed tilts of ± 5 arcminutes for polar angles and ± 7.5 arcminutes for the azimuthal angle.

polar and azimuthal axes. Compared to the results obtained from feed offsets, feed tilts lead to higher beam deviations, reaching a maximum value of 0.25 at 800 MHz for y -axis tilts.

It is observed that across all frequencies, tilts around the y axis produce higher deviations, followed by x tilts and z rotations. Although symmetry between positive and negative perturbations is observed at 400 and 600 MHz, it breaks down at 800 MHz. Preliminary studies with tilt perturbation models, where the excitation port was moved to the center of the antenna, demonstrated that the beam deviations maintained symmetry between positive and negative perturbations at all frequencies, producing an even distribution of surface currents in the cloverleaf petals without any lags. Current efforts are focused on improving the design of the HIRAX feed to mitigate this asymmetry. The zig-zag trends observed in both feed offsets and tilts, particularly in the y -axis at 800 MHz, where a $+0.5^\circ$ tilt produces higher deviations than a $+1.5^\circ$ tilt, require further investigations. Because the current range of feed tilt perturbation models is way beyond the limits set by the TMA requirements, it is essential to conduct additional CST simulations with finer resolution in the perturbation values to determine the beam variations within the acceptable limits. Hence, feed tilt/rotation simulations with perturbation values of $\pm 0.01^\circ$, $\pm 0.04^\circ$, $\pm 0.083^\circ$ (polar), and $\pm 0.125^\circ$ (azimuthal) are conducted and the differences quantified as $R_{\text{cond}}^{-1/2}$ are presented in Figure 5.4. It is observed that feed tilts around the y axis dominate the errors, followed by the x and z axes, at 400 and 600 MHz. However, at 800 MHz, tilts around the x axis result in higher beam deviations. Within the TMA limits for polar angles (± 5 arcminutes), beam deviations increase by a factor of 10 from 400 to 800 MHz. In contrast, perturbations along the azimuthal axis produce minimal deviations, with a

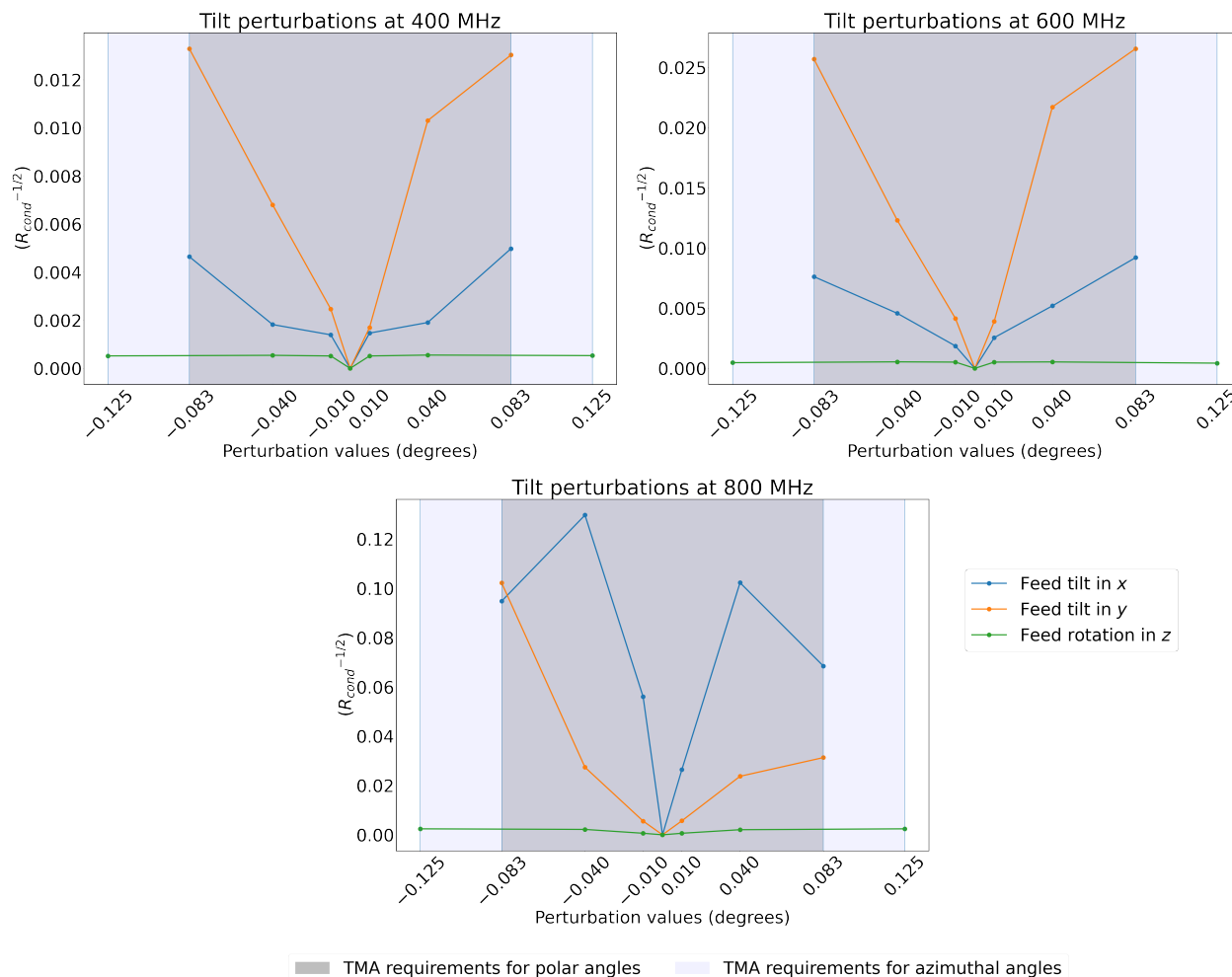


Figure 5.4: Beam deviations, quantified as $R_{\text{cond}}^{-1/2}$, between the HIRAX fiducial and perturbed models, considering feed tilts in x , y , and feed rotation in z axes, within the TMA limits of ± 5 arcminutes for polar angles and ± 7.5 arcminutes for the azimuthal angle.

maximum of ~ 0.002 at 800 MHz for perturbations greater than $> 0.01^\circ$. The asymmetric behavior between positive and negative perturbations, along with the zig-zag trend observed particularly with x and y -axis tilts, persists even within the TMA limits and will be the focus of future simulations. Comparing the $R_{\text{cond}}^{-1/2}$ values from Figures 5.3 and 5.4, a beam

deviation of ~ 0.1 is seen for both a y -axis feed tilt of $\pm 2.5^\circ$ at 400 MHz and $+0.01^\circ$ at 800 MHz. Obtaining such beam deviations for tilts with the TMA requirements, which are produced by a $\pm 2.5^\circ$ tilt warrants further investigation as it suggests that even minor tilts can lead to considerable beam deviations at higher frequencies, which could impact the performance of the system. Further studies should focus on understanding the underlying reasons for the differences observed and developing methods to mitigate any systematic effects associated with the feed tilt simulations. Throughout this study, beam deviations are compared across various perturbation models without establishing fixed minimum and maximum limits of $R_{\text{cond}}^{-1/2}$ for verification. These tolerances will be determined based on the results of cosmological simulations, which will analyze how these beam perturbations affect the 21 cm power spectrum sensitivity.

Chapter 6

Summary and Future Work

The central focus of this thesis revolved around characterizing the dish surface deformations of two next-generation radio instruments, HIRAX and CHORD which aim to map 21 cm emissions from neutral hydrogen to investigate BAO structures and unravel the universe's expansion history. To realize the key technologies required for CHORD and HIRAX including antenna feeds and LNA, reflector fabrication methods, and digital read-out systems, the D3A testbed was deployed at DRAO. Analysis of measurement data from laser tracker and photogrammetry metrology techniques revealed that the surface errors of D3A6 dishes 1, 2, and 3 are within the expected sub-millimeter precision, with the similarity between D3A6 dishes 2 and 3—differing only by $\sim 200\ \mu\text{m}$ —making them good representative of future fabrication methods. Additionally, D3A6 dishes 1 and 2 showed no significant deformations at the maximum zenith angle, demonstrating effective resistance to gravitational effects

when tilted. The laser tracker and photogrammetry analysis routine developed in this work provided a robust foundation for future studies and can be expanded to facilitate the analysis of large-scale production of dishes. By refining and scaling these methodologies, it will be possible to verify the required standards for dish fabrication and achieve high-precision results. Feed displacements at wind speeds typical for DRAO (i.e., under 25 kph) remained below ~ 0.7 mm, while at 80 kph, they reached approximately 1 mm, regardless of the presence of a radome.

To determine if the calculated surface and systematic errors are within acceptable limits for the telescope's performance in line with the scientific objectives, EM simulations were conducted incorporating both HIRAX and CHORD feed. Simulations of the deformed surface models with the HIRAX feed showed that the beam deviations ranged between ~ 0.1 and 0.3 dB across the operating frequency range of 400 to 800 MHz. The comparable results from the 5000 and 20000-faceted models indicated that the former might be sufficient for capturing surface deformations accurately and reducing computational costs. However, future simulations with more facets will be conducted to confirm if this trend continues. In addition, future simulations will aim to validate and determine the phase center location across the entire frequency band of HIRAX. This will clarify the greater beam deviations observed at 600 MHz compared to those at 800 MHz, highlighting a correlation between the phase center definition and beam performance. The first set of CHORD simulations with the discretized surface models showed that the 20000-faceted

model closely resembled the fiducial compared to the 5000 and 47000 faceted-models. Current efforts are focused on validating this result by employing integral domain solvers in the EM simulations. The plan involves decoupling the dish from the physical feed structure by importing a far-field excitation source, hoping to eliminate dish-feed interaction effects and concentrate solely on the dish discretization systematics. Additionally, more simulations are planned with the CHORD feed that will incorporate dish surface errors identified through laser tracker and photogrammetry analyses, as well as other systematics such as feed offset and tilt from its nominal position.

Calculating the beam covariances— a metric that considers spatial variations among the beam patterns by reducing the influence of far off-axis regions and focusing more on the main lobe—for systematic perturbations of the HIRAX feed including feed offsets and tilts/rotations in the x , y and z axes showed that feed tilts, especially in the y axis, produced higher beam deviations and asymmetric patterns compared to feed offsets. Current studies aim to improve the HIRAX feed design to mitigate the asymmetric behavior of the beams at higher frequencies. In the future, greater emphasis will be placed on feed tilt simulations to understand the significant beam deviations observed, by employing the integral domain solver in simulations and using a farfield excitation source. Additionally, simulations will be conducted for the CHORD feed to analyze its behavior under various systematic perturbations and dish surface deformations, similar to the approach taken for HIRAX. The simulations presented in this chapter have enriched our

understanding of the beam deviations caused by dish surface discretization, deformations, and systematic perturbations. The ultimate goal would be to evaluate these potential systematic effects on 21 cm cosmology by propagating the perturbations derived from the CST simulations to 21 cm power spectrum errors, which will be the story of another thesis.

Bibliography

- E. Abdalla, E. G. Ferreira, R. G. Landim, A. A. Costa, K. S. Fornazier, F. B. Abdalla, L. Barosi, F. A. Brito, A. R. Queiroz, T. Villela, et al. The BINGO Project-I. Baryon Acoustic Oscillations from Integrated Neutral Gas Observations. *Astronomy & Astrophysics*, 664:A14, 2022.
- P. Ade, J. Aguirre, Z. Ahmed, S. Aiola, A. Ali, D. Alonso, M. A. Alvarez, K. Arnold, P. Ashton, J. Austermann, et al. The Simons Observatory: Science Goals and Forecasts. *Journal of Cosmology and Astroparticle Physics*, 2019(02):056, 2019.
- A. Aghamousa, J. Aguilar, S. Ahlen, S. Alam, L. E. Allen, C. A. Prieto, J. Annis, S. Bailey, C. Balland, O. Ballester, et al. The DESI Experiment Part I: Science, Targeting, and Survey Design. 2016.
- L. Amendola, S. Appleby, A. Avgoustidis, D. Bacon, T. Baker, M. Baldi, N. Bartolo, A. Blanchard, C. Bonvin, S. Borgani, et al. Cosmology and Fundamental Physics with the Euclid Satellite. *Living reviews in relativity*, 21:1–345, 2018.

- M. Amiri, B. C. Andersen, K. Bandura, S. Berger, M. Bhardwaj, M. M. Boyce, P. Boyle, C. Brar, D. Breitman, T. Cassanelli, et al. The First CHIME/FRB Fast Radio Burst Catalog. *The Astrophysical Journal Supplement Series*, 257(2):59, 2021.
- M. Amiri, K. Bandura, T. Chen, M. Deng, M. Dobbs, M. Fandino, S. Foreman, M. Halpern, A. S. Hill, G. Hinshaw, C. Höfer, J. Kania, T. L. Landecker, J. MacEachern, K. Masui, J. Mena-Parra, et al. Detection of Cosmological 21 cm Emission with the Canadian Hydrogen Intensity Mapping Experiment. *The Astrophysical Journal*, 947(1), 2023.
- É. Aubourg, S. Bailey, J. E. Bautista, F. Beutler, V. Bhardwaj, D. Bizyaev, M. Blanton, M. Blomqvist, A. S. Bolton, J. Bovy, et al. Cosmological Implications of Baryon Acoustic Oscillation Measurements. *Physical Review D*, 92(12):123516, 2015.
- K. Bandura, A. N. Bender, J. Cliche, T. de Haan, M. Dobbs, A. J. Gilbert, S. Griffin, G. Hsyu, D. Ittah, J. M. Parra, et al. ICE: A Scalable, Low-cost FPGA-based Telescope Signal Processing and Networking System. *Journal of Astronomical Instrumentation*, 5(04):1641005, 2016.
- B. Bassett and R. Hlozek. Baryon Acoustic Oscillations. *Dark energy: Observational and Theoretical Approaches*, 246, 2010.
- B. A. Benson, P. Ade, Z. Ahmed, S. Allen, K. Arnold, J. Austermann, A. Bender, L. Bleem, J. Carlstrom, C. Chang, et al. SPT-3G: A Next-generation Cosmic Microwave Background Polarization Experiment on the South Pole Telescope. In *Millimeter, Submillimeter, and*

- Far-Infrared Detectors and Instrumentation for Astronomy VII*, volume 9153, pages 552–572. SPIE, 2014.
- C. G. Broyden. The convergence of a class of double-rank minimization algorithms: 2. the new algorithm. *IMA journal of applied mathematics*, 6(3):222–231, 1970.
- T.-C. Chang, U.-L. Pen, K. Bandura, and J. B. Peterson. An Intensity Map of Hydrogen 21-cm Emission at Redshift $z \approx 0.8$. *Nature*, 466(7305):463–465, 2010.
- C.-C. Chiong, Y. Wang, K.-C. Chang, and H. Wang. Low-noise Amplifier for Next-generation Radio Astronomy Telescopes: Review of the State-of-the-art Cryogenic LNAs in the most Challenging Applications. *IEEE Microwave Magazine*, 23(1):31–47, 2021.
- J. J. Condon and S. M. Ransom. *Essential Radio Astronomy*, volume 2. Princeton University Press, 2016.
- D. Crichton, M. Aich, A. Amara, K. Bandura, B. A. Bassett, C. Bengaly, P. Berner, S. Bhatporia, et al. Hydrogen Intensity and Real-Time Analysis Experiment: 256-element Array Status and Overview. *Journal of Astronomical Telescopes, Instruments, and Systems*, 8(1):011019–011019, 2022.
- Dassault Systemes. CST Studio Suite: Electromagnetic Field Simulation Software, 2021.
- M. Davis, S. M. Faber, J. Newman, A. C. Phillips, R. S. Ellis, C. C. Steidel, C. Conselice, A. L. Coil, D. Finkbeiner, D. C. Koo, et al. Science Objectives and Early Results of the

- DEEP2 Redshift Survey. In *Discoveries and Research Prospects from 6-to 10-Meter-Class Telescopes II*, volume 4834, pages 161–172. SPIE, 2003.
- K. S. Dawson, J.-P. Kneib, W. J. Percival, S. Alam, F. D. Albareti, S. F. Anderson, E. Armengaud, É. Aubourg, S. Bailey, J. E. Bautista, et al. The SDSS-IV Extended Baryon Oscillation Spectroscopic Survey: Overview and Early Data. *The Astronomical Journal*, 151(2):44, 2016.
- J. C. N. de Araujo. The Dark Energy–Dominated Universe. *Astroparticle Physics*, 23(2): 279–286, 2005.
- I. Debono and G. F. Smoot. General Relativity and Cosmology: Unsolved Questions and Future Directions. *Universe*, 2(4), 2016.
- S. Dodelson and F. Schmidt. *Modern Cosmology*. Academic press, 2020.
- A. Dolgov. Modern Cosmology and Physics beyond the Standard Model. *Surveys in High Energy Physics*, 6(2):57–113, 1991.
- D. J. Eisenstein, I. Zehavi, D. W. Hogg, R. Scoccimarro, M. R. Blanton, R. C. Nichol, R. Scranton, H.-J. Seo, M. Tegmark, Z. Zheng, S. F. Anderson, J. Annis, N. Bahcall, J. Brinkmann, S. Burles, et al. Detection of the Baryon Acoustic Peak in the Large-Scale Correlation Function of SDSS Luminous Red Galaxies. *The Astrophysical Journal*, 633(2):560–574, 2005.

- P. M. Garnavich, S. Jha, P. Challis, A. Clocchiatti, A. Diercks, A. V. Filippenko, R. L. Gilliland, C. J. Hogan, R. P. Kirshner, B. Leibundgut, et al. Supernova Limits on the Cosmic Equation of State. *The Astrophysical Journal*, 509(1):74, 1998.
- K. M. Gerodias. Simulations and Data Analysis for HIRAX and CHORD. Master's thesis, Department of Physics, Trottier Space Institute, McGill University, 2023.
- D. J. Griffiths. Hyperfine Splitting in the Ground State of Hydrogen. *American Journal of Physics*, 50(8):698–703, 1982.
- A. H. Guth. Inflationary Universe: A Possible Solution to the Horizon and Flatness Problems. *Physical Review D*, 23(2):347, 1981.
- S. Henderson, R. Allison, J. Austermann, T. Baidon, N. Battaglia, J. Beall, D. Becker, F. De Bernardis, J. Bond, E. Calabrese, et al. Advanced ACTPol Cryogenic Detector Arrays and Readout. *Journal of Low Temperature Physics*, 184:772–779, 2016.
- I. T. Hendricksen. Observational, Digital Readout and Calibration Techniques for Studying the Redshifted 21-cm Signal of Hydrogen. Master's thesis, Department of Physics, Trottier Space Institute, McGill University, 2023.
- HIRAX Collaboration. [HIRAX Telescope Mechanical Assemble Requirements Document](#). University of KwaZulu-Natal (UKZN), 2021.

- E. Hubble. A Relation between Distance and Radial Velocity among Extra-Galactic Nebulae. *Proceedings of the national academy of sciences*, 15(3):168–173, 1929.
- D. Huterer. *A Course in Cosmology: From Theory to Practice*. Cambridge University Press, 2023.
- M. N. Islam and D. Ölçek. Metrology of Deep Dish Development Array (D3A) for Precision Alignment and Surface Deformation Analysis. In *Ground-based and Airborne Telescopes VIII*, volume 11445, pages 893–903. SPIE, 2020.
- M. N. N. Islam. D3A6 Dish/Mold Surface Accuracy and Precision. 2023.
- M. N. N. Islam, D. Ölçek, G. Lacy, H. C. Chiang, and R. Hellyer. Errors in Deep Dish Development Array (6m) Construction and Metrology Steps. In *Ground-based and Airborne Telescopes IX*, volume 12182, pages 149–160. SPIE, 2022.
- M. Kuhlen, P. Madau, and R. Montgomery. The Spin Temperature and 21 cm Brightness of the Intergalactic Medium in the Pre-reionization Era. *The Astrophysical Journal*, 637(1):L1, 2006.
- E. R. Kuhn, B. R. Saliwanchik, M. Harris, M. Aich, K. Bandura, T.-C. Chang, H. C. Chiang, et al. Design and Implementation of a Noise Temperature Measurement System for the Hydrogen Intensity and Real-time Analysis eXperiment (HIRAX). 2021.
- A. Liu, M. Tegmark, S. Morrison, A. Lutomirski, and M. Zaldarriaga. Precision Calibration

- of Radio Interferometers using Redundant Baselines. *Monthly Notices of the Royal Astronomical Society*, 408(2):1029–1050, 2010.
- V. MacKay, M. Lai, P. Shmerko, D. Wulf, L. Belostotski, and K. Vanderlinde. Low-cost, Low-loss, Ultra-wideband Compact Feed for Interferometric Radio Telescopes. *Journal of Astronomical Instrumentation*, 2022.
- J. Mena, K. Bandura, J.-F. Cliche, M. Dobbs, A. Gilbert, and Q. Y. Tang. A Radio-frequency-over-fiber Link for Large-array Radio Astronomy Applications. *Journal of Instrumentation*, 8(10):T10003, 2013.
- J. D. Monnier and R. J. Allen. *Radio & Optical Interferometry: Basic Observing Techniques and Data Analysis*. 2012.
- R. Nan, D. Li, C. Jin, Q. Wang, L. Zhu, W. Zhu, H. Zhang, Y. Yue, and L. Qian. The Five-Hundred-Meter Aperture Spherical Radio Telescope (FAST) Project. *International Journal of Modern Physics D*, 20(06):989–1024, 2011.
- L. Newburgh, K. Bandura, M. Bucher, T.-C. Chang, H. Chiang, J. Cliche, R. Davé, M. Dobbs, C. Clarkson, K. Ganga, et al. HIRAX: A Probe of Dark Energy and Radio Transients. In *Ground-based and Airborne Telescopes VI*, volume 9906, pages 2039–2049. SPIE, 2016.

- A. D. Nitto. Characterizing Prototype Dishes for CHORD and HIRAX using Reflectometry. Master's thesis, Department of Physics, McGill University, 2023.
- A. Nusser. The Spin Temperature of Neutral Hydrogen during Cosmic Pre-reionization. *Monthly Notices of the Royal Astronomical Society*, 359(1):183–190, 2005.
- S. Paul, M. G. Santos, Z. Chen, and L. Wolz. A First Detection of Neutral Hydrogen Intensity Mapping on Mpc Scales at $z \approx 0.32$ and $z \approx 0.44$. 2023.
- E. Petroff, J. Hessels, and D. Lorimer. Fast Radio Bursts. *The Astronomy and Astrophysics Review*, 27(1):4, 2019.
- E. Pieters. Prototyping and Testing Analog Electronics and Dishes for HIRAX and CHORD. Master's thesis, Department of Physics, McGill University, 2021.
- R. M. Prestage, K. T. Constantikes, T. R. Hunter, L. J. King, R. J. Lacasse, F. J. Lockman, and R. D. Norrod. The Green Bank Telescope. *Proceedings of the IEEE*, 97(8):1382–1390, 2009.
- J. R. Pritchard and A. Loeb. 21 cm Cosmology in the 21st Century. *Reports on Progress in Physics*, 75(8):086901, 2012.
- R. Reichke and S. Hagstotz. Cosmological Covariance of Fast Radio Burst Dispersions. *Monthly Notices of the Royal Astronomical Society*, 524(2):2237–2243, 2023.

- B. F. Roukema. The Baryon Acoustic Oscillation Peak: A Flexible Standard Ruler. In *The Fourteenth Marcel Grossmann Meeting On Recent Developments in Theoretical and Experimental General Relativity, Astrophysics, and Relativistic Field Theories: Proceedings of the MG14 Meeting on General Relativity, University of Rome “La Sapienza”, Italy*, pages 2327–2332. World Scientific, 2018.
- V. C. Rubin and W. K. Ford Jr. Rotation of the Andromeda Nebula from a Spectroscopic Survey of Emission Regions. *Astrophysical Journal*, 159:379, 1970.
- V. C. Rubin, D. Burstein, W. K. Ford Jr, and N. Thonnard. Rotation Velocities of 16 SA Galaxies and a Comparison of Sa, Sb, and SC Rotation Properties. *Astrophysical Journal*, 289:81–98, 1985.
- B. Ryden. *Introduction to Cosmology*. Cambridge University Press, 2017.
- B. R. Saliwanchik, A. Ewall-Wice, D. Crichton, E. R. Kuhn, D. Ölçek, K. Bandura, M. Bucher, T.-C. Chang, H. C. Chiang, K. Gerodias, et al. Mechanical and Optical Design of the HIRAX Radio Telescope. In *Ground-based and Airborne Telescopes VIII*, volume 11445, pages 1047–1067. SPIE, 2021.
- B. Santos, J. C. Carvalho, and J. S. Alcaniz. Current Constraints on the Epoch of Cosmic Acceleration. *Astroparticle Physics*, 35(1):17–20, 2011.
- B. P. Schmidt, N. B. Suntzeff, M. Phillips, R. A. Schommer, A. Clocchiatti, R. P. Kirshner,

- P. Garnavich, P. Challis, B. Leibundgut, J. Spyromilio, et al. The High-Z Supernova Search: Measuring Cosmic Deceleration and Global Curvature of the Universe using Type Ia Supernovae. *The Astrophysical Journal*, 507(1):46, 1998.
- F. Shamshad and M. Amin. Simulation Comparison between HFSS, CST and WIPL-D for Design of Dipole, Horn and Parabolic Reflector Antenna. *Advances in Computational Mathematics and its Applications*, 1(4):203–207, 2012.
- G. B. Taylor, C. L. Carilli, and R. A. Perley. Synthesis Imaging in Radio Astronomy II. *Synthesis Imaging in Radio Astronomy II*, 180, 1999.
- A. R. Thompson, J. M. Moran, and G. W. Swenson. *Interferometry and Synthesis in Radio Astronomy*. Springer Nature, 2017.
- C. Tzu-Ching, P. Ue-Li, B. Peterson Jeffrey, and M. Patrick. Baryon Acoustic Oscillation Intensity Mapping as a Test of Dark Energy. *Phys. Rev. Lett*, 100:091303, 2008.
- K. Vanderlinde, A. Liu, B. Gaensler, D. Bond, G. Hinshaw, C. Ng, C. Chiang, I. Stairs, J.-A. Brown, J. Sievers, et al. The Canadian Hydrogen Observatory and Radio-transient Detector (CHORD). *Canadian Long Range Plan for Astronomy and Astrophysics White Papers*, 2020:28, 2019.
- P. Virtanen, R. Gommers, T. E. Oliphant, M. Haberland, T. Reddy, D. Cournapeau,

-
- E. Burovski, P. Peterson, W. Weckesser, et al. SciPy 1.0: Fundamental Algorithms for Scientific Computing in Python. *Nature Methods*, 17:261–272, 2020.
- M. Zhang, H.-L. Zhang, Y.-Z. Zhang, J. Wang, S.-C. Guo, and Q. Meng. Research on Channelization Techniques of Radio Astronomical Wideband Signal with Oversampled Polyphase Filter Banks. *Research in Astronomy and Astrophysics*, 23(8):085012, 2023.